Geodätisch-geophysikalische Arbeiten in der Schweiz

(Fortsetzung der Publikationsreihe
«Astronomisch-geodätische Arbeiten in der Schweiz»)

herausgegeben von der

Schweizerischen Geodätischen Kommission
(Organ der Schweizerischen Akademie der Naturwissenschaften)

Einundsechzigster Band
Volume 61

Spatial and Temporal Distribution of Atmospheric Water Vapor using Space Geodetic Techniques

Lars Peter Kruse

2001

Geodätisch-geophysikalische Arbeiten in der Schweiz

(Fortsetzung der Publikationsreihe
«Astronomisch-geodätische Arbeiten in der Schweiz»)

herausgegeben von der

Schweizerischen Geodätischen Kommission
(Organ der Schweizerischen Akademie der Naturwissenschaften)

Einundsechzigster Band
Volume 61

Spatial and Temporal Distribution of Atmospheric Water Vapor using Space Geodetic Techniques

Lars Peter Kruse

2001

Adresse der Schweizerischen Geodätischen Kommission:

Institut für Geodäsie und Photogrammetrie
Eidg. Technische Hochschule Zürich
ETH Hönggerberg
CH-8093 Zürich, Switzerland

Internet: http://www.sanw.ch/exthp/geodet/

ISBN 3-908440-03-3

Redaktion des 61. Bandes:
Dr. L. P. Kruse, Dr. B. Bürki

Druck: Print-Atelier E. Zingg, Zürich

VORWORT

Im vorliegenden Band werden die neuesten Methoden zur integralen Wasserdampfbestimmung mit GPS analysiert und einer sorgfältigen Fehleruntersuchung unterzogen. Dieses relativ neue Gebiet wird mit "GPS-Meteorologie" bezeichnet. Neben dem integralen Wasserdampfanteil werden auch Möglichkeiten zur Bestimmung der Höhenverteilung des Wasserdampfes erarbeitet und in realen Messkampagnen getestet. Einen zentralen Mittelpunkt bildete auch die Frage, wie weit es möglich ist, real-time Berechnungen vorzunehmen; d.h., aus GPS on-line Wasserdampf zu schätzen, auch wenn keine hochpräzisen Bahnparameter der Satelliten vorliegen.

Die GPS Meteorologie ist noch relativ neu und wenig bearbeitet. Dies liegt zum Teil daran, dass international wenig Ground Truth Daten erhoben werden können. In der Schweiz konnte hierzu durch Eigenentwicklungen in der Wasserdampfradiometrie und Sonnenspektrometrie ein wesentlicher Beitrag geleistet werden. Zudem ist einer der wichtigen Ground-Truth Datensätze durch Bodenstationen gegeben, wie sie in der Schweiz durch das Meteo-Netz ANETZ der Schweizerischen Meteorologischen Anstalt SMA realisiert sind. Zusätzlich sind die Ballonsondierungen in Payerne für die mathematische Stützung des Modells wichtig.

Herr Kruse hat nicht nur Algorithmen entwickelt, sondern auch an Hand von Experimenten quantitative Hinweise auf die Möglichkeiten der verschiedenen Methoden gegeben. Das erste Experiment wurde im Deep Space Network der NASA und ESA in Spanien ausgeführt. Herr Kruse zeigt, dass der Wasserdampf sehr starke zeitliche Fluktuationen aufweist, die über wenige Tage hinweg bis zu 20 mm ausfällbaren Wasserdampf erreichen können. Im zweiten Beispiel wird ein 10-tägiges Experiment am Radioteleskop der TU Göteborg vorgeführt.

Die Leistungsfähigkeit der entwickelten Software kann sehr schön an Beobachtungen von längerer Dauer beurteilt werden. Hierzu hat Herr Kruse 18-monatige Datensätze von der AGNES Station Hönggerberg benutzt. Deutlich sieht man aus den GPS-Schätzungen die wesentlich grösseren Wasserdampfgehalte im Sommer, wenn die Atmosphäre aufgrund der höheren Temperatur mehr Feuchtigkeit aufnehmen kann.

Ein weiteres Interesse betrifft die zeitliche und räumliche Verteilung des Wasserdampfes aus GPS: ein Problem, das gegenüber der Bestimmung des integralen Wasserdampfgehaltes als wesentlich schwerer einzustufen ist. Herr Kruse hat das Softwarepaket "Atmospheric Water Vapor Tomography Software (AWATOS)" entwickelt und in einem dedizierten Experiment in Hawaii angewandt. Hier konnte er horizontale Inhomogenitäten der Troposphäre nachweisen, welche die Machbarkeit seines tomographischen Ansatzes eindrücklich bestätigten.

Die SGK dankt Herrn Kruse für die Arbeiten, die einen wesentlichen neuen Beitrag zur Geodäsie in der Schweiz darstellen. Herr Dr. B. Bürki vom GGL hat sowohl in wissenschaftlicher wie auch in organisatorischer Hinsicht sehr zum Gelingen der Untersuchungen beigetragen. Herr Dr. M. Cocard hat bei der Entwicklung der AWATOS Software tatkräftig mitgewirkt und Herr Dr. A. Geiger hat mit seinen fundierten Ratschlägen zum Gelingen des Projektes auf allen Stufen beigetragen. Ihnen gebührt unser herzlicher Dank.

Dank geht auch an die Kollegen Dres. G. Elgered, P. Jarlemark und J. Johansson vom Onsala Space Observatoray in Schweden und Dres. M. Lisowski, M. Bevis und J. Foster vom Hawaiian Volcano Observatory und der Universität von Hawaii in USA.

Der ETH Zürich, dem Bundesamt für Bildung und Wissenschaft (BBW) sowie der Schweizerischen Akademie für Naturwissenschaften (SANW) danken wir für die finanzielle Unterstützung dieses Projektes (EU ENV4-CT96-0301). Von der SANW wurden die Druckkosten übernommen, wofür die SGK ihren grossen Dank ausspricht.

Prof. Dr. H.-G. Kahle
ETH Zürich
Präsident der SGK

Dr. h.c. E. Gubler, Direktor
Bundesamt für Landestopographie
Vizepräsident der SGK

PREFACE

Dans le présent fascicule les nouvelles méthodes de détermination du contenu intégral de la vapeur d'eau atmosphérique par GPS sont analysées et une étude soignée des sources d'erreurs y est conduite. Ce domaine relativement nouveau est dénommé météorologie par GPS. A côté de la partie de la vapeur d'eau intégrale les possibilités de détermination de la distribution en fonction de l'altitude sont étudiées et celles-ci sont testées en campagnes de mesures réelles. Un point central soulève la question de savoir comment il est possible de calculer en temps réel, à partir des données GPS le contenu en vapeur d'eau atmosphérique quand aucun paramètres précis des trajectoires des satellites ne sont disponibles.

La météorologie par GPS est relativement neuve et jusque à maintenant peu étudiée. Ceci provient en partie que peu de "Ground Truth" internationaux sont disponibles. En suisse une contribution a pu être apportée à la météorologie par GPS et à la spectroscopie solaire par un développement propre du GGL. En outre un des plus important ensemble de données de "Ground Truth" est donné au travers de stations au sol comme cela est réalisé par le réseau météorologique ANETZ de l'agence météorologique suisse. De plus les sondages par ballons de Payerne sont important pour la justification des modèles mathématiques.

Monsieur Kruse n'a pas seulement développé des algorithmes mais a aussi donné des indications quantitatives, basées sur des expériences, sur les possibilités des différentes méthodes. La première expérience a été conduite en Espagne sur le " Deep Space Network" de la NASA et de l'ESA. Monsieur Kruse a montré que la vapeur d'eau présente une très forte fluctuation temporelle qui sur quelques jours peut atteindre des chutes allant jusqu'à 20 millimètres. Dans le second exemple est décrite une expérience de dix jours sur le radio télescope de l'université technique de Göteborg à Onsala.

La puissance du logiciel développé ne peut être jugé que sur des longues périodes d'observations. Pour cela Monsieur Kruse a utilisé un ensemble de données d'une période de 18 mois mesurées à la station AGNES du Hönggerberg. L'on y voit distinctement sur la base des appréciations par GPS que la grande teneur en vapeur d'eau de l'atmosphère correspond à une température élevée qui permet à l'atmosphère d'acquérir une plus grande humidité. Un autre intérêt concerne la détermination de la distribution temporelle et spatiale de la vapeur d'eau à partir des données GPS: Le problème est que cette détermination est essentiellement beaucoup plus difficile à quantifier. Monsieur Kruse a développé le logiciel "Atmosphere Water Vapor Tomography Software" (AWATOS) et l'a appliqué à une expérience propre conduite à Hawaii. De cette expérience il a pu mettre en évidence les hétérogèneités horizontales de la troposphère ce qui a démontré l'applicabilité de sa formulation des règles de la tomographie.

La Commission Suisse de Géodésie remercie Monsieur Kruse pour ces travaux qui représentent une contribution substantielle à la géodésie suisse. Monsieur Beat Bürki du GGL a aussi contribué à la réussite de cette étude par son apport scientifiquement et dans son active participation à l'organisation. Dr. M. Cocard a participé au development du logiciel AWATOS. Durant tout le projet, Dr. A. Geiger a apporté ses conseils constructifs. Nous leur en sommes reconnaissant.

Nous remercions également nos collègues les Dres. G. Elgered, P. Jarlemark and J. Johansson de l'Observatoire Spatial d'Onsala en Suède et les Dres. M. Lisowski, M. Bevis et J. Foster de l'Observatoire Volcanologique d'Hawaii et de l'Université d'Hawaii aux Etats Unis.

L'EPF-Zürich, l'office fédérale de l'education et de la science (OFES) et l'Académie Suisse des Sciences Naturelles (ASSN) ont contribué substantiellement par leur apport financier à la bonne réalisation de ce projet (EU ENV4-CT96-0301). Les coûts d'impression de ce fascicule ont été supportés par l'ASSN. La Commission Suisse de Géodésie les remercie vivement.

Prof. Dr. H.-G. Kahle
ETH Zürich
Président de la CGS

Dr. h.c. E. Gubler, Directeur
de l'Office fédéral de topographie
Vice-président de la CGS

FOREWORD

The volume presented includes an overall analysis on most recent methods to estimate integral precipital water vapor (IPWV) based on GPS observations. This topic has become known as "GPS meteorology". In addition to the IPWV also attempts are being made to determine the distribution of water vapor as a function of height. Dedicated campaigns have been conducted to test the feasibility of the theoretical approach. Of particular interest was also the question whether real-time estimates are possible given the fact that precise orbital information is not available online.

One of the reasons why "GPS meteorology" has not been commonly applied yet is the lack of knowledge of ground truth either in terms of hardware or appropriate networks. In this volume Dr. L.P. Kruse takes advantage of available water vapor radiometers and a solar spectrometer at the ETH Zurich, as well as of the widely distributed meteo network of the Swiss Meteorological Service (SMA). Also data from radio soundings at the Swiss SMA station Payerne was used to strengthen the model.

Dr. Kruse has developed alogorithms which were first tested at the Deep Space Network of NASA and ESA in Spain. Strong variations of IPWV reaching 20 mm were detected over a short time span of only a few days. A second experiment was conducted at the radiotelescope in Göteborg, Sweden. The usefulness of the algorithms were tested with a 18 months long data set collected from a CGPS station at the ETH Hönggerberg. The systematic increase of IPWV at summer time can clearly be seen in the analyzed data.

In order to shed light on the height distribution of water vapor Dr. Kruse has developed a software package called "AWATOS" (Atmospheric Water Vapor Tomography Software). It was applied in a dedicated high-density network on the Big Island of Hawaii. The good knowledge on ground truth data along a large height range between the coast and Mt. Kilauea, enabled to validate the algorithms to a large extent.

The Swiss Geodetic Commission thanks Dr. Kruse for his highly valuable contribution in the new field of GPS Meteorology. Dr. B. Bürki of the Geodesy and Geodynamics Lab (IGP ETHZ) has significantly supported the work both in practical, editorial and scientific aspects. Dr. M. Cocard assisted in developing the AWATOS software. Dr. A. Geiger gave critical advice during all stages of the project. Their help is gratefully acknowledged.

Thanks are also due to our colleagues Dres. G. Elgered, P. Jarlemark and J. Johansson from the Onsala Space Observatory in Sweden and to Dres. M. Lisowski, M. Bevis and J. Foster of the Hawaiian Volcano Observatory and the University of Hawaii in USA.

We are furthermore grateful to the ETH Zurich, the Swiss Federal Office for Education and Science (FOES) and the Swiss Academy of Sciences (SAS) for financial support of the project (EU ENV4-CT96-0301). The SAS has also provided funds for printing this volume which is greatly appreciated.

Prof. Dr. H.-G. Kahle
ETH Zurich
President of SGC

Dr. h.c. E. Gubler, Director
Federal Office of Topography
Vice President of SGC

Abstract

This work investigates methodological aspects of the Global Positioning System (GPS) to validate its potential as a remote sensing tool for monitoring atmospheric water vapor. GPS estimates of integral precipital water vapor (IPWV) are compared with simultaneous measurements of co-located Water Vapor Radiometers (WVR), as well as atmospheric refraction models for validation of GPS for meteorological applications.

Based on a one year data set of continuous GPS estimates and WVR observations at ETH Zurich a standard deviation of 1.54 mm and an offset of 0.54 mm IPWV is found between the two techniques. The analysis of several dedicated observation campaigns carried out at different sites in Europe and on Hawaii revealed offsets between GPS estimates and WVR observations.

The instrumental methods are also compared with a numerical model of the troposphere using ground meteorological observations and radiosondes from the station Payerne of the Swiss meteorological network (ANETZ). The modeling results, obtained with a software package performing four-dimensional interpolations by collocation yield a standard deviation of 2.88 mm and a bias of 2.23 mm IPWV with respect to the GPS derived time series of IPWV. Furthermore a clear seasonal dependency of the GPS - WVR differences is recognized. Mainly the periods dominated by strong fluctuations of water vapor during summer and autumn months degrade the agreement between the two techniques.

Because of the high correlation between GPS estimated tropospheric parameters and the height component, potential error sources are investigated.

The accuracy of GPS-derived IPWV in near real-time for consideration in weather forecasting is degraded due to insufficient satellite orbit quality. Investigations on the impact of implementing predicted orbit information on GPS water vapor retrievals showed that the accuracy degrades by a factor of about 2 compared to results obtained with final precise orbits as released by the International GPS Service (IGS) about two weeks after the observations.

Finally the potential of GPS for resolving three-dimensional distributions of tropospheric water vapor by means of the tomographic technique is investigated and applied within this work. For this purpose a software package called AWATOS (Atmospheric WAter vapor TOmography Software) was developed. In order to validate the tomographic approach a dedicated field experiment was carried out on the Big Island of Hawaii, USA. Tomographic results based on the extremely dense Continuous GPS (CGPS) network in the Mt. Kilauea and Mauna Loa volcano area are presented. They are compared to other independent techniques, such as radiosondes, Water Vapor Radiometers, and a high resolution solar spectrometer.

Zusammenfassung

Zur Bestimmung des atmosphärischen Wasserdampfs wurde der Einsatz von GPS als Fernerkundungsmethode untersucht. Um die Güte von GPS-Schätzungen des integralen ausfällbaren Wasserdampfgehalts (IPWV) zu überprüfen, wurden Simultanmessungen mit Wasserdampf-Radiometern (WVR) durchgeführt. In diesem Zusammenhang wurde ein Datensatz eines Jahres untersucht, der in Zürich mit GPS und WVR erhoben wurde. Die berechnete Standardabweichung für den IPWV ergab 1.54 mm mit einem Offset von 0.54 mm. Dabei wurde eine klare saisonale Abhängigkeit der GPS-WVR differenzen festgestellt. Vor allem die Perioden, die von starken Fluktuationen des Wasserdampfs im Sommer und Herbst dominiert sind, reduzieren die Übereinstimmung zwischen den beiden Techniken.

Resultate von atmosphärischen Modellrechnungen, die auf einer vierdimensionalen Interpolations-Software beruhen, wurden mit den GPS-Schätzwerten verglichen und ergaben eine Standardabweichung von 2.88 mm, mit einem Offset von 2.23 mm. Die Analyse von mehreren einschlägigen Beobachtungskampagnen, die an verschiedenen Stationen in Europa und in Hawaii durchgeführt wurden, zeigten Offsets zwischen den GPS-Schätzungen und den Radiometermessungen.

Infolge der hohen Korrelation zwischen den aus GPS geschätzten Troposphärenparametern und der Punkthöhe, wurden potentielle Fehlerquellen untersucht. Die Genauigkeit von GPS-Schätzungen des IPWV in Quasi-Echtzeit für die Berücksichtigung in der Wettervorhersage wird durch ungenügende Genauigkeit der Satellitenbahn vermindert. Untersuchungen zum Einfluss des Einbezugs von vorausberechneten (prädizierten) Bahnbögen ergaben, dass die Genauigkeit um den Faktor zwei schlechter ist, als bei der Berücksichtigung von präzisen Bahnbögen, die vom Internationalen GPS Service (IGS) mit ca. zwei Wochen Verzögerung veröffentlicht werden.

Schliesslich wird das Potential von GPS-Messungen für die Bestimmung der dreidimensionalen Verteilung des Wasserdampfgehalts mittels der Tomographie untersucht. Zu diesem Zweck wurde ein Programmpaket AWATOS (Atmospheric WAter vapor TOmography Software) entwickelt. Zur Überprüfung des tomographischen Verfahrens wurde in Hawaii ein gezieltes Feldexperiment durchgeführt und im Rahmen dieser Arbeit ausgewertet. Es werden Resultate der tomographischen Berechnungen präsentiert, die im extrem dichten CGPS-Netz erhoben wurden, das vom US Geological Survey und den Universitäten Hawaii und Stanford in der Umgebung der Vulkane Mt. Kilauea und Mauna Loa auf Big Island betrieben wird. Diese werden mit unabhängigen Methoden, wie Radiosonden, Wasserdampf-Radiometer und einem Sonnenspektrometer verglichen.

Contents

1 Introduction

The Global Positioning System of Navigation Satellites (GPS) offers the the potential to compute 3D positions to subcentimeter precision. Using its inherent strength, GPS has been widely deployed in a broad spectrum of Geophysical applications, where high accuracy positioning is required, such as monitoring of crustal motions (e.g [Kahle et al., 1999], [McClusky et al., 2000]) and sea level changes (e.g. [Penna, 1997], [Becker et al., 2000]). Until recently, atmospheric effects have been the main limitation in precise positioning because microwaves traversing the atmosphere suffer refraction along the propagation path, resulting in an excess path delay of the signal. Since atmospheric refractivity depends on the composition of atmospheric gases, the signal delay changes both in space and time. The delay caused by the dry constituents, mainly N_2 and O_2, is straightforward to determine from barometric measurements since the mixing ratios of these gases are constant up to heights of about 50km [R.McIlven, 1989]. In contrast, the component due to atmospheric water vapor, referred to as the wet path delay, is difficult to determine, because its distribution is highly variable at both temporal and spatial scale. It can be shown, that the wet path delay is proportional to the amount of integrated precipitable water vapor (IPWV) in the troposphere. The removal of refraction errors from GPS data therefore requires either modeling or measurement of IPWV in the troposphere.

Models for the tropospheric refraction have been utilized, which estimate the microwave path delay using ground meteorological measurements (i.e. [Saastamoinen, 1973], [Askne and Nordius, 1987]). More sophisticated models calculate 3D and 4D fields of atmospheric refractivity by including radiosonde soundings ([Bevis et al., 1996], [Hirter, 1998]). However, these approaches suffer from a low correlation of surface humidity with the vertical profile and the sparseness of radiosonde data. Nevertheless, in cases where the topography facilitates a good distribution of surface meteo observations in height, an increased accuracy can be achieved.

Because of the limited use of meteorological models and the increasing significance of GPS in Geodynamics and other disciplines, remote sensing techniques have been developed for the determination of IPWV or refraction delay, respectively. Water Vapor Radiometers (WVR) measure the radiation intensity of the atmosphere in a frequency band usually ranging from 20 to 32 GHz. The radiation intensity of water vapor in the direction of the antennas is proportional to the amount of water vapor molecules along the line of sight. Data from WVRs have been used for correcting the wet path delay in space geodetic measurements. Their deployment is especially use-

ful in geodetic applications where the accuracy of the vertical component is crucial [Alber et al., 1997]. Ongoing instrumental developments of microwave systems have shown the capability of retrieving vertical profiles of water vapor [Solheim et al., 1998].

One decade of research in microwave signal propagation revealed that investigations of refraction problems in geodesy are likely to have interdisciplinary impact on atmospheric sciences and related fields. In meteorology and atmospheric sciences the water vapor content of the troposphere is a parameter of major importance. Its significance is due to the key role of water molecules in most energy transportation and conversion processes in the atmosphere. It is the most variable constituent of the atmosphere with a significant contribution to the greenhouse effect and the only one which exists in the solid, liquid and gaseous state. Due to its high latent heat it is a crucial parameter in numerical weather prediction models. Therefore its variability is a major source of uncertainty in weather forecasting. Especially vertical profiles of humidity are of utmost importance for meteorologists since weather changes associated with cold and warm fronts start at high altitudes.

In the past several years a new technique, referred to as GPS-meteorology ([Bevis et al., 1992]), has been developed which reverses the refraction problem of GPS measurements by using continuously operating receivers whose positions are accurately known. The GPS derived path delays can be converted into IPWV by a model using surface values of atmospheric pressure and temperature.

The feasibility of this technique has been demonstrated in numerous studies ([Bevis et al., 1992], [Rocken et al., 1995], [Duan et al., 1996], [Baker, 1998]) and several weather services are currently implementing data from meteorological GPS networks to improve their forecasts. In collaboration with geodetic institutes, meteorological and climatological communities (e.g. UK Met Office and Deutscher Wetterdienst) are now operating GPS networks in order to improve forecasting. The advantages of GPS over existing methods such as WVR are cost efficiency and low maintainance as well as all-weather monitoring capabilities. Although recent comparisons of GPS estimated IPWV with independent measurements such as WVRs and radiosondes show good agreement, there are biases and temporal disagreements which need to be investigated ([Baker, 1998])

The accuracy of GPS-derived IPWV in near real-time for assimilation in weather forecasting is degraded due to satellite orbit quality. High-precision orbits provided by GPS analysis centers are not yet available in real-time. Therefore operational meteorological GPS analysis will rely on orbit predictions. Investigations on the impact of introducing predicted orbit information on the accuracy of GPS water vapor retrievals have been carried out by [Baker, 1998] and [Kruse et al., 1999].

Another limitation of GPS-derived water vapor from a meteorological point of view is the absence of vertical information on the humidity distribution. From a single GPS receiver in a large scale network only column abundances of water vapor can be derived. On the other hand, the GPS signals measured by a network intersect

the overlying troposphere by a multitude of rays given by the satellite constellation and network geometry. Given a dense receiver network, the water vapor distribution could be estimated from the GPS network data utilizing a tomographic approach. Although this technique has been proposed by Bevis et al. in 1992, only recently feasibility studies of GPS tomography have been carried out [WAVEFRONT, 1999]. The main reason for this is the necessity of an extremely dense continuous network of receivers with baseline lengths on the order of 10 km or less.

In this work numerous aspects of ground based GPS meteorology are addressed, including the problems mentioned above. Different methods for atmospheric water vapor determination are investigated and compared for the validation of GPS derived water vapor estimates. The propagation properties of microwave signals and basic atmospheric laws are discussed in chapter 2 to serve as a basis for the following chapters. Direct measurements of atmospheric parameters such as pressure, temperature and humidity can be used as input for modeling the state of the atmosphere. This topic is investigated in chapter 3 and compared to the remote sensing techniques GPS and Water Vapor Radiometry (WVR).

At the Geodesy and Geodynamics Laboratory (GGL), as well as in many other groups, several years of experience have been made with the WVR technique. The error budget is well understood and completely independent from that of GPS meteorology. Water vapor retrievals from this well established technique are therefore used as a comparison standard for all GPS results throughout this work. Because of the high significance of radiometry retrievals as a quasi ground truth, it is important to review the characteristics of this remote sensing technique (chapter 4), including the retrieval techniques based on radiative transfer models. To estimate the absolute accuracy of the technique, comparisons with other radiometric instruments were performed and described at the end of chapter 4.

The use of GPS as a remote sensing tool for atmospheric water vapor estimates will be discussed in chapter 5. Several short term campaigns with co-located GPS and WVRs were carried out at different sites and seasons in Europe. More than one year of almost continuous GPS and WVR estimates are compared to models of atmospheric water vapor. The accuracy of simulated near real-time GPS water vapor estimates compared to water vapor radiometry is discussed at the end of chapter 5.

The present work also presents one of the first studies on GPS tomography (see above). In order to assess and validate the tomographic capabilities of GPS, a dedicated field experiment was carried out on Big Island in Hawaii, USA [Bürki et al., 1999]. The data from the ultra-dense Continuous GPS (CGPS) network operated in the Mt. Kilauea volcano area and from the co-located remote sensing systems represent a unique dataset for validation and accuracy assessment of GPS tomography. Results from the Hawaiian campaign are discussed in chapter 6 where all techniques described in previous chapters including Solar Spectrometry (SSM) are outlined and mutually compared. Three-dimensional resolution of atmospheric water vapor, based on the Mt. Kilauea network and its limitations are investigated

in chapter 7. Finally the intercomparison of all applied techniques, the tomographic results as well as the limitations will be discussed in chapter 8.

2 Propagation properties of the atmosphere

2.1 Introduction

The propagation of radio waves from GPS satellites to ground based receivers is affected by the refractive atmosphere. The atmosphere (ionosphere and the neutral troposphere) bends the propagation path and causes changes in the propagation velocity. The Ionosphere is a dispersive medium for frequencies in the radio-band. By using a linear combination of the two frequencies emitted by GPS satellites it is possible to mitigate the ionospheric refraction to more than 99% under quiet conditions. The delay due to ionospheric refraction is well modeled and not a great error source for elevations above 15 degrees. A detailed discussion can be found in Rothacher and Mervart [1996], and Schaer [1999]. In contrary to the ionosphere the troposphere is a non-dispersive medium for frequencies below 15 GHz. The tropospheric refraction causes a delayed arrival of radio signals, often referred to as excess propagation delay expressed in meters.

2.2 Atmospheric propagation delay

The electric path length L of a radio signal propagating along the path O (Figure 2.1) is defined as

$$L = \int_O n\, ds \tag{2.1}$$

If n is known the path O can be determined by Fermat's Principle of least times. The signal will propagate through the atmosphere along the minimum electrical path length L (from b to a). The geometrical straight-line distance M represents the path that a signal would travel if it were propagating through vacuum.

$$G = \int_M ds \tag{2.2}$$

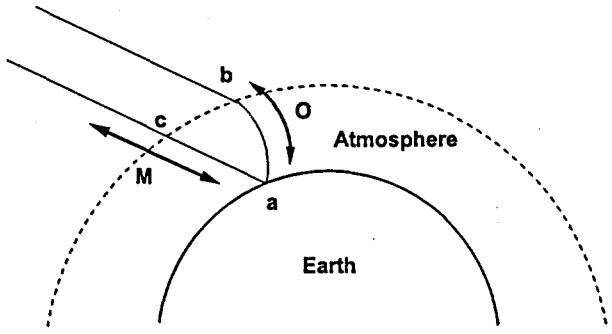

Figure 2.1: Signal propagation of an extraterrestrial radio source (e.g. GPS satellite) to the antenna. The geometrical path length (M) represents the propagation in vacuum

The difference between the electrical path length (L along O) and the geometrical straight-line distance (G along M) is called the excess propagation path. By combining equation 2.1 and 2.2 we get an expression of the path delay ΔL.

$$\Delta L = (L - G) = \int_a^b (n-1)\, ds + S - G \tag{2.3}$$

The term $S = \int_O ds$ expresses the path length along the curved path O and the difference (S-G) is called the delay due to bending or geometrical delay. The effect of the geometrical delay is zero for a ray with zenith direction and about 10 cm at 5deg elevation. Since the refractive index of the atmosphere n is very close to unity, it is common to define refractivity, N, as parts per million differing from unity

$$N = 10^6\ (n-1) \tag{2.4}$$

A common expression for the refractivity N [Owens, 1967] is

$$N = k_1 \frac{P_d}{T} Z_d^{-1} + k_2 \frac{e}{T} Z_w^{-1} + k_3 \frac{e}{T^2} Z_w^{-1} \tag{2.5}$$

Where P_d is the partial pressure of the dry constituents of air in hPa. e is the partial pressure of water vapor in hPa, T is the temperature in Kelvin and Z_d^{-1} and Z_w^{-1} are the inverse compressibility factors of dry air and water vapor, respectively. These compressibility factors equal 1 for an ideal gas. Their departure to unity are proportional to pressure, temperature and water vapor pressure [Owens, 1967]. Saturated air with the temperature 30°C at sea level (e = 42.5 hPa and P 1013 hPa) yields 1.00027 for Z_d and 1.00201 for Z_w which is a departure of 0.2%. Because of their small contributions, these factors will be neglected in the following. The first

	$k_1[K/hPa]$	$k_2[K/hPa]$	$k_3[K^2/hPa]$
Smith & Weintraub [1954]	77.61 ± 0.01	72 ± 9	$(3.75 \pm 0.03) \times 10^5$
Thayer [1974]	77.604 ± 0.014	64.79 ± 0.08	$(3.776 \pm 0.004) \times 10^5$

Table 2.1: Refractivity coefficients of different models

two terms of Eq. 2.5 are due to the induced dipole effect, whereas the third term is caused by the permanent dipole moment of the water vapor molecule. The constants k_1, k_2 and k_3 can be determined from laboratory experiments. The most often used values for the coefficients are those of Smith and Weintraub [1954] and Thayer [1974] as listed in Table 2.1. The constants given by Thayer are used throughout this work since they are provided with the highest accuracies.

The first term in Eq.2.5 represents the dry refractivity, the second and third terms describe the wet refractivity. However, the measurable barometric pressure is the sum of all partial pressures (wet and dry). The gas law for each gas i

$$P_i = \rho_1 \frac{R}{m_i} T \tag{2.6}$$

where ρ_i is the density, m_i the molar mass, and R the universal gas constant (8314.34 $\pm$ 0.35 J/kmol K). We can now rewrite Eq. 2.5 as

$$\begin{aligned} N &= k_1 \frac{R}{m_d} \rho_d + k_2 \frac{R}{m_w} + k_3 \frac{e}{T^2} \\ &= k_1 \frac{R}{m_d} \rho + \left(k_2 - k_1 \frac{m_w}{m_d}\right) \frac{e}{T} + k_3 \frac{e}{T^2} \end{aligned} \tag{2.7}$$

where ρ is the total density, and ρ_d and ρ_w are the densities of dry and wet air, respectively. m_d and m_w are the molar masses of dry (28.9644 kg/kmol) and wet (18.0152 kg/kmol) air, respectively. The first term of 2.7 contains the total air density. Inserting this term in 2.3 and integrating in the zenith direction we get

$$\Delta L_h^z = 10^{-6} k_1 \frac{R}{m_d} \int_s^h \rho(h) dh \tag{2.8}$$

where: ΔL_h^z is the hydrostatic delay in the zenith direction

To get an expression of the zenith delay as a function of the total pressure P_0 the hydrostatic equation

$$\frac{dP}{dh} = -\rho(h)\ g(h) \tag{2.9}$$

is used. Integrating Eq. 2.9, we obtain

$$P_0 = g_{eff} \int \rho(h)\, dh \tag{2.10}$$

where

$$g_{eff} = \frac{\int \rho(h) g(h)\, dh}{\int \rho(h)\, dh} \tag{2.11}$$

By combining 2.10 and 2.8 The hydrostatic delay in the zenith direction can be evaluated as

$$\Delta L_h^z = (0.0022768 \pm 0.0000024(m/hPa)) \frac{P_0}{f(\Theta,\ H)} \tag{2.12}$$

where

$$f(\Theta,\ H) = 1 - 0.00266\ \cos 2\Theta\ -\ 0.00028H \tag{2.13}$$

describes the variation of the acceleration due to gravity [Saastamoinen, 1973]. Θ is the latitude, and H the height in km (above the ellipsoid) of the station. The wet component of the total delay can now be defined by inserting the last two terms of Eq. 2.7 into Eq. 2.3

$$\Delta L_w = 10^{-6} \int_O (k_2' \frac{e}{T} + k_3 \frac{e}{T^2})\, ds \tag{2.14}$$

where

$$k_2' = k_2 - k_1 \frac{m_w}{m_d} = 22.1 K h P a^{-1} \tag{2.15}$$

The contribution of the first term in Eq.2.14 is about 1% of the second term. The expression can be simplified without loss of accuracy by introducing a mean weighted temperature T_m, defined by

$$T_m = \frac{\int_O \frac{e}{T}\, ds}{\int_O \frac{e}{T^2}\, ds} \tag{2.16}$$

Inserting this expression in Eq. 2.14 we get

$$\Delta L_w = 10^{-6}(k_2' + k_3/T_m) \int_O \frac{e}{T^2}\, ds \tag{2.17}$$

After having removed the hydrostatic part of the total path-delay we are left with the remaining wet delay in units of meters. The mixing ratio of the non-polar atmospheric gases can be considered to be constant [R.McIlven, 1989] therefore the hydrostatic delay can be well modeled from barometer measurements alone. In

contrast to the hydrostatic delay the wet delay is highly variable due to local micro climatical conditions such as topography and sea-land interference. In general the wet delay is not easily predictable from surface humidity measurements because the correlation between surface conditions and those at higher altitudes are low [Askne and Nordius, 1987]. However, if measurements are available at higher altitudes like in the ANETZ network in Switzerland ranging from 500 up to 3600 m above sea level the accuracy of path delay calculations can be improved (see Chapter 3 Table 3.2).

2.3 Conversion of wet delay into water vapor

For meteorological applications the wet path delay is converted into atmospheric water vapor expressed as integrated precipitable water vapor (IPWV) defined as

$$IPWV = \frac{1}{\rho_l} \int_O \rho_v \, ds \tag{2.18}$$

where $\rho_l = 1000 \; kg \; m^{-3}$ is the density of liquid water and ρ_v is the water vapor density as a function of height. Since water vapor behaves as an ideal gas in terrestrial conditions, we can use the equation of state to relate the water vapor pressure e to vapor density ρ_v and absolute temperature T

$$e = \rho_v R_v T \tag{2.19}$$

where $R_v = 461.524 \; J \; K^{-1} kg^{-1}$ is the specific gas constant for water vapor. Combining Eq. 2.14, 2.18, and 2.19 yields

$$\Delta L_w = 10^{-6}(k_2' + k_3/T_m) R_v \; IPWV \tag{2.20}$$

The value of T_m requires information of the vertical profile of water vapor pressure and temperature. Instead of using the same value for the mean temperature for all sites and seasons Bevis et al. [1992] derived a linear relation between the surface temperature T_s and the weighted mean temperature T_m, based on 8'718 radiosonde profiles from 13 stations in the United States:

$$T_m = 70.2 + 0.72 T_s \tag{2.21}$$

The error introduced by using Eq. 2.21 is expected by the authors to be about 2% [Bevis et al., 1992]. Edmarson and Derks [1999] investigated several models for the conversion from wet-delay to IPWV based on more than 120'000 radiosonde profiles from 38 sites in Europe. Their polynomial model (Eq. 2.22) using measured surface temperature data yielded an error of 1.14% when all European sites were considered.

$$\frac{IPWV}{\Delta L_w} = a_0 + a_1 T\Delta + a_2 T\Delta^2 \tag{2.22}$$

$T\Delta$ are the deviation in surface temperature from the mean value for the data set used (in K). The values of the coefficients $a_{0,1,2}$ with their respective RMS are documented in the above reference.

The observed IPWV's can be compared to the corresponding quantities as calculated from direct atmospheric observations such as pressure, temperature and humidity. In the following chapter, models of atmospheric water vapor are compared to estimates from remote sensing techniques.

3 Modeling of atmospheric Water Vapor

3.1 Introduction

The modeling of tropospheric water vapor by means of meteorological observations is investigated and compared to the remote sensing techniques (GPS and WVR). A variety of models for atmospheric refraction corrections has been developed over the last 30 years [Hopfield, 1969], [Saastamoinen, 1973] and [Askne and Nordius, 1987]. In general, the precision of models using meteorological surface measurements never perform better than ± 3 mm IPWV. Although this accuracy may be sufficient for many applications, for precise positioning purposes such as GPS or *Very Long Base Line Interferometry* (VLBI) it is not adequate. An often used expression for atmospheric effects on microwave signals is the model derived by Saastamoinen [1973]. The model for the total path delay is:

$$\Delta L_{tot} = \frac{0.002277}{cos(\Phi)}\Big[P + \Big(\frac{1255}{T} + 0.05\Big)e - B\ tan^2 z\Big] + \delta \qquad (3.1)$$

Where P, T and e are pressure, temperature and water vapor pressure observations, Φ is the zenith distance, and δ and B are correction terms due to station height and latitude. The formula assumes an exponential decay for air and water vapor pressure and a linear decrease of temperature in the troposphere of 6.22 K/km. Saastamoinen [1973] estimated the accuracy of the hydrostatic path delay in the zenith direction to be in the range of 2-3 mm (see also Eq. 2.12) whereas the wet component was assumed to be 3 - 5 cm. Saastamoinen [1973] "... *the most important single source of error is due to local variations in the vertical distribution of humidity which may cause an error of up to one-fifth of the standard correction for vapor pressure*". Askne and Nordius [1987] investigated several models for the determination of total wet delay by surface observations and radiosoundings. Their statistical model uses radiosonde measurements to calculate a priori information of the vertical distribution of water vapor. This statistical model and a slightly modified Saastamoinen model was compared to radiosonde measurements and showed an RMS between 2.3 - 2.6 cm (Copenhagen) and 2.56 - 3.9 cm (Onsala) path delay, respectively.

3.2 Modeling

The software package COMEDIE (Collocation of Meteorological Data for Interpretation and Estimation of Tropospheric Path Delays) [Eckert et al., 1992; Hirter, 1998] is a four-dimensional (spatial and temporal) modeling software package based on least-squares collocation (see e.g. Moritz [1973]). The model is described by a functional part of pressure, temperature and water vapor as well as a stochastic part describing the deviations from the functional model. The interpolation of the stochastic part is achieved by optimizing the correlated signal and white noise residuals simultaneously.

3.2.1 Deterministic modeling

The deterministic model functions of pressure temperature and water vapor are

$$P(x,y,z,t) = (P_0 + bx + cy + dt)e^{\frac{z}{H_P}} \tag{3.2}$$

$$T(x,y,z,t) = T_0 + bx + cy + dt + \gamma z \tag{3.3}$$

$$e(x,y,z,t) = (e_0 + bx + cy + dt)\ 10^{\frac{z}{H_e}} \tag{3.4}$$

where x,y,z are spatial coordinates, P_0, T_0 and e_0 are pressure, temperature and water vapor pressure at the reference height z = 0, H_P and H_e are scale heights for total pressure and water vapor pressure, respectively, and γ is the rate at which the temperature changes with height (temperature lapse rate). All three models account for a linear variation of the parameters in the horizontal coordinates and time. The functional models are represented by slowly varying standard tropospheric behavior and the parameters are estimated together with the stochastic part.

3.2.2 Stochastic modeling

The collocation method is an extension of the classical least-squares formulation ($\mathbf{l} = \mathbf{Ax} + \mathbf{v}$). The residual parameter v is split up into a signal and a noise term: $\mathbf{v} = (\mathbf{s} + \mathbf{n})$

$$\mathbf{l} = \mathbf{Ax} + \mathbf{s} + \mathbf{n} \tag{3.5}$$

l is the measurement,
A is the design matrix
x is the vector of unknowns
s is the signal at the measurement (colored noise)
n is measurement noise (white noise).

The minimization criteria for the collocation is:

$$\mathbf{n}^T\mathbf{C}_{nn}^{-1}\mathbf{n} + \mathbf{s}^T\mathbf{C}_{ss}^{-1}\mathbf{s} = \mathbf{Minimum} \tag{3.6}$$

where $\mathbf{C}_{nn}$ and $\mathbf{C}_{ss}$ are covariance matrices for the noise and signal, respectively. The least-squares solution (for details see Schmid [1977]; Moritz [1980]) of the parameter is given by:

$$\mathbf{x} = (\mathbf{A}^T\mathbf{D}^{-1}\mathbf{A})^{-1}\mathbf{A}^T\mathbf{D}^{-1}\mathbf{l} \tag{3.7}$$
$$\mathbf{s} = \mathbf{C}_{ss}\mathbf{D}^{-1}(\mathbf{l} - \mathbf{A}\mathbf{x}) \tag{3.8}$$
$$\mathbf{n} = \mathbf{C}_{nn}\mathbf{D}^{-1}(\mathbf{l} - \mathbf{A}\mathbf{x}) \tag{3.9}$$
$$\mathbf{D} = \mathbf{C}_{ss} + \mathbf{C}_{nn} \tag{3.10}$$

The three equations 3.7, 3.8 and 3.9 describe the parameter solutions for the functional model $\mathbf{x}$, and signal and noise for every observation. The calculation of values between points of observations (interpolation) is done in the same manner:

$$\mathbf{l}' = \mathbf{A}'\mathbf{x} + \mathbf{C}_{ss'}\mathbf{D}^{-1}(\mathbf{l} - \mathbf{A}\mathbf{x}) \tag{3.11}$$

where $\mathbf{l}'$ is the interpolated value,
$\mathbf{A}'$ is the design matrix
$\mathbf{s}'$ is the interpolated signal
$\mathbf{C}_{ss'}$ is the covariance matrix describing the covariance between signals s_1 and s_2 at the points P_1 and P_2

Assumptions have to be made on the elements of the covariance matrices $\mathbf{C}_{nn}$, $\mathbf{C}_{ss}$ and $\mathbf{C}_{ss'}$. The measurement noise $\mathbf{n}$ is regarded as uncorrelated and the matrix $\mathbf{C}_{nn}$ has diagonal shape whereas the signal is expected to be correlated. The covariance elements of $\mathbf{C}_{ss}$ and $\mathbf{C}_{ss'}$ were determined by the covariance function (3.12).

$$\Phi_{ij} = \frac{\sigma_0^2}{1 + \left[(\frac{x_i - x_j}{\Delta x_0})^2 + (\frac{y_i - y_j}{\Delta y_0})^2 + (\frac{z_i - z_j}{\Delta z_0})^2 + (\frac{t_i - t_j}{\Delta t_0})^2\right] \cdot f \cdot exp(-\frac{z_i + z_j}{2z_0})} \tag{3.12}$$

where σ_0^2 is the variance of the signal, x, y, z and t describe the spatial coordinates and time, respectively, Δx_0, Δy_0, Δz_0 and Δt_0 are the correlation lengths and f is a constant. Equation 3.12 describes a spatial and temporal anisotropic covariance function. The spatial variability of atmospheric parameters (pressure, temperature and water vapor) dominates in the vertical direction. This anisotropy is accounted for by applying appropriate correlation lengths in the corresponding directions. In general the spatial and temporal sampling of the upper atmosphere by radiosoundings is poor compared to ground meteo observations from meteorological networks.

	σ_0^{signal}	σ_0^{noise}	Δx_0	Δy_0	Δz_0	Δt_0	z_0	f
P	6 hPa	0.5hPa	200 km	150 km	800 m	1.9 hours	4 km	1
T	5 C	0.5 C	75 km	50 km	250	1.2 hours	4 km	1
e	3 hPa	0.5 hPa	75 km	50 km	250	1.2 hours	4 km	1

Table 3.1: Correlation parameters used to calculate the elements of the Covariance matrix for the interpolation of pressure temperature and water vapor pressure

Since high altitude measurements are important for reliable estimation of atmospheric parameters (see Figure 3.4) the validity of measurements from radiosondes has to be extended both in time and in space. With the factor f and the correlation length z_0 within the exponential term in 3.12 the correlation with height can be increased. Table 3.1 shows the covariance parameters used for the collocation. All elements of the covariance matrix are calculated with the covariance function. Finally interpolated (predicted) values at any points are calculated as the weighted average of all observations whereby the associated weight factors are determined by the covariance function.

3.3 The ANETZ network

The Swiss meteorological network ANETZ (see Figure 3.1) consists of 72 permanent stations recording 15 - 25 meteorological parameters every 10 minutes. At the aerological station Payerne (PAY, 491 m.a.sl.) radiosondes are launched every 12 hours. The accuracy of the surface station measurements has been compared with radiosonde measurements by Richner and Phillips [1984], Tschirren [1989], Gassner [1990] and Richner and Viatte [1995]. Standard deviations of pressure, temperature and water vapor pressure were estimated to be in the range of 0.5 [hPa], 1.0 K and 1.0 hPa, respectively. Tschirren [1989] showed that measurements of water vapor pressure from the network stations are in general higher than in the free atmosphere (less than 1 hPa). Since April 1990, the Swiss SRS 400 sonde type is flown. The basic measurements are temperature and pressure. The humidity is measured by a boiling-point barometer commonly called hypsometer [Richner et al., 1996].

The height distribution of the network is shown in Figure 3.2 in intervals of 200 meters. About 50% of all stations are at altitudes below 1000 m and 9 stations (12.5%) are above 2000 m.

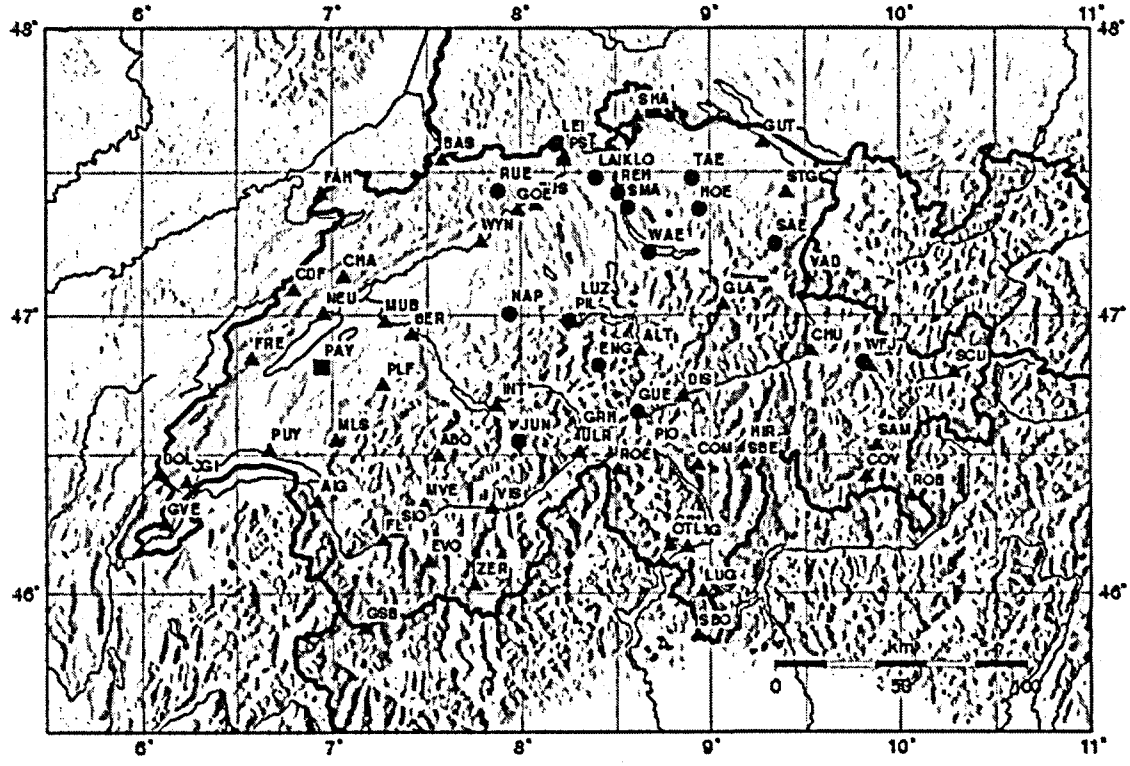

Figure 3.1: Map of the ground meteorological station network ANETZ in Switzerland. A total of 72 stations is displayed (triangles and dots). The stations indicated by dots were used for the modeling. The aerological and radiosonde launch station Payerne (PAY) of the Swiss National Weather Service is indicated as a square. The vertical distribution of the stations ranges from 432 m to 3.5 km above sea level (see also Figure 3.2)

3.4 Comparisons and Results

In this section four comparisons of IPWV at the station ETHZ are shown. 21 days of data during December 1997 are investigated. Two solutions were calculated with the modeling software COMEDIE, hereafter COM1 and COM2, where both use the surface meteo observations from stations marked by dots in Figure 3.1. COM1, uses in addition radiosonde measurements from the Payerne station. COM1 is then compared with the wet part of the Saastamoinen (SAAS) model and IPWV estimates from GPS and WVR. Table 3.2 shows mean and standard deviation for the four comparisons.

In Figure 3.3a,b the results from the COM1 solution are shown together with the results obtained by the SAAS and COM2 solutions. The results from the Saastamoinen model are in general below the COM1 solution whereas the COM2 solution is in general higher throughout this period. When comparing the SAAS and COM2

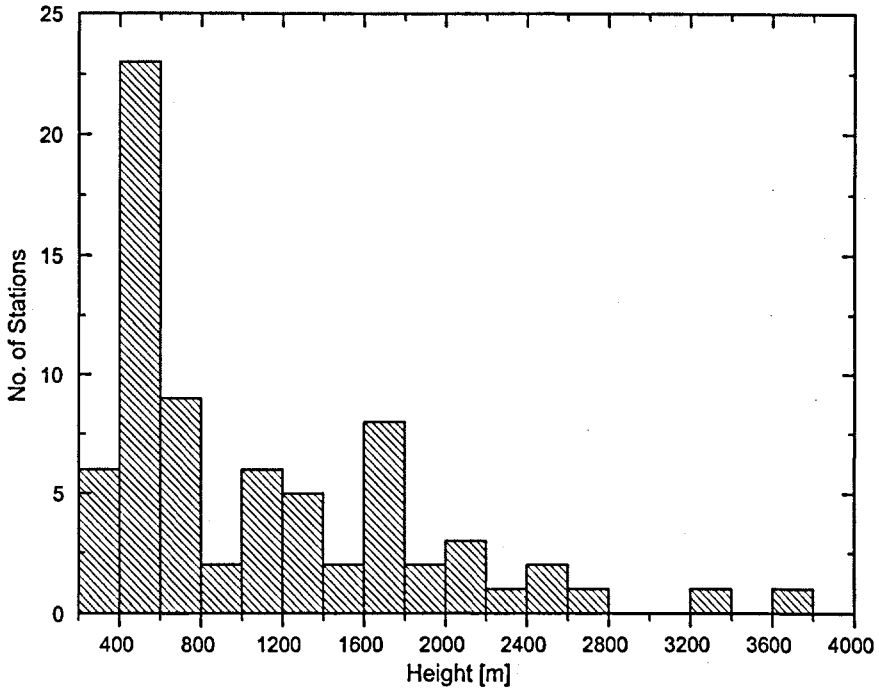

Figure 3.2: Histogram of the height distribution of the ANETZ stations with a bin size of 200 meters. About 50% of all stations have altitudes lower than 1000 m and 9 stations (12.5%) higher than 2000 m.

	COM2 [mm]	SAAS [mm]	WVR [mm]	GPS [mm]
mean difference COM1	-1.85	2.68	-0.52	0.09
standard deviation	1.96	2.53	1.56	1.89

Table 3.2: Mean differences and their corresponding standard deviations of the COM1 solution with respect to the four solutions COM2, SAAS, WVR, and GPS.

solutions the two results show anti-correlation. This is pronounced during the two periods where large deviations from the COM1 solution is observed. During these two periods the profiles show an inversion in the water vapor pressure profile. Three pairs of profiles calculated by COMEDIE are shown in Figure 3.4a,b and c. The profiles a1, b1 and c1 were calculated with radiosonde measurements and the profiles a2, b2 and c2 without radiosonde measurements. The corresponding IPWV from these profiles are marked with vertical lines in Figure 3.3b. During periods with temperature and water vapor inversion the Saastamoinen model fails because the assumed exponential decrease of water vapor in the lower atmosphere does not exist. In contrast the COM2 solution overestimates the water vapor profile during such

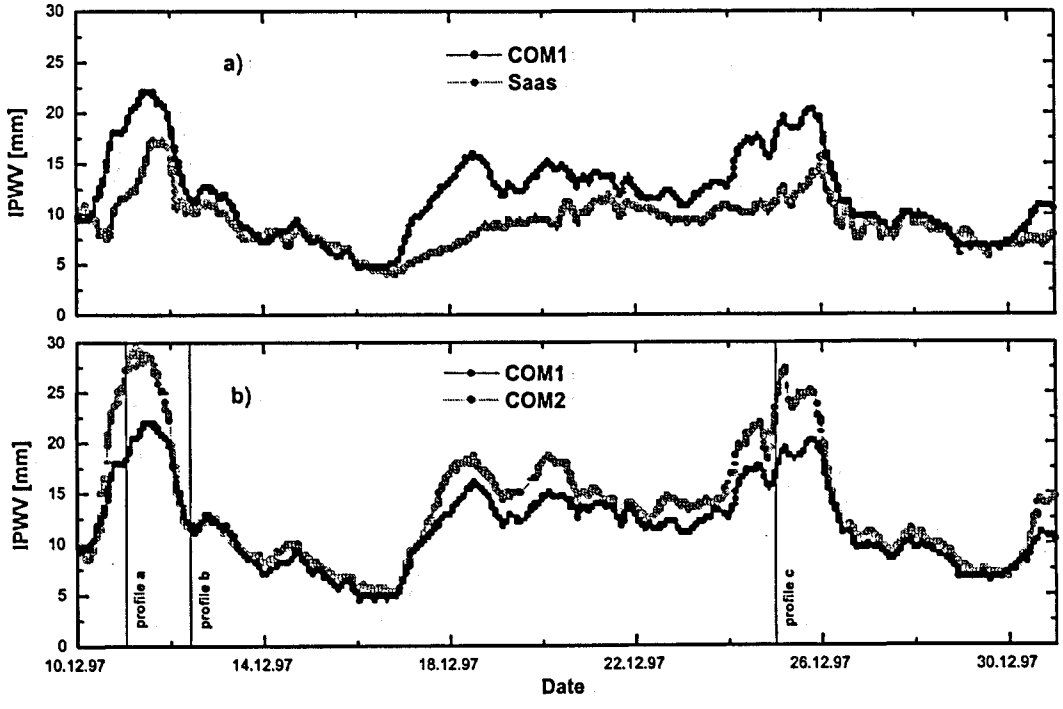

Figure 3.3: IPWV estimates from COMEDIE compared to a) Saastamoinen and b) COMEDIE without radiosonde measurements. 21 days of 15 minute estimates are plotted. The vertical lines in Figure b mark the IPWV values from the profiles in Figure 3.4.

periods. The least-squares fit of the water vapor scale height H_v (Eq. 3.4) highly depends on the distribution of the stations. In this example all stations around Zurich were below the inversion layer. If only stations below the inversion layer are used to estimate the scale-hight parameter H_e an increasing water vapor distribution with height would be the result. In the case of a bad estimated model the signal is only partly able to correct the model along the profile. The effect on the model parameters by introducing radiosonde measurements can be seen in the profiles of Figure 3.4a and c. The model calculated with the radiosonde measurements changes the entire profile towards a more rapid decrease of water vapor, however, the changes near the ground are minor. The effect of the signal content is visible in profile c1 and c2 in Figure 3.4. The two depressions at about 2000 and 3500 meters are caused by signal contributions from the two highest stations, used in this computation, at 2472 and 3580 meters. Between these two stations the model dominates the profile. The signal effect on profile c2 is more pronounced than on profile c1 which indicate that the model calculated with radiosonde measurements agree better with the measurements at these stations.

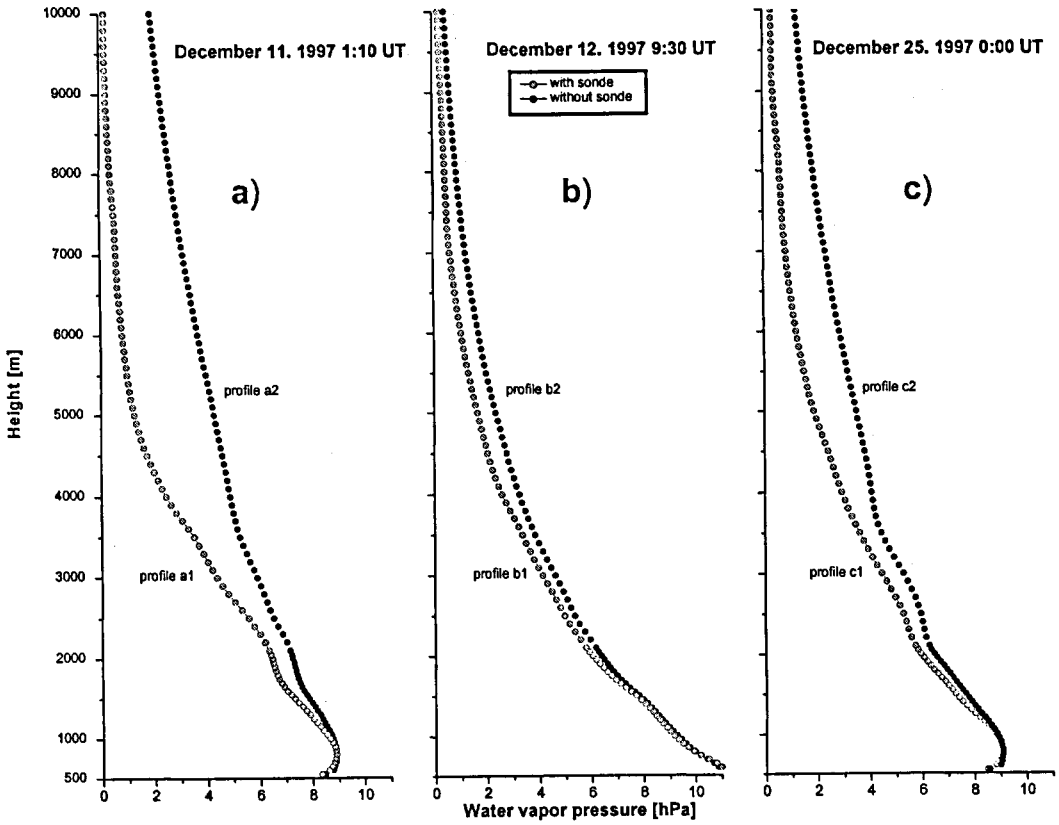

Figure 3.4: Water vapor pressure profiles at the ETHZ station estimated by COMEDIE (Figure a, b, and c). The profiles a1, b1 and c1 were calculated with radiosonde measurements and the profiles a2, b2 and c2 were calculated without radiosonde measurements. The water vapor pressure is overestimated when no radiosonde measurements are used. Figure a and c show an inversion of the water vapor pressure with height. The corresponding IPWV from these three profiles are marked with vertical lines in Figure 3.3b

The WVR and GPS estimates were included in this comparison for the validation of the COM1 solution. Details on the GPS and WVR processing are given in chapter 4 and 5. Figure 3.5 a and b shows the COM1 solution with estimates from GPS and WVR. The statistics of the comparison are listed in Table 3.2. Comparison of the GPS and WVR estimates gave a mean difference of -0.84 and a standard deviation of 1.23 mm. The gaps in the WVR time series were due to failure of the instrument. The absolute agreement of 0.09 mm between COM1 and the GPS estimates is regarded as good since comparisons with several WVRs (see chapter 4) showed larger offsets. However, some of the short-time fluctuations are not reproduced by the COM1 solution. This is pronounced during the time period C defined by the vertical lines in Figure 3.5a and b. Since there is no local profile information

available it is difficult to address the error. In general the COM1 solution shows a smooth behavior compared to the GPS and WVR estimates which is mainly caused by the temporal correlation length Δt.

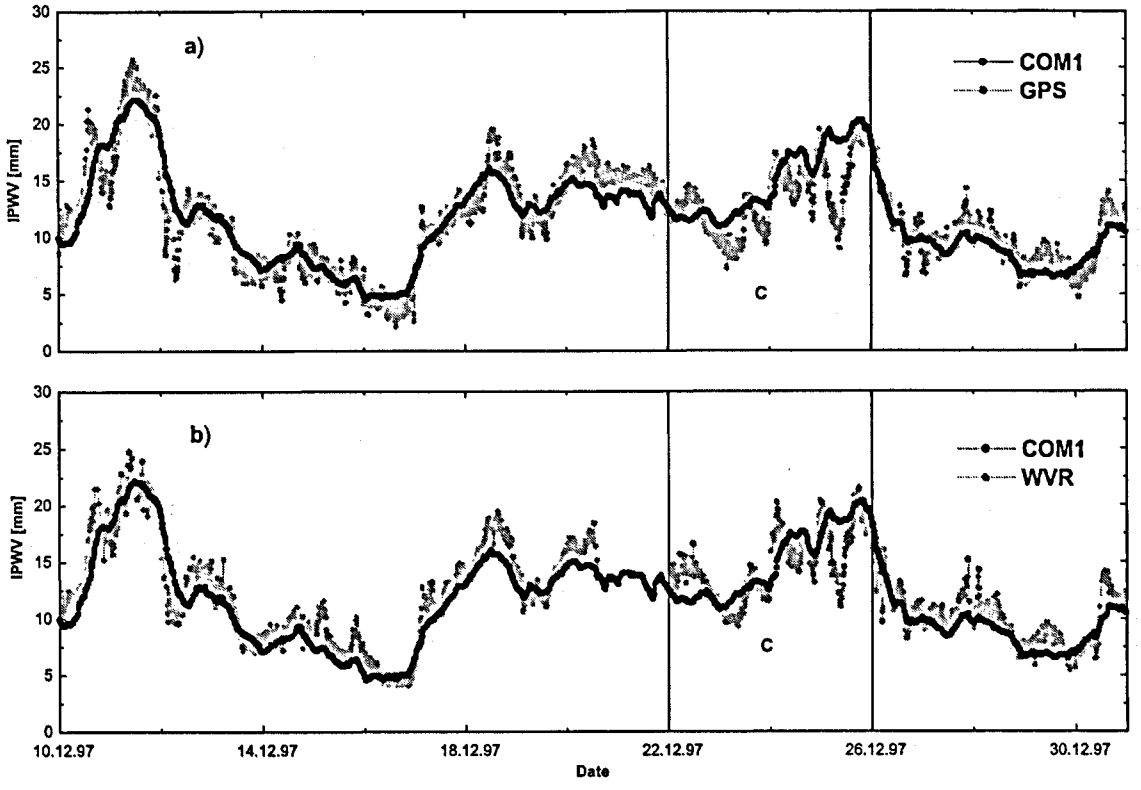

Figure 3.5: IPWV estimates from COMEDIE with radiosonde measurements (COM1) compared to **a)** GPS and **b)** WVR. The time series show 21 days of data with tropospheric water vapor estimates of 15 minute intervals. Rapid changes in IPWV detected by GPS and WVR within the time window C defined by the vertical lines are not reproduced by the COMEDIE solutions. The mean and standard deviation of the GPS - WVR difference is -0.84 mm and 1.23 mm IPWV

3.5 Conclusions

The modeling of tropospheric water vapor with the collocation method shows a good agreement with estimates from GPS and WVR. The accuracy of the modeling highly depends on the vertical distribution of measurements which in case of the Alpine topography is partly given. The results of the COM2 solution without radiosonde measurements show a general overestimation of the water vapor profile since measurements from ground stations dominate the fit of the water vapor scale height H_e.

The fit of the scale height parameter could be improved by constraining the water vapor pressure at high altitudes to zero. In contrast the Saastamoinen solution underestimated the water vapor content when an inversion layer was present. The lower water vapor pressure measured at the ground in combination with a standard profile of the water vapor misses the increase in water vapor pressure by default. In Table 3.2 the standard deviation of the COM1 - WVR differences is a little lower than compared to the standard deviation of the COM1 - GPS differences. However, the standard deviation of the GPS - WVR differences is smaller thus indicating that short-time fluctuations of water vapor are detected by both types of instruments.

The large fluctuations in water vapor content within the time window C in Figure 3.5a and b could not successfully be reconstructed by modeling. As discussed in the previous section the temporal correlation may be too long for some of the deviations. The time span of other deviations within this time window are, however, too long to be explained by the temporal correlation length. Such deviations are rather due to wrong modeling of the upper local water vapor profiles which are interpolated from distant Alpine stations. The deterministic model for the temperature lapse rate (Eq. 3.3) is assumed to be constant. This assumption is, however, only valid for a standard atmosphere below the tropopause. Introducing an additional model parameter to account for a temperature inversion at low altitudes might further improve the overall results of the modeling.

4 Microwave Radiometry

Passive microwave radiometers measure the intensity of radiation emitted by the atmosphere. Dual frequency water vapor radiometers usually operate at two selected wavelengths in the spectral vicinity of the water vapor rotational line centered at 22.235 GHz. One channel measures slightly off the line center and the second normally in the range 30 - 32 GHz. The channel close to the emission line center is more sensitive to water vapor while the other channel is more affected by liquid water (see Figure 4.1). The selection of optimal frequency pairs for dual channel radiometers is described in Elgered [1993] and Jarlemark [1997]. In this work data from the two ETH Water Vapor Radiometers ETH-Red and ETH-Blue were investigated and compared to WVR data from the geo-fundamental station Wettzell from the Bundesamt für Kartographie und Geodäsie and from the Onsala Space Observatory, Sweden. The ETH and Wettzell radiometers are portable dual channel radiometers developed at the Institute of Geodesy and Photogrammetry at the ETH Zurich in cooperation with the Institute of Applied Physics at the University of Berne and the CAPTEC-company [Bürki et al., 1992]. The Onsala radiometer ASTRID (Atmospheric Sky Temperature Radiometer for Interferometric Delay correction) is a dual channel radiometer permanently operated at the Onsala Space Observatory in Sweden. Within the WAVEFRONT [1999] project radiometer comparisons were carried out to estimate the absolute accuracy of the radiometers.

4.1 Absorption and emission in the atmosphere

4.1.1 Black-body radiation

The emission of electromagnetic radiation by the molecules of a body as they jostle in thermal agitation is analogous to evaporation from a wet surface, in case of saturated vapor. In case of dynamic equilibrium between the radiation field and the emitting surface, thermodynamics can be applied. A fundamental law named after Kirchhoff can be derived and expressed as follows:

$$E_\lambda = \alpha_\lambda f(\lambda, T) \tag{4.1}$$

where E_λ is the power radiated by unit area of surface per unit wavelength range centered at λ, a_λ is the spectral absorption coefficient of the surface (the fraction of incident radiation of wavelength λ absorbed by the surface) and $f(\lambda, T)$ is a universal function which varies only with wavelength and surface temperature.

Kirchhoff's law states that the efficiency of absorption of radiation of a certain wavelength by a surface is equal to its efficiency of emission of the same wavelength, where perfectly efficient emission is defined by the universal function $f(\lambda, T)$. Such an ideal surface is called a black body and its spectral distribution is described by Planck's law:

$$I(\lambda, T) = \frac{2\pi hc^2}{\lambda^5 \left[e^{hc/\lambda kT} - 1 \right]}, \tag{4.2}$$

where I is radiated power per wavelength interval, h = Planck's constant, k is Boltzmann's constant, T is temperature, c is speed of light. In the long wavelength limit where $hc << \lambda kT$, one can expand the exponential expression and obtain the classical Rayleigh-Jeans approximation of Planck's law. This approximation can be applied to radiometer frequencies:

$$I(\lambda, T) = \frac{2\pi ckT}{\lambda^4}. \tag{4.3}$$

From this expression it can be seen that the measured intensity power is linearly proportional to the equivalent temperature of black body target. This brightness temperature is used in radiometry as a measure of radiation intensity.

4.1.2 Brightness Temperature

The brightness temperature of the atmosphere at microwave frequencies is a sum of contributions from water vapor, liquid water and oxygen. With dual channel radiometers it is possible to separate the contributions from liquid water and water

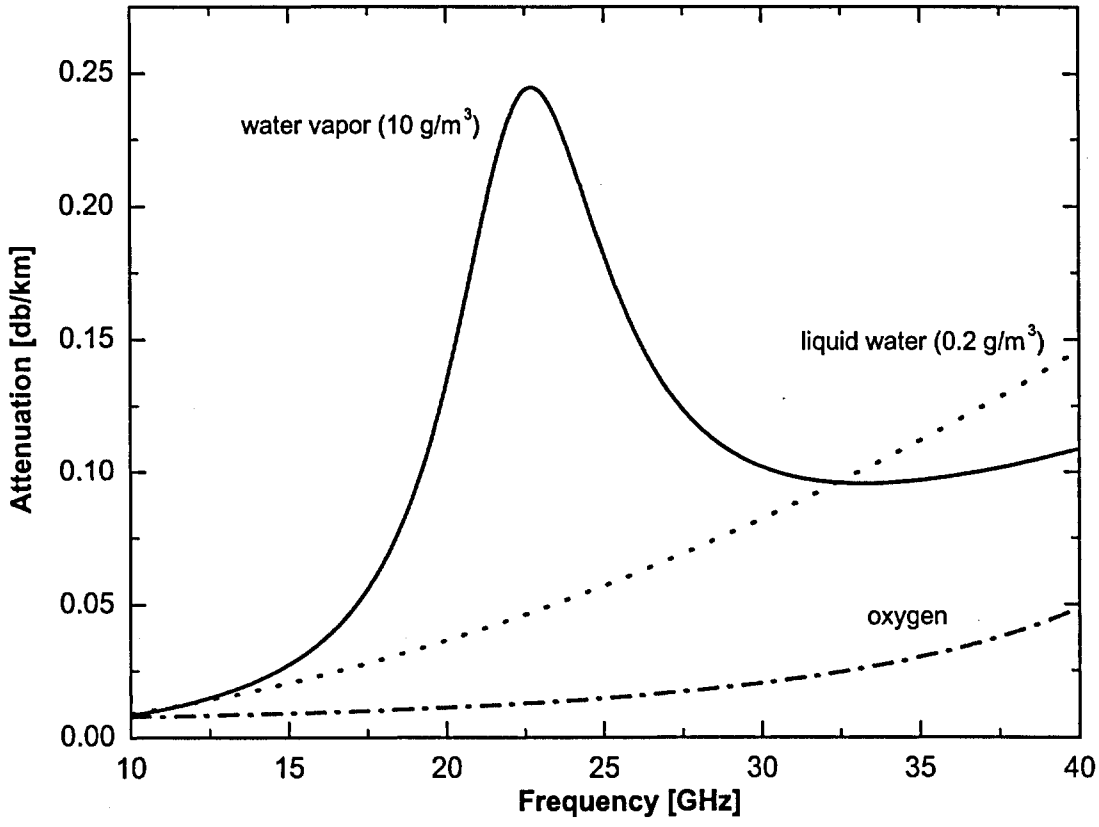

Figure 4.1: Atmospheric attenuation for water vapor, liquid water and oxygen in the range from 10 to 40 GHz. The solid and dashed lines are the attenuation spectra for water vapor and oxygen, respectively, given by Liebe [1992]. The dotted line represents the attenuation due to liquid water given by Staelin [1966]. The three spectra were calculated with a ground pressure of 1013 hPa and a ground temperature of 293 K.

vapor because they have different spectra (Figure 4.1). Using the Rayleigh-Jeans approximation (Eq. 4.3) and the radiative transfer equation Chandrasekhar [1960], we can write the observation equation for ground based radiometers as

$$T_s = T_{back} e^{-\tau_\infty} + \int_0^\infty T(s)\alpha(s)e^{-\tau(s)}ds \tag{4.4}$$

where

- T_s = Sky brightness temperature, the basic radiometer observable, [Kelvin]
- T(s) = The physical temperature at a point s along the optical path [Kelvin]

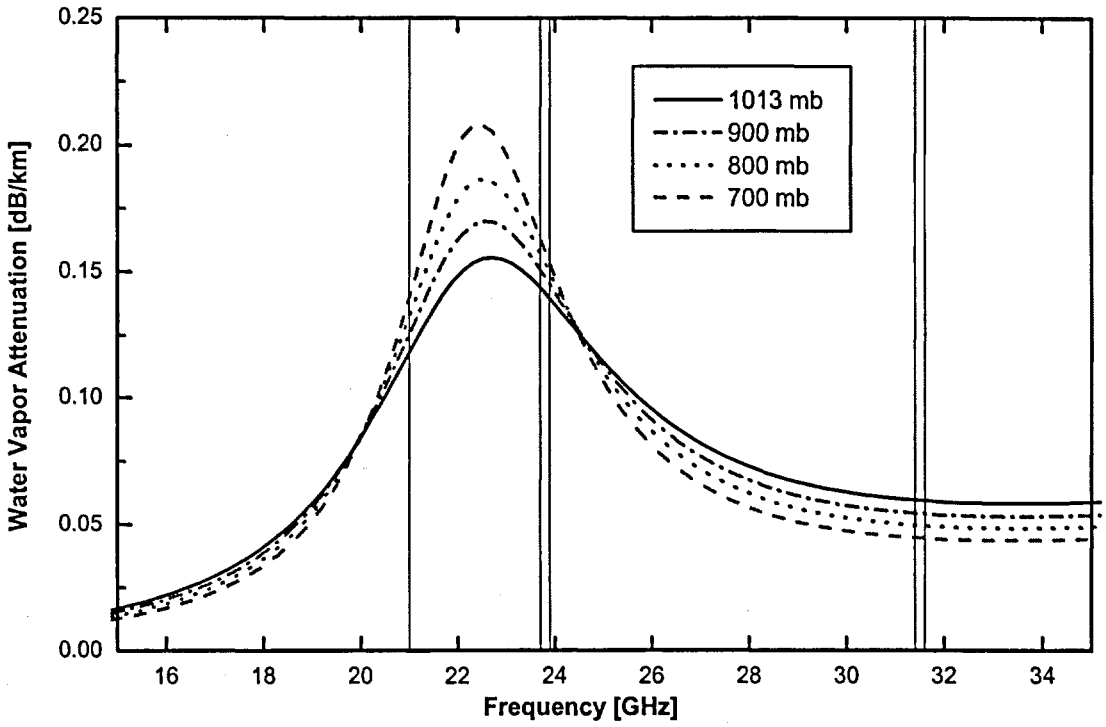

Figure 4.2: The effect of pressure broadening on the attenuation spectrum of a 50% humidity 15C atmosphere at 1013, 900, 800 and 700 hPa. At the two hinge points (around 20 and 24.5 GHz) the attenuation is unaffected by pressure variations. The receiving band widths of the ETH WVRs are shown at 23.8 GHz and 31.5 GHz. The lower frequency of the Onsala WVR, ASTRID, is marked at 21 GHz.

- $T_{back} = 2.8$K, the residual cosmic radiation from outer space [Kelvin]
- $\alpha(s) =$ is the absorption coefficient at s $[m^{-1}]$
- $\tau_\infty = \int_0^\infty \alpha(s)\, ds =$ opacity from the surface to outer space
- $\tau(s) = \int_0^s \alpha(s')\, ds' =$ opacity of the atmosphere from the surface to the point s along the optical path

Utilizing the Mean Value Theorem of calculus, one can approximate and partially linearize the above integral equation by introducing a mean atmospheric temperature defined as:

$$T_{eff} = \frac{\int_0^\infty T(s)\alpha(s)e^{-\tau_s} ds}{\int_0^\infty \alpha(s)e^{-\tau_s} ds} \tag{4.5}$$

Inserting this definition of the mean radiating temperature T_{eff} in Eq. 4.4 using the relation:

$$\int_0^\infty \alpha e^{-\tau} ds = 1 - e^{-\tau_\infty} \tag{4.6}$$

we get:

$$T_s = T_{back} e^{-\tau_\infty} + T_{eff}(1 - e^{-\tau_\infty}) \tag{4.7}$$

The exponential terms in Eq. 4.7 causes saturation effects for high opacities (e.g measurements at low elevation angles) and the measured brightness temperature becomes insensitive to changes in the water vapor content. for small opacities the relation is linear. It is therefore necessary to linearize the measured sky brightness temperatures at each frequency as well as the expression for the effective temperature T_{eff} to correct for these saturation effects. The expression of the linearized brightness temperatures [Wu, 1979] is defined as:

$$T'_s = T_{back} \cdot [1 - \tau_\infty] + \int_0^\infty T(s)\alpha(s) ds \tag{4.8}$$

The linearized effective temperature of the atmosphere is defined as:

$$T'_{eff} = \frac{\int_0^\infty T(s)\alpha(s) ds}{\int_0^\infty \alpha(s) ds} \tag{4.9}$$

Combining Equation 4.7, 4.8 and 4.9 the linearized sky brightness temperature is written as

$$T'_s = T_{back} - (T'_{eff} - T_{back}) \ln\left(1 - \frac{T_s - T_{back}}{T_{eff} - T_{back}}\right) \tag{4.10}$$

where T_{eff} and T'_{eff} are frequency dependent average temperatures of the attenuation medium and T_{back} is the background radiation equal to 2.8 K. The expression to calculate the effective temperatures of the atmosphere was taken from Jarlemark [1997]:

$$T'_{eff,f} = b'_0 + b'_1 \cdot T_{o,max} \tag{4.11}$$

$$T_{eff,f} = (b_0 + m \cdot b_1) \cdot T'_{eff,f} \tag{4.12}$$

The coefficients b_0 and b_1 in Eq. 4.11 are obtained with the method of least-squares, to estimate the effective temperature at each one of the observed frequencies from the daily maximum ground temperature $T_{o,max}$ and the airmass of the observation, m (see Table 4.1)

	b'_0	b'_1	b_0	b_1
22.73 GHz	62.16	0.7283	1.00004	1.37E-3
31.40 GHz	58	0.738	1.00002	9.80E-4

Table 4.1: Coefficients for the relation between a: T'_{eff} and daily maximum ground temperature and b: T_{eff} and T'_{eff} taken from Table 2 and 3 in Jarlemark [1997]. The coefficients can be applied without significant error. to the 23.8/31.5 frequency pair.

4.1.3 Absorption Coefficients

The total absorption coefficient α is the sum of partial absorption from water vapor, oxygen and liquid water:

$$\alpha = \alpha_v + \alpha_{ox} + \alpha_l \tag{4.13}$$

Three models for the water vapor absorption developed by Waters [1976], Liebe [1987] and Liebe [1992], hereafter called Water-76 Liebe-87 and Liebe-92, are shown in Figure 4.3. The shape of the absorption spectra is defined by line parameters with their center frequency for vacuum and parameters that describe the shape, strength and overlap of the line. The shape of an emission line in the microwave region is determined by the pressure- or collision broadening effect. In Figure 4.2 the effect of pressure broadening on the water vapor line is shown. Due to collision of water vapor molecules with mainly Nitrogen and Oxygen the rotational state of the molecule is disturbed. The range of allowed energy transitions increases proportional to the number of collisions and hence pressure. Several models have been proposed to describe the spectral line shape resulting from pressure broadening. The Liebe models Liebe [1985] uses the Van Vleck-Weisskopf [Vleck and Huber, 1974] line shape whereas Waters-76 uses the Gross line shape.

The line parameters depend on meteorological parameters such as pressure temperature and humidity. The models include continuum absorption contributions that are not taken into account by the line parameters. From Figure 4.3 it can be seen that the peak of the water vapor absorption line by Waters-76 is shifted to lower frequencies compared to the Liebe absorption models. The impact of water vapor absorption on radiometer data collected at 23.8 GHz is larger than at 21.0 GHz.

Jarlemark [1997] calculated the difference in the wet delay retrieved from algorithms based on the Liebe-92 model and the Waters-76 model to be on the order of 2% for a 21/31.4 GHz radiometer. Between the Waters-76 and Liebe-87 models a difference of 5% was observed.

Comparison of previous radiometer processing from the ETH radiometers with the Waters-76 absorptions model for water vapor and the [Wu, 1979] retrieval algorithm

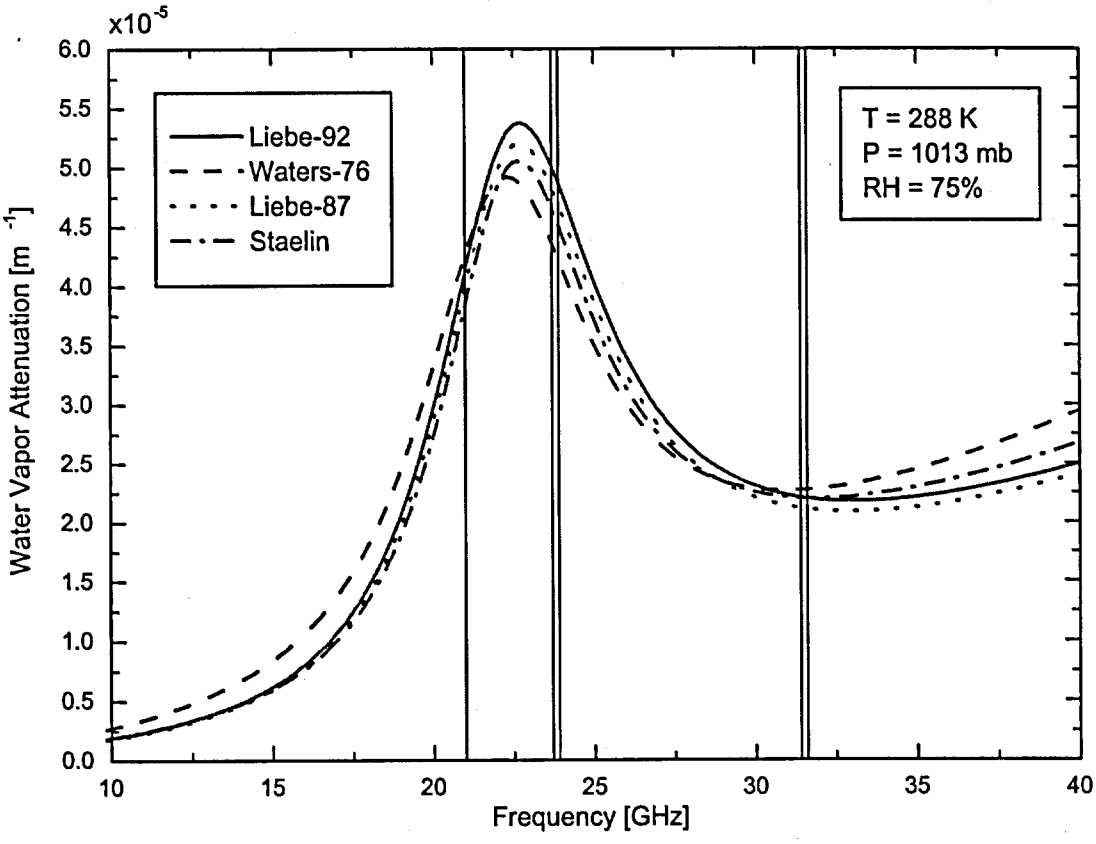

Figure 4.3: Water vapor absorption for various models in the range 10 to 40 GHz. The frequencies of the ETH radiometers are marked at 23.8 and 31.5 GHz. The frequencies of the WVR at Onsala (ASTRID) are 21.0 and 31.4 GHz. The double lines at frequencies of the ETH WVRs indicate the bandwidth of the instruments. The water vapor absorption models plotted show larger variation at 23.8 GHz than at 21 GHz.

showed a difference of up to 8% for path delays in the range of 26-28 cm compared with the Liebe-92 absorption model. [Cruz-Pol et al., 1998] made extensive comparisons of measured brightness temperatures with multi channel microwave radiometers and radiosondes. Their modified Liebe-87 water vapor absorption model confirmed the increased absorption of the Liebe-92 model compared to the Liebe-87 model. The Liebe-models are described in Liebe [1985]. The Liebe [1992] expressions of water vapor, oxygen and liquid absorption coefficients were used in this work.

4.1.4 Microwave profiling

The retrieval of temperature profiles by ground based instruments operating at microwave frequencies have been successfully reported by Westwater et al. [1975], Decker et al. [1978], Askne and Westwater [1986], Solheim and Keihm [1994]. These approaches exploit knowledge of the pressure broadening effect (see above). The absorption at each frequency along the flank of the spectrum, is a weighted sum of contributions from the water vapor profile. Because the distribution of Nitrogen and Oxygen with height is predictable from surface pressure measurements the broadening effect can be determined. First results from microwave water vapor profiling instruments have been presented by Solheim and Keihm [1994]. However, the required accuracy and frequency stability of the instrument is crucial.

The oxygen line complex at 60 GHz (Figure 4.4) is used to retrieve the temperature profiles by measuring the absorption at several frequencies close to 60 GHz. In addition to these frequencies Decker et al. [1978] introduced measurements at 22.235 and 31.65 GHz to correct for cloud liquid water droplets and water vapor contributions on measurements near 60 GHz in order to derive profiles of water vapor. The accuracy of the profiles was well above 1.0 g/cm^3 below 2 km. The results presented by Skoog et al. [1982] showed agreements with radio sonde profiles better than 1.0 g/cm^3. However the use of statistical information from radio sonde launches was necessary to derive the profiles in both cases. Recent developments of water vapor profilers have been reported by Solheim and Keihm [1994]. These instruments are capable of measuring in a tunable range of frequencies over the water vapor absorption spectrum and use the effect of pressure broadening to retrieve the water vapor profile.

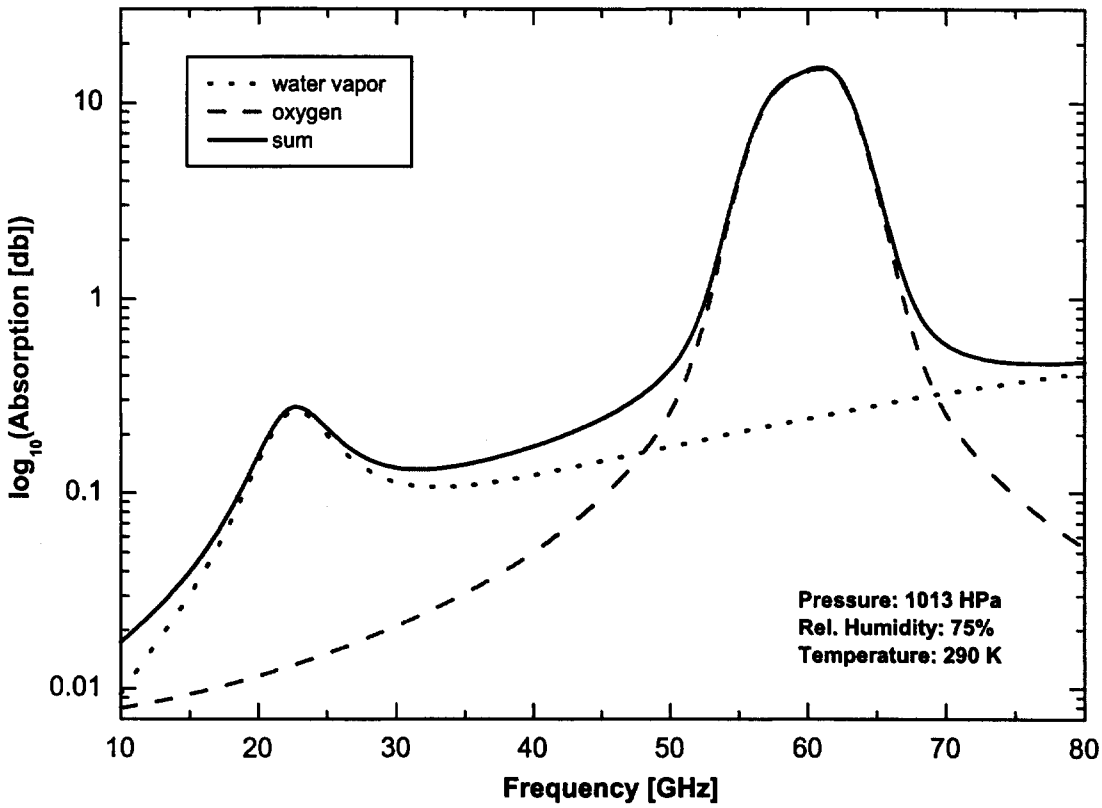

Figure 4.4: Water vapor and oxygen absorption in the 10 - 60 GHz range calculated with the Liebe-92 model for an atmosphere with 75% relative humidity, 1013 hPa ground pressure and a ground temperature of 290 K. Microwave temperature profilers measure the flank of the oxygen complex centered at 60 GHz whereas water vapor profilers measure the flank of the water vapor absorption line at 22.235 GHz.

4.2 Water Vapor retrieval algorithm

The retrieval of tropospheric path delay or precipitable water vapor from radiometric measurements requires an observation equation which relates the observable sky brightness temperatures with the quantity to be retrieved. While this could, in principle, be done for either IPWV or ΔL_w, in geodesy the latter quantity is used and transformed into IPWV using the expressions discussed in section 2.

The WVR data in this work have been processed using a retrieval algorithm proposed by Elgered [1993]. It uses a linear combination of the two observation frequencies to eliminate the radiation contribution of cloud liquid water. As can be seen in Figure 4.1 the two different phases of water exhibit different spectral absorption features. By forming the following linear combination of the observations, expressed in a quantity X as:

$$X = \left[\left(\frac{f_2}{f_1} \right)^2 T'_{s,f_1} - T'_{s,f_2} - T_{bg+ox} \right], \tag{4.14}$$

the influence of liquid water on the path delay estimation is minimized. T_{bg+ox} in Equation 4.14 is the combined contribution of the cosmic background radiation and the atmospheric oxygen to the sky brightness temperature. It can be modeled as

$$T_{bg+ox} = \left[\left(\frac{f_2}{f_1} \right)^2 - 1 \right] T_{bg} + \left(\frac{f_2}{f_1} \right)^2 T_{ox,f_1} - T_{ox,f_2}, \tag{4.15}$$

where T_{ox,f_1} and T_{ox,f_2} denote the brightness temperature of oxygen at the corresponding frequencies and $T_{bg} = 2.8\text{K}$ the constant cosmic background temperature.

The linear combination X is proportional to the wet path delay ΔL_w:

$$\Delta L_w = c \cdot X. \tag{4.16}$$

The constant of proportionality c depends on the meteorological conditions at the observation site and can be parameterized by the following expression:

$$\begin{aligned} c = c_{eff} \Big[1 &+ c_1 (P_o - \overline{P}_o) + c_2 (T_{o,max} - \overline{T}_{o,max}) \\ &+ c_3 (X - \overline{X}) \Big] \cdot (1 + 6 \cdot 10^{-5} T_{o,max}) \end{aligned} \tag{4.17}$$

The parameters for 6 selected stations are

- P_o: ground pressure at the WVR site
- $\overline{P}_o$: one year average of P_0 at the radiosonde site

Site	c_{eff} [cm/K]	c_1 $[hPa^{-1}]$	c_2 $[K^{-1}]$	c_3 $[K^{-1}]$	$\sigma_{0\ K}$ [cm]	$\sigma_{1\ K}$ [cm]
Landvetter 1997	0.3072	-0.840E-4	-0.320E-2	-0.110E-2	0.19	0.69
Munich 1997	0.2984	0.101E-3	-0.101E-2	-0.176E-3	0.20	0.64
Payerne 1997	0.2952	-0.165E-3	-0.456E-3	-0.357E-3	0.15	0.61
Madrid 1996	0.2849	-0.421E-4	-0.135E-2	-0.404E-4	0.24	0.63
Lihui 1999*	0.2889	0.260E-3	0.229E-3	-0.932E-4	0.09	0.61
Hilo 1999*	0.2884	0.622E-3	0.152E-3	-0.116E-3	0.11	0.61

Table 4.2: Inversion coefficients calculated with one year radiosonde dataset for the five sites Madrid (Spain), Landvetter (Sweden), Munich (Germany), Payerne (Switzerland) and Hawaii (Lihui and Hilo) at the frequency pair 23.8/31.5 GHz. *The coefficients for the two Hawaiian stations were calculated with data from December 1998 - April 1999 from radiosondes launched at noon local time. The standard deviations $\sigma_{0\ K}$ and $\sigma_{1\ K}$ represent the algorithm error for a noise-free radiometer (0 K) and for a radiometer with a brightness temperature noise level of 1 K.

- $T_{o,max}$ daily maximum of ground temperature at the WVR site
- $\overline{T}_{o,max}$ one year average of daily maximum of ground temperatures at the radiosonde site

The constants c_{eff}, c_1, c_2 and c_3 are determined in a least squares processing using the radiosonde dataset.

Assembling 4.16 and 4.17 finally yields the observation equation for WVR measurements:

$$\begin{aligned}\Delta L_w = c_{eff}\Big[1 + c_1(P_o - \overline{P}_o) + c_2(T_{o,max} - \overline{T}_{o,max}) \\ + c_3(X - \overline{X})\Big] \cdot (1 + 6 \cdot 10^{-5} T_{o,max})\ X.\end{aligned} \tag{4.18}$$

A detailed discussion on the performance of this observation model can be found in [Johansson et al., 1993] and in the appendix. Table 4.2 and 4.3 show inversion coefficients calculated with the Liebe [1992] water vapor, liquid water and oxygen absorption models (see also Figure 4.3).

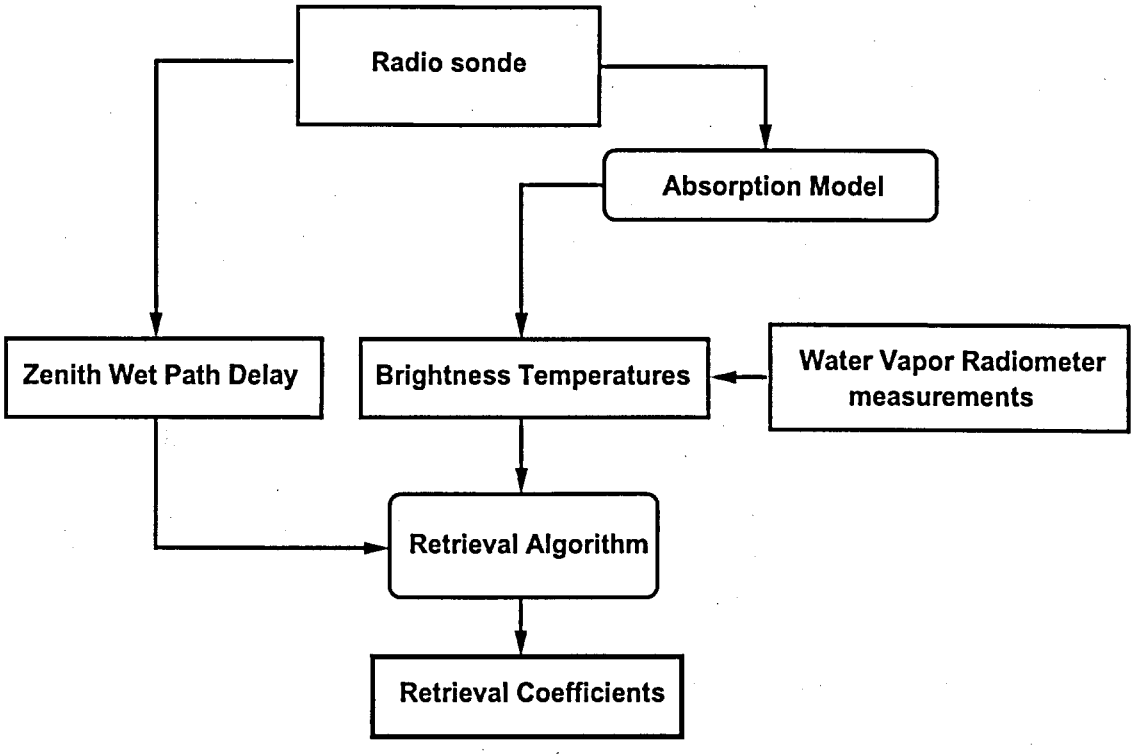

Figure 4.5: Flow diagram of processing retrieval coefficients from radio sonde information. The brightness temperatures are either calculated by absorption models using the radiosonde profiles or measurements from a microwave radiometer at the radiosonde launch site. The coefficients of the model described by the retrieval algorithm are estimated in a least-squares sense and called retrieval coefficients.

Site	$\Delta\overline{L}_w$ [cm]	σ [cm]	$\overline{P}_0$ $[hPa]$	σ $[hPa]$	$\overline{T}_{0,max}$ $[K]$	σ $[K]$	$\overline{X}_0$ $[K]$
Landvetter 1997	8.3	3.7	994.0	11.0	282.0	7.1	27.4
Munich 1997	8.5	4.0	961.3	7.8	283.9	8.82	28.6
Payerne 1997	10.2	4.4	961.0	7.3	283.6	11.3	34.6
Madrid 1996	9.3	3.5	943.4	6.4	289.7	9.3	32.5
Lihui 1999*	15.1	3.6	1014.1	2.2	293.5	2.1	51.6
Hilo 1999*	19.7	2.8	1017.5	2.1	291.9	0.9	67.0

Table 4.3: Mean values and standard deviations of the wet delay ($\Delta\overline{L}_w$), ground maximum temperature ($\overline{T}_{0,max}$), ground pressure ($\overline{P}_0$) and the quantity X as defined in 4.14 for the five sites. * The values for Lihui and Hilo were calculated with data from December 1998 - April 1999 from radiosondes launched at noon local time.

4.3 Water Vapor Radiometer Comparisons

Within the WAVEFRONT project two WVR comparison campaigns were carried out. The first campaign took place from 11.-20. of august 1997 at the Onsala Space Observatory, Sweden. The second campaign followed from 22.-30. of june 1998 at the Geo-FundamentalStation in Wettzell, Germany. The portable WVRs of ETH Zurich have been co-located with other continuously operating WVRs involved in the project, and GPS receivers. In order to achieve a consistent comparison between the WVR systems deployed in the project, the processing software for the ETH- and Wettzell Radiometers was updated. The main point was the adoption of the retrieval algorithm proposed by Johansson et al. [1993]. The retrieval algorithm puts more emphasis on the consideration of local meteorological and climatological conditions than the retrieval algorithm of Wu [1979], which was applied to the ETH data before the update. The calculation of the quantities introduced in the previous section was based on the the Liebe-92 atmospheric attenuation model [Liebe, 1992], which was already implemented in the processing software for the ASTRID Radiometer at Onsala. Introduction of these models yielded path delays of about 2 cm less than those calculated with the Wu [1979] retrieval algorithm and attenuation coefficients calculated with the Waters-76 model, which corresponds to about 8% of the total signal. An extensive intercomparison between the different instruments showed an agreement within their accuracy limits of about 1mm IPWV. The inherent biases between all WVRs have been determined. This provided a calibration data set for GPS-WVR comparisons within WAVEFRONT [1999].

4.3.1 WVR comparisons at Onsala

The dual channel WVR ASTRID at the Onsala Space Observatory operates since more than ten years. The goal of the before mentioned campaign was to compare measurements of water vapor from two different types of WVR's. The Onsala WVR measures the sky brightness temperature at 21.0 and 31.4 GHz while the ETH WVRs measure at 23.8 and 31.5 GHz. The antennas of the ASTRID radiometer collect the sky emission redirected by a mirror in front of the two antennas whereas the antennas of the ETH radiometers are pointed directly towards the source. Two ETH WVRs, in the following referred to as ETH-Red and ETH-Blue, were operated in co-location with ASTRID for 10 days. During this period each of the instruments recorded more than 60'000 measurements. Apart from the usual measurement mode, an experiment with synchronized pointing schedule for ASTRID and an ETH-WVR was performed in order to investigate the noise-level of the instruments.

4.3.1.1 Comparison Results

The time series of IPWV are plotted in Figure 4.6 and 4.7, indicating offsets between the instruments. The average standard deviation of the WVR estimates within the

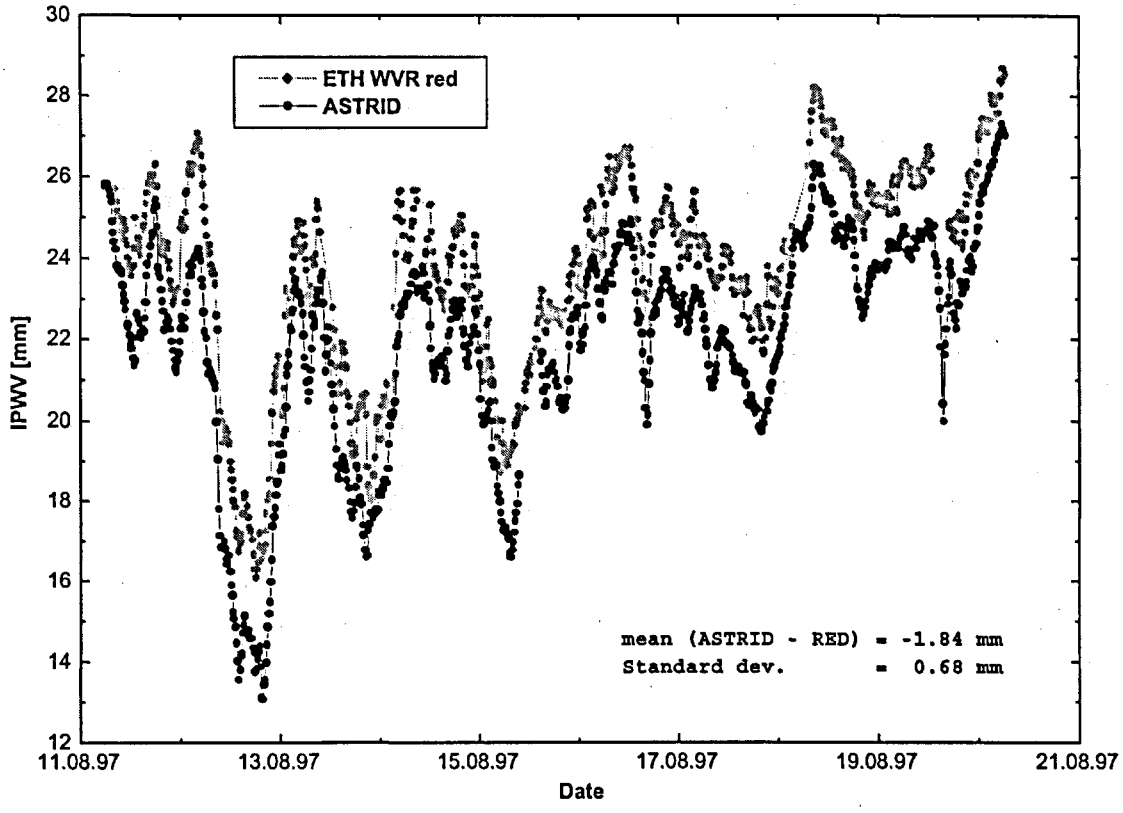

Figure 4.6: IPWV estimates from ETH-Red and ASTRID. The signature of the two curves shows good agreement with a standard deviation of 0.68 mm PW. The offset between the measurements was 1.84 mm PW (see also table 4.4)

15-minute intervals was 0.31 mm for ASTRID, 0.77 mm for ETH-Red and 0.98 mm for ETH-Blue. The 2-3 times higher standard deviation of the ETH-WVRs compared to ASTRID was caused by a higher noise level and a systematic elevation dependency of the calibration loads. Antenna and calibration loads were tested by pointing all instruments in one direction for about three hours. This should reduce possible effects generated by the antennas and the elevation dependencies of the microwave equipment. The experiment showed that the noise of the calibration loads was about a factor of two higher for the ETH radiometers than for the ASTRID radiometer. Jarlemark [1997] estimated the noise of the ASTRID radiometer to be about or better than 0.5 K which corresponds to a wet delay error of about 0.39 cm. Due to the higher noise level of the ETH Radiometers a standard deviation of about 1 K are expected which corresponds to a standard deviation of about 0.6 cm wet delay. The errors for the ETH radiometer with a standard deviation of 1.0 K brightness temperature is listed in Table 4.2. For a detailed discussion on the error estimates the reader is referred to the appendix in chapter 9.

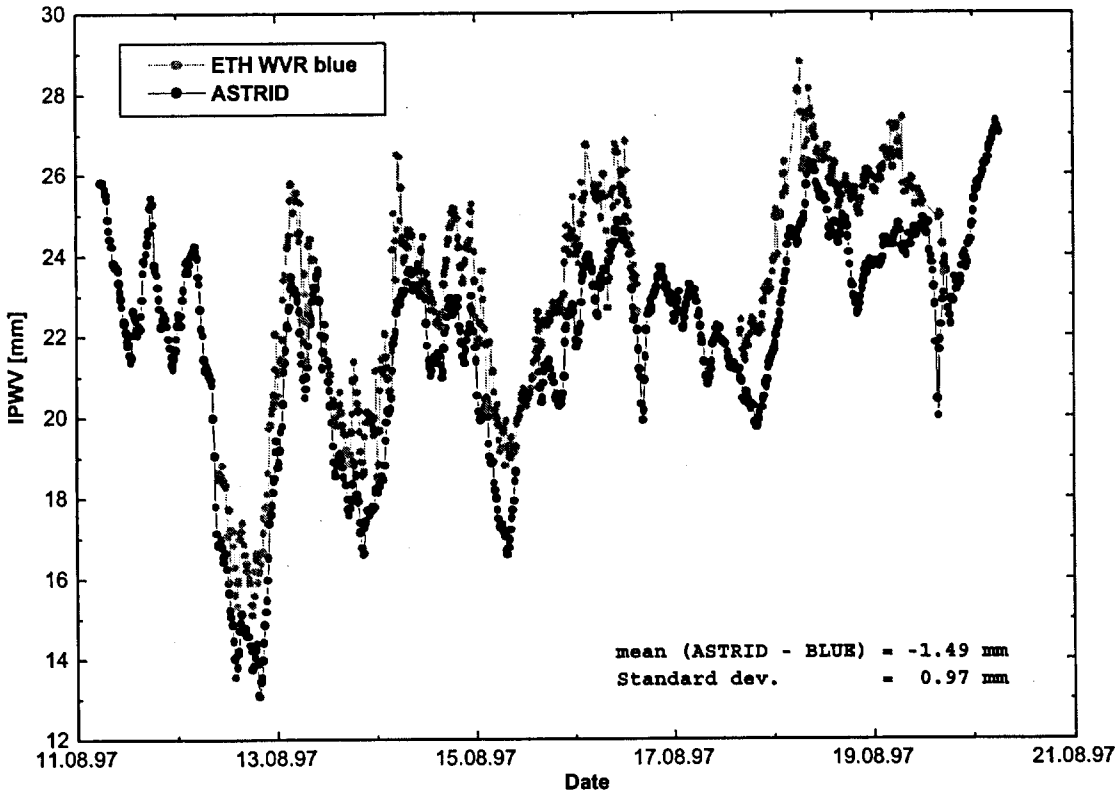

Figure 4.7: IPWV estimates from the WVRs ETH-Blue and ASTRID. Each point represent a mean of 15-minute intervals. Gaps in the ETH WVR blue data are caused by instrumental failures. A standard deviation of 0.97 mm and an offset of -1.49 mm between the two instruments were observed.

4.3.2 WVR comparisons at Wettzell

The Geo-Fundamental Station Wettzell of the Bundesamt für Kartographie und Geodäsie (BKG) in Germany operates three portable WVRs, which were constructed at ETH and CAPTEC. One of them is operated continuously at the co-located IGS station (WTZR). The 9-day-WAVEFRONT campaign started on June, 22nd 1998. Four dual-channel radiometer systems, one from ETH and three from BKG were deployed simultaneously, and measuring without interruption during 8 days. They will be referred to as ETH-Red, BKG-Yellow, BKG-White and BKG-Green.

4.3.2.1 Comparison Results

Table 4.4 shows the results from the comparison of the three BKG-WVRs with the ETH-Red Radiometer. The average standard deviation of the WVR estimates within the 15-minute intervals was 1.1, 1.3, 1.6 and 2.2 mm IPWV for the Red, Yellow, White and Green instrument, respectively. A major offset of BKG-Green and BKG-Yellow compared with ETH-Red was observed. The offset of BKG-Green is, however, reduced when compared to the ASTRID radiometer. The comparison with BKG-Yellow showed the smallest standard deviation whereas the standard deviations of the comparisons with BKG-Green and BKG-White are relatively large. In the case of BKG-Green the offset was due to an unstable hot load on the 23.8GHz channel. As can be seen in Figure 4.8 the offset between BKG-White and ETH-Red (upper plot) is shifted in the middle of the period, which is marked by the vertical line. The offset and standard deviation calculated before and after the shift (vertical line) is 1.03/1.71 and -2.79/2.43 respectively. Up to now the reason for this offset is not fully understood. Therefore the offset and standard deviation listed in Table 4.4 may not be representative for the instrument.

4.3.3 WVR calibration tables

Table 4.4 shows the results of the WVR intercomparison. In the first line, the biases of the WVRs are plotted with respect to the ETH-Red instrument. To achieve a standard for comparison, the ETH-Red is calibrated with respect to the ASTRID WVR (using the results from the Onsala campaign 1997). The corresponding new offsets are plotted in the second line of table 4.4 (Figure 4.8).

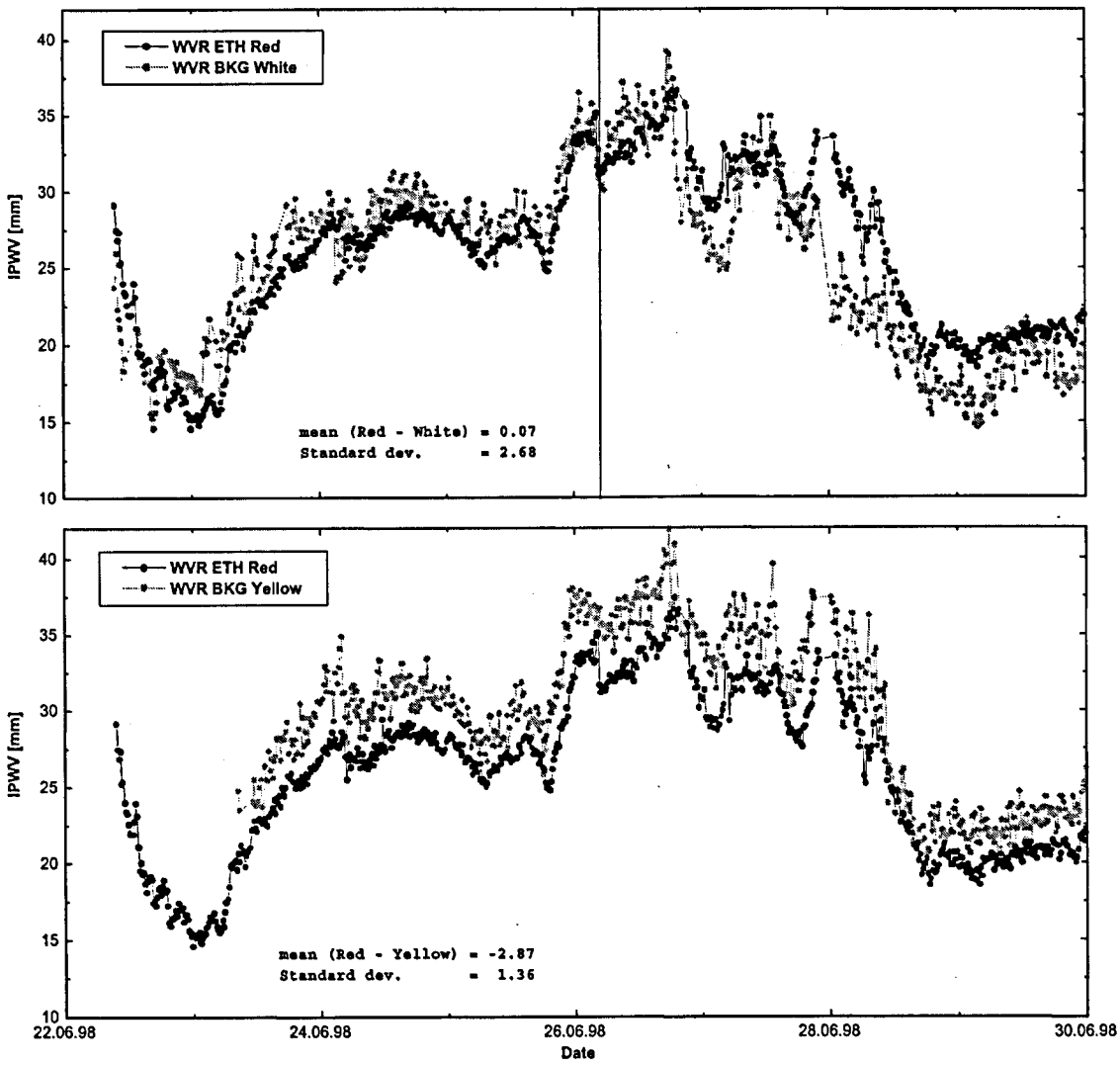

Figure 4.8: WVR IPWV estimates from ETH-Red, BKG-Yellow and BKG-White at the Geo-Fundamental Station Wettzell. The four curves show mean-values of 15 minute measurements, which corresponds to a complete scan of the hemisphere. The offset between BKG-White and ETH-Red (upper plot) is shifted in the middle of the period, marked by the vertical line. The offset and standard deviation calculated before and after the vertical line is 1.03/1.71 and -2.79/2.43 respectively.

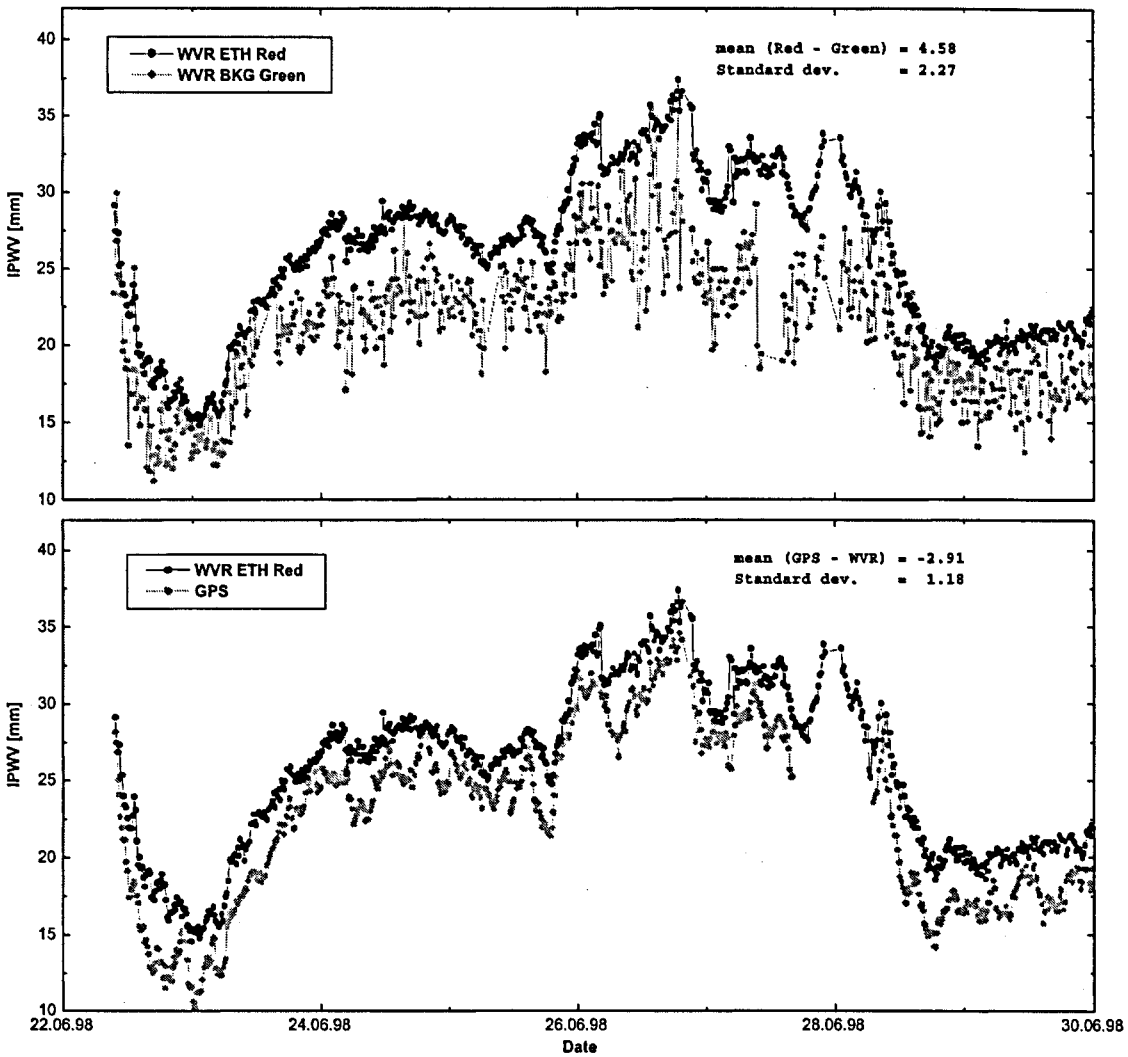

Figure 4.9: IPWV estimates from ETH-Red, BKG-Green and GPS at the Geo-Fundamental Station Wettzell. The four curves show mean-values of 15 minute measurements, which corresponds to a complete scan of the hemisphere.

Difference/WVR	Red [mm]	Green [mm]	White [mm]	Yellow [mm]
Δ_{PW} RED-WVR	0	+4.58	+0.07	-2.87
Δ_{PW} ASTRID-WVR	-1.84	+2.74	-1.77	-4.71
σ	0	2.27	2.68	1.36

Table 4.4: Calibration table of the four WVRs relative to ASTRID. ETH-Red is used as a calibration link between the Wettzell WVRs and ASTRID.

5 GPS Meteorology

5.1 Introduction

The Global Positioning System (GPS) is a constellation of 24 active satellites maintained by the U.S Department of Defense for military and civil navigation purposes. The satellites are distributed on six orbital planes which are inclined by 55^o with respect to the Earth's equator and separated by 60^o on the equator. The orbital planes are almost circular with a semi major axis of about 26'000 km which is equivalent to a zenith distance of about 20'000 km observed from the surface of the Earth. The orbital revolution of a GPS satellite is about 11 hours and 58 minutes corresponding to 12 hours sidereal time. Each GPS satellite is equipped with rubidium and cesium oscillators which are used to generate two carriers L1 and L2 with frequencies f_1 and f_2. The two frequencies are generated by multiplying the fundamental frequency $f_0 = 10.23MHz$ by 154 and 120, respectively.

5.2 Observation equation

This section is a brief treatment of the basic GPS observation equations used in this work. For a detailed discussion on GPS the reader may consult, e.g. [Seeber, 1993], [Teunissen and Kleusberg, 1998]. GPS receivers measure the difference between the phase generated by the satellite at the time of transmission and the phase generated by the receiver at reception time. The observation equation for the carrier phase observation L_r^s in units of length can be written as:

$$L_r^s = \rho_r^s + c(\Delta t_r + \Delta t^s) + \Delta\rho_{r,trop}^s + \Delta\rho_{r,ion}^s + \lambda N_r^s + \epsilon \tag{5.1}$$

where

L_r^s is the carrier phase observation in units of length between satellite s and receiver r

ρ_r^s is the geometric distance between receiver r and satellite s

$c = 299'729'458\ m/s$ is the speed of light in vacuum

Δt_r and Δt^s are receiver and satellite clock offsets

$\Delta\rho^s_{r,trop}$ is the tropospheric path delay

$\Delta\rho^s_{r,ion}$ is the ionospheric path delay

N^s_r is the initial phase bias

λ is the wavelength of the carrier

ϵ is the error or residual

The satellite to receiver range ρ^s_r is defined by

$$\rho^s_r = \sqrt{(X_r - X^s)^2 + (Y_r - Y^s)^2 + (Y_r - Y^s)^2} \tag{5.2}$$

where (X, Y, Z) are geocentric coordinates of the receiver and satellite indicated by the suffixes r and s, respectively. The International GPS Service (IGS) provides high precision coordinates of the satellites orbits with accuracies better than 5 cm [Kouba and Mireault, 1998] (see also section 5.5.2). The ionospheric delay $\Delta\rho^s_{r,ion}$ depends on the frequency and is eliminated using a linear combination of dual frequency observations. This linear combination was used throughout this work and will not be further discussed here. Details on ionospheric refraction can be found in the GPS literature referenced above and in a recently published Ph.D Thesis on this subject by Schaer [1999]. In contrast to the ionosphere the troposphere is not dispersive for frequencies below 40GHz and the delay term $\Delta\rho^s_{r,trop}$ can therefore not be eliminated by linear combinations of observations. The tropospheric delay term therefore has to be modeled (see chapter 3) or estimated as an additional parameter in the processing in order to get accurate coordinate estimates of the receiver position. The satellite clock bias Δt^s is removed by differencing observations from two receivers with respect to a satellite. The phase difference between two receivers i and j measuring simultaneously the signal from the same satellite k

$$L^k_{i,j} = L^k_i - L^k_j \tag{5.3}$$

eliminates common effects such as the satellite clock offset Δt^s

$$L^k_{i,j} = \rho^k_{i,j} + c\Delta t_{i,j} + \Delta\rho^k_{i,j,trop} + \Delta\rho^k_{i,j,ion} + \lambda N^k_{i,j} + \epsilon \tag{5.4}$$

Differencing of single difference observations at the same epoch eliminates the receiver clock offset Δt_r.

$$L_{i,j}^{k,l} = \rho_{i,j}^{k,l} + \Delta\rho_{i,j,trop}^{k,l} + \Delta\rho_{i,j,ion}^{k,l} + \lambda N_{i,j}^{k,l} + \epsilon \tag{5.5}$$

Observations of this type are called double difference observations and are the primary observations used in the Bernese Software version 4.0 [Rothacher and Mervart, 1996]. The resulting double difference phase bias $N_{i,j}^{k,l}$, the so called phase ambiguity is an integer. It is estimated during the processing of the GPS data. The major advantage of the double difference technique or baseline method is the removal of the receiver and satellite clock offsets which would have to be modeled when zero difference observations (Eq. 5.1) were used. The method using zero differences is often referred to as the point positioning method.

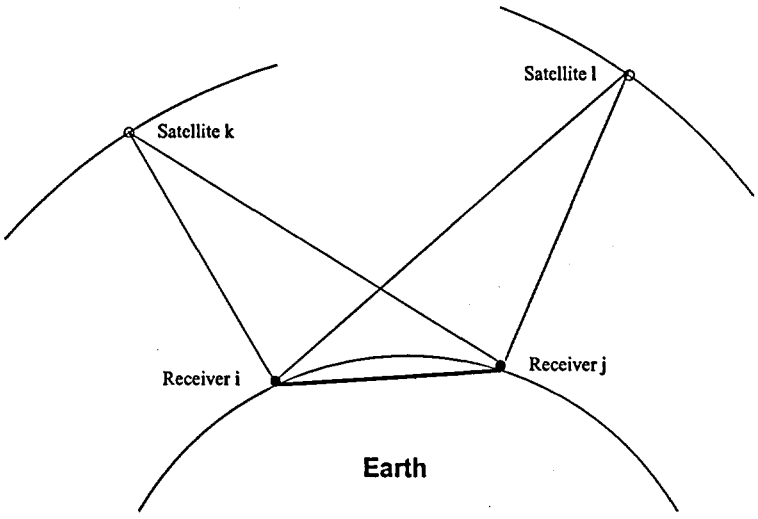

Figure 5.1: Constellation of two receivers and two satellites with their corresponding ray paths. The four observations are used to form one double difference observation. The straight line between the receivers is called baseline.

5.2.1 Coordinates and Tropospheric Parameters

Assuming a homogeneous distribution of satellite observations over the hemisphere [Geiger, 1987] showed that a systematic range error, such as tropospheric delay is amplified by a factor of 3 in the vertical, whereas the horizontal components remain unaffected. If the Total Zenith Delay (TZD) is not modeled at all, the height is biased by about 6 to 8 m. On the other hand, an error in the height of 1 cm will lead to a delay error of about 3.3 mm. In Figure 5.2 the relation between formal errors of height and troposphere for different cut-off angles are shown. Three coordinates and twelve tropospheric parameters were estimated per day. Five IGS and 10 GPS stations from the Hawaiian campaign were used. The formal errors of

the daily mean troposphere estimates are plotted against formal errors of the daily height estimate. The straight line is a linear fit of the data with respect to the height errors and can be interpreted as a ratio of the formal errors of tropospheric height parameters. This ratio decreases with increasing elevation cut-off angle from 4.6 at 10 degree to 3.2 at 30 degree elevation cut-off. A one to one relation of height and tropospheric errors is in theory (with a homogeneous satellite distribution) achieved at a cut-off of close to zenith. However, real distributions of satellites are far from being homogeneous since in general more satellites are visible below 45 degrees than above this angle.

From Figure 5.2 it can be seen that the formal errors of the parameter estimates decrease with decreasing elevation cut-off since the strength of the observation geometry is improved. On the other hand the a posteriori RMS is improved by increasing elevation cut-off angles because data are noisier at low elevation angles and contributions from tropospheric model imperfections at low elevation angles are highly reduced.

Tropospheric effects can be corrected for by introducing external information of the tropospheric path delay such as meteorological models and measurements from WVRs in the GPS processing. The potential bias of this information is, however, important due to the error propagation discussed above. A way to avoid the requirement of absolute accuracy is to estimate one tropospheric parameter per day or over the whole period to correct for a possible bias of the a-priori values. This method reduces the number of parameters to be estimated but allows a potential bias of the coordinate estimates. Wiget et al. [1999] compared heights from precise leveling and GPS estimates for a wide range of station altitudes in the Swiss Alps. The differences showed a scale factor with height of about 9.5 mm/km. This scale factor could be removed by applying meteorological models (see chapter 3) and estimating one troposphere parameter every 48 hours. Estimation of tropospheric delay by introducing external information from precise barometers and WVRs in the processing of the GPS observables have shown that sub-centimeter accuracy of the height component is possible [Alber et al., 1997]. The high correlation between height and troposphere parameters can, however, be separated because of the elevation dependency of the tropospheric delay. This elevation dependency of the tropospheric delay is modeled by mapping functions. The Hopfield [1969] mapping function was used in this work. For measurements in the zenith direction the correlation of the delay and the height component is 100% and with decreasing elevation this correlation is reduced to 0 at 0^o elevation. However, real observations are made at elevations ranging from zenith to a certain cut-off angle and the correlation factor is somewhere in between these limits (see above and Figure 5.2). Low elevation angle measurements improve the observation geometry and are therefore required to de-correlate height and tropospheric estimates.

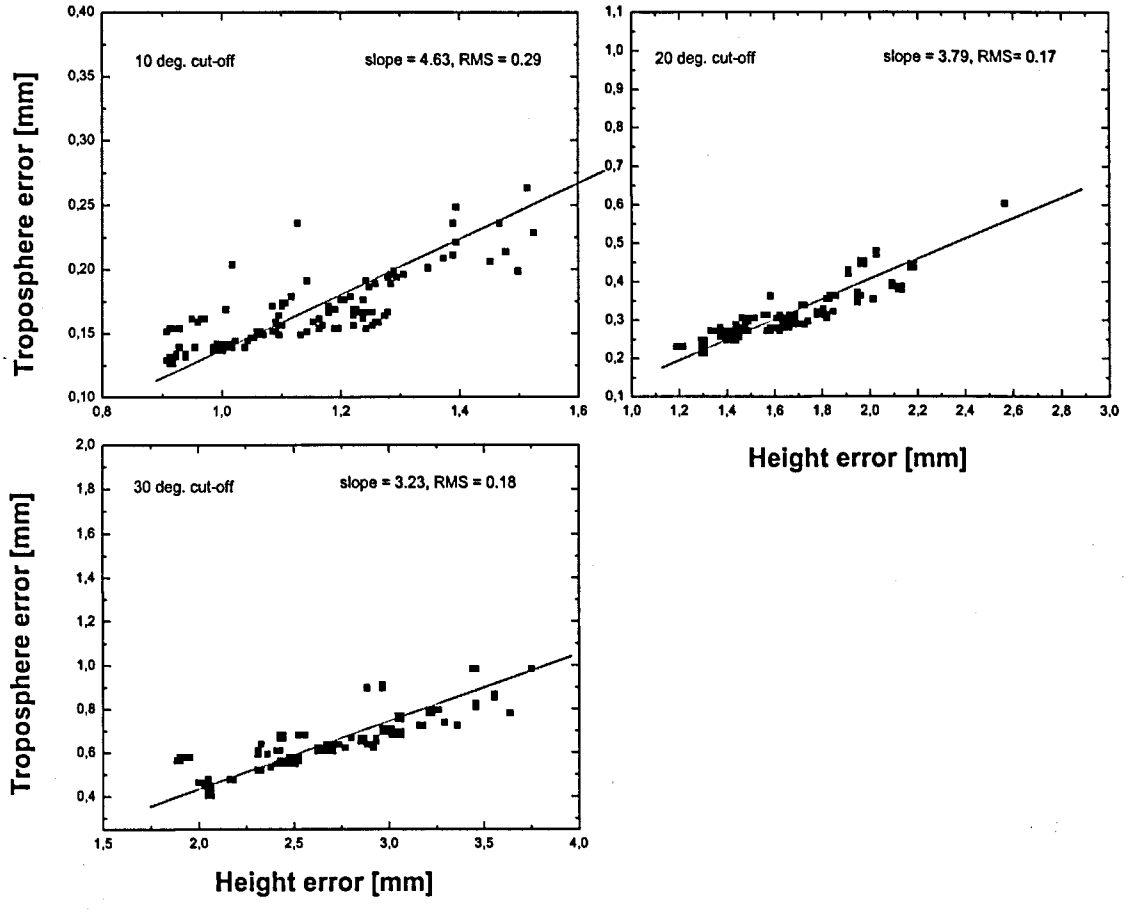

Figure 5.2: Proportionality factors between formal errors of height and zenith path delay estimations in mm for three different elevation cut-off angles at 10, 20 and 30 degrees. Five IGS and 10 GPS stations from the Hawaiian campaign network were used. The factor of proportionality decreases with the cut-off angle from a factor of about 4.63 at 10 degree to about 3.23 at 30 degree. The overall noise level of the parameters increase with increasing elevation cut-off angle.

5.3 Estimating tropospheric parameters with GPS

GPS meteorology is based on simultaneous observations of signal delays from satellites at different elevation angles. Modern software packages based on least-squares techniques evaluate observations of a network of receivers. In a multi-station analysis tropospheric delay parameters can be estimated in regular time intervals for each receiver. In order to retrieve IPWV the contribution of the dry air is removed from the estimated total delay using the known ground pressure Davis et al. [1985]. The

obtained ZWD is converted into IPWV as discussed in chapter 2.

In a local GPS network it is possible to estimate relative changes of ZWD between the stations, because the absolute tropospheric parameters recovered at closely spaced stations are highly correlated. The elevation of the satellite is almost identical for short baselines. Furthermore, differencing of phase observations between satellites and stations, which is performed in the GPS analysis to cancel unmodeled variations of the clock oscillators, reduces the sensitivity to the absolute values of station, orbital and atmospheric parameters. These problems can be overcome by incorporating widely separated stations (> 800 km [Baker, 1998]) into the GPS network. In this case the different stations receive the same satellite signal at significantly different elevation angles. The introduction of such long baselines reduces the correlation of tropospheric parameters within the network and therefore allows absolute estimations of ZWD [Bevis et al., 1992; Duan et al., 1996].

5.3.1 Accuracy of GPS Estimated Tropospheric Parameters

In order to achieve the best parameter estimates careful modeling of error sources is required. The requirements of sub-centimeter accuracy of the vertical coordinate component has led to a variety of model improvements such as mapping functions, antenna phase center variations, gradient estimation etc.. However, due to the geometry of the station satellite configuration the height component and the tropospheric parameters are highly correlated. The a posteriori RMS errors of tropospheric and height estimates given by the Bernese GPS Software are known to be much too realistic [Rothacher, 1999]. The formal errors of zenith total delays (ZTDs) and height are in general within 0.9 - 1.4 mm and 1 - 3 mm, respectively. A more realistic measure of the height error is the daily repeatability of the height component which is normally in the range 6 - 12 mm.

For tropospheric estimates calculated with a 10 degree elevation cut-off angle a proportionality factor of 1/4,63 (see Figure 5.2) can be used to estimate the error of the ZTD estimates. With this factor an error of 10 mm in the height component corresponds to a ZTD error of 2.15 mm. With 24 tropospheric estimates per day the number of observations used to calculate the height component is 24 times higher compared to the number used for the tropospheric estimates. Therefore an error of 2.15 mm TZD may be too optimistic.

The too small formal error estimates are mainly caused by neglecting the correlation between consecutive measurements. Every epoch is treated as independent. The stochastic errors described above are unaffected by potential systematic errors which may bias the results. Recently Springer [1999] calculated the range difference between *Satellite Laser Ranging* (SLR) measurements and GPS estimates of the orbits of satellite PRN5 and PRN6 to 54 mm. The reason for this bias is not yet known. Errors in antenna-phase center models and multi-path effects are further

sources that may bias the results. Comparisons with independent measurements of water vapor are therefore required in order to validate tropospheric GPS estimates.

5.3.2 GPS processing scheme

All GPS results presented were processed with the Bernese Software Version 4.0. The pre-processing of the GPS data corresponds to a standard processing scheme which is described in detail in the User's Guide of the Bernese GPS Software [Rothacher and Mervart, 1996]. Daily coordinate solutions from the GPS campaign network stations are estimated by introducing observations from several IGS core stations fixed to coordinates defined within the ITRF coordinate reference frame. With these daily coordinate solutions a mean position is calculated. For long term observation periods it might be required to estimate the velocity of the station to adjust for plate tectonic motions. In the final processing step tropospheric parameters are estimated by fixing all station coordinates on their respective values. By fixing coordinates on their mean positions one assumes no movement of the antenna during the period of observation. The scatter of the daily solutions around the mean value is thereby regarded as noise. To account for the short term variability of tropospheric water vapor, parameters have to be estimated within intervals depending on the size of water vapor fluctuations at the site of interest. Tropospheric parameter estimations within the Bernese GPS software are set up in time intervals defined by the user. The estimates are mean values of tropospheric refraction in the directions defined by the current satellite constellation mapped to zenith. From comparisons with WVR data, estimation interval lengths of 15 minutes was regarded as sufficient to detect short time variations. However, tight constraints on the estimates have to be applied for such short intervals since the amount of data available and the strength of the observation geometry is not sufficient for reliable estimates.

Figure 5.3a and b show different constraints applied on 15 minute, 1 and 2 hour estimates compared with WVR data at the Onsala site. The one and two hour estimates changes only slightly by tightening the tropospheric constraints because the number of observations reduces the effect of the constraints. The effect on 15 minute estimates is much more pronounced by the size of the constraints and approaches the values of the 1 and 2 hour estimates with increasing constraints. Similar results have been shown by Baker [1998]. In Figure 5.3 daily coordinates of the Onsala site were estimated together with tropospheric parameters. The bias between the GPS and WVR estimates increases by about 0.5 cm wet path delay whereas the differences between the estimate intervals are reduced. The increased bias of the GPS - WVR difference is coupled with a change in the coordinate height of the Onsala station of 12 mm. The example shows that estimation of campaign station heights depends on the network used. Such biases of the height component propagate into the tropospheric estimates because of the high correlation between these two parameters (see also Figure 6.8).

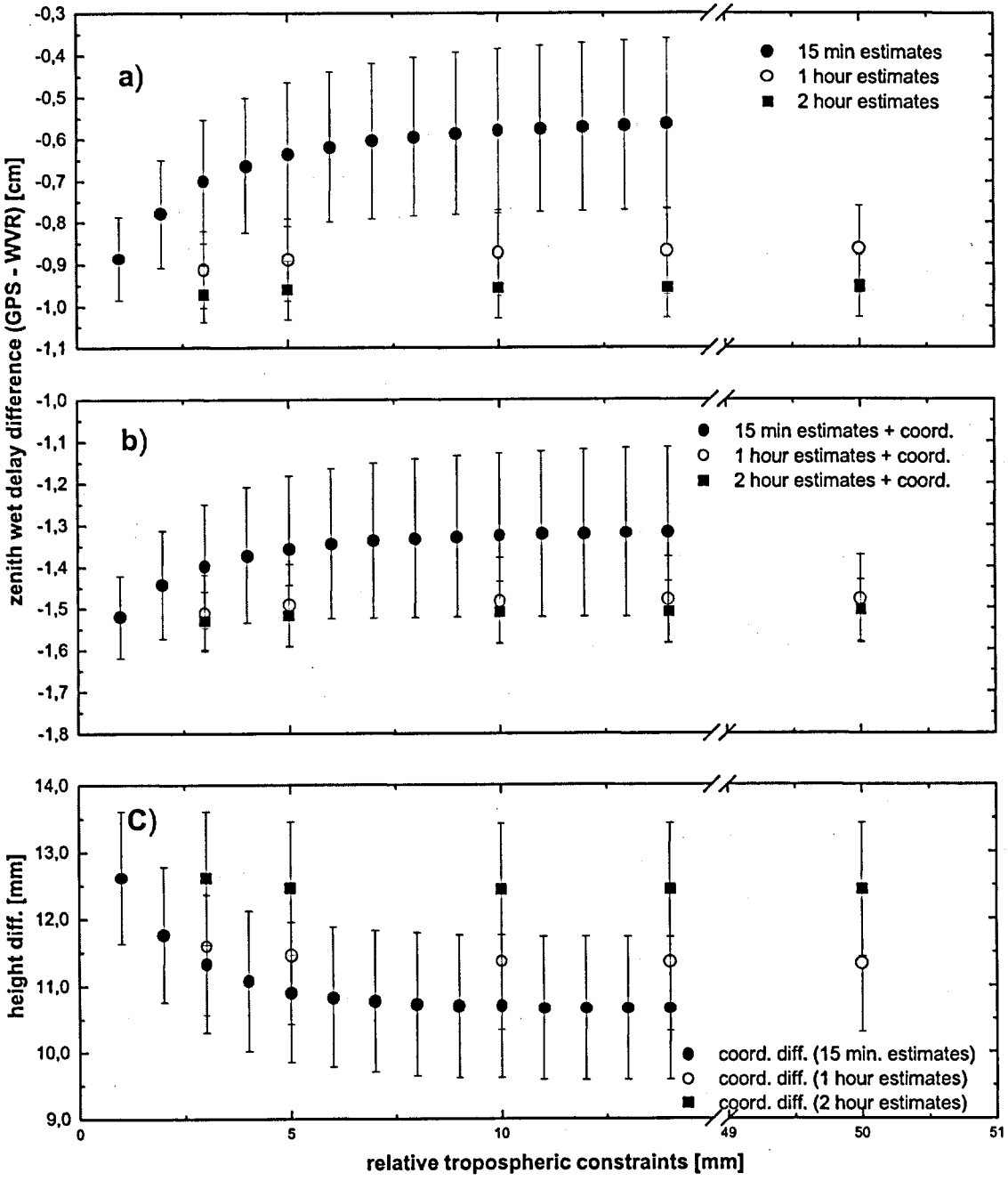

Figure 5.3: Constraints on tropospheric GPS estimates and their effect on the absolute estimates compared with WVR. a and b) Each point represents the mean difference of ten days of continuous GPS and WVR data from the Onsala site. The error bars are mean formal errors of the tropospheric estimates. Three estimation intervals of 15 minutes, 1 and 2 hours are plotted (see legend). **a)** Coordinates of the ONSA station were kept fixed on their ITRF96 coordinates. **b)** Coordinate and tropospheric parameters were estimated simultaneously for the IGS station ONSA. **c)** Mean shift in the height component of the ONSA coordinate as a function of relative tropospheric constraints and estimation interval. Note the break in the horizontal axis.

5.4 Comparison of WVR and GPS retrieved water vapor

5.4.1 The Spanish campaign

This experiment was carried out in the northwestern part of the Madrid area between the 2nd and 15th of December 1996 [Elosegui et al., 1998; Ruffini et al., 1998; Kruse et al., 1999]. A local network of five Trimble SSE 4000 receivers was operated during two weeks (see Figure 5.4). Two of the GPS campaign stations were placed next (less than 10 meters) to the IGS Stations Madrid (MADR) and Villafranca (VILL) at the INTA-NASA Deep Space Network Complex in Robledo and at the European Space Agency (ESA) site at Villafranca, respectively. Four WVRs were operated at three of the GPS sites. The BKG-WVR-Yellow was operated during the second week of the campaign. One of the major goals was to perform a WVR comparison between the ETH WVRs and the JPL WVR located next to the IGS station MADR. Unfortunately only 60 pointings from the JPL instrument during these 14 days were available. The weather conditions were often rainy and because the WVRs do not yield reasonable results under such conditions, the rain fall caused gaps of several days in the WVR time series. The inversion of water vapor contents from radiometric intensity measurements is described in chapter 4.

Difference/Station	Escorial [mm]	Robledo [mm]	Villafranca [mm]
Δ_{IPWV}	+0.24	0.02	+1.32
σ	1.11	1.78	1.61

Table 5.1: Mean and standard deviation of the GPS - WVR differences at Escorial, Robledo and Villafranca. The results from the station Robledo were calculated with estimates from two WVRs (see Figure 5.7).

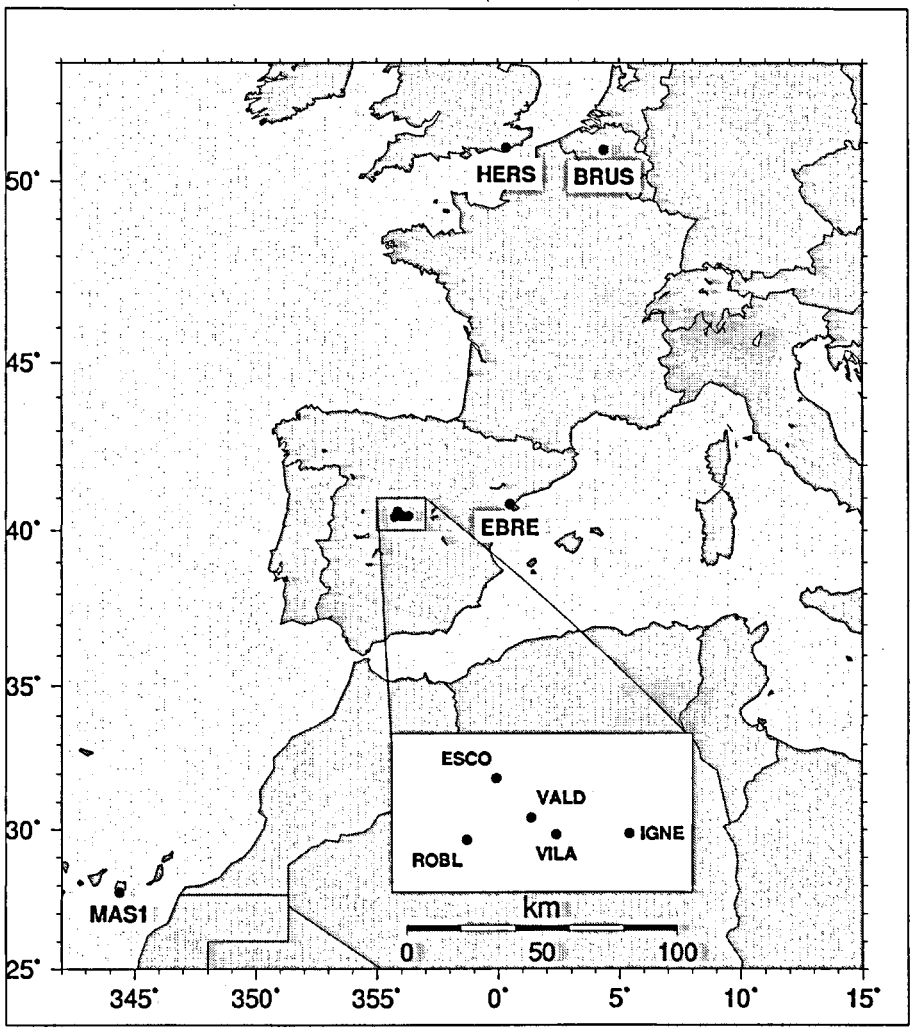

Figure 5.4: Campaign and IGS-core stations (BRUS, HERS, EBRE and MAS1) used in the processing. The spacing between the campaign stations is 8 to 50km

5.4.1.1 Results and Comparison

The GPS network solution included the remote IGS stations Herstmonceux (HERS), Ebre (EBRE), Maspalomas (MAS1) and Brussels (BRUS) to determine campaign station coordinates and to achieve absolute GPS IPWV estimates. Tropospheric parameters were estimated on a half-hour basis with relative constraints of 2mm. The WVR data were averaged over half-hour intervals to match the GPS estimation intervals. An additional bias was observed for the BKG-Yellow WVR as a consequence of an instrumental crash due to a heavy thunderstorm. In the processing, this bias was corrected for using the results of the ETH-Red WVR. Barometric pressure measurements from the GPS/WVR site were used, in order to split the

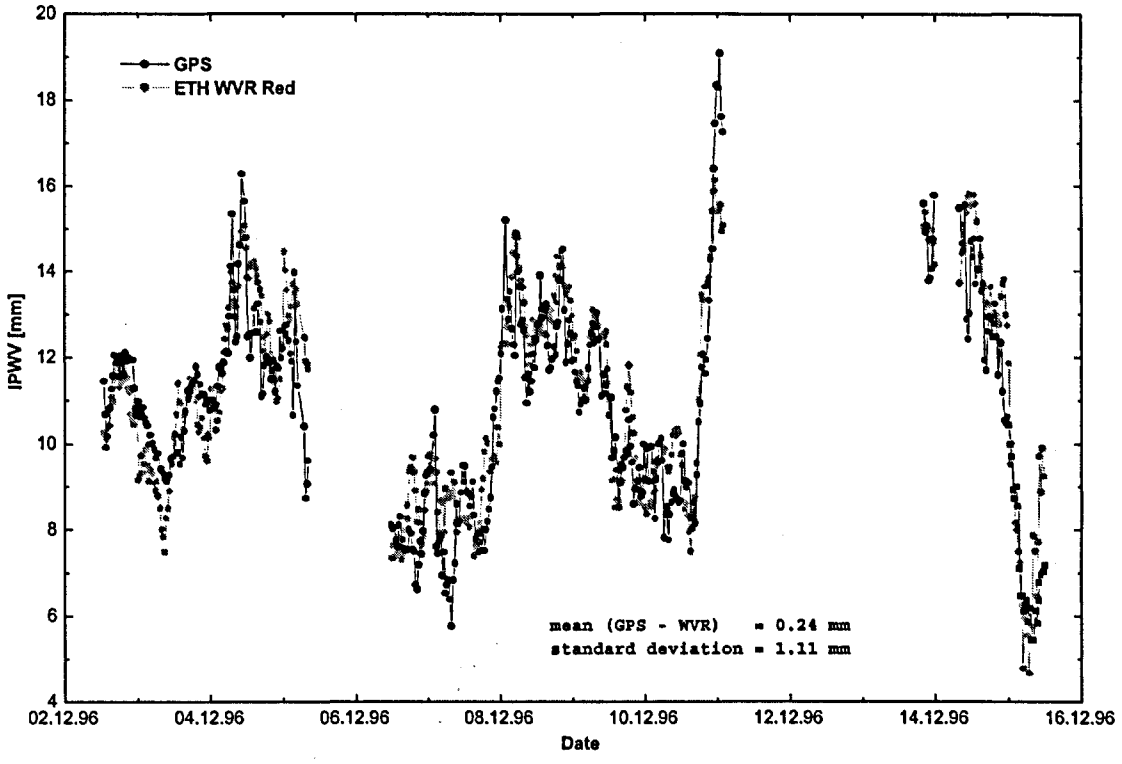

Figure 5.5: GPS and WVR estimates of IPWV at the Escorial site. Large signal variations during the campaign covering a wide range of IPWV were observed. Rain fall caused interruptions in the WVR time series for several days.

total path delay derived from GPS into a hydrostatic and a wet component. The latter was then compared to the results obtained with the WVR. The results of the GPS/WVR comparison show a good agreement. The best agreement is, however, achieved at the Escorial site with a standard deviation of 1.1 mm IPWV (table 5.1). At the Villafranca and Robledo sites rain was more frequent than at the Escorial site which may explain the higher standard deviations at these two sites. The results for each GPS/WVR site are plotted in Figure 5.5, 5.6 and 5.7 and the statistics of the comparisons are listed in Table 5.1.

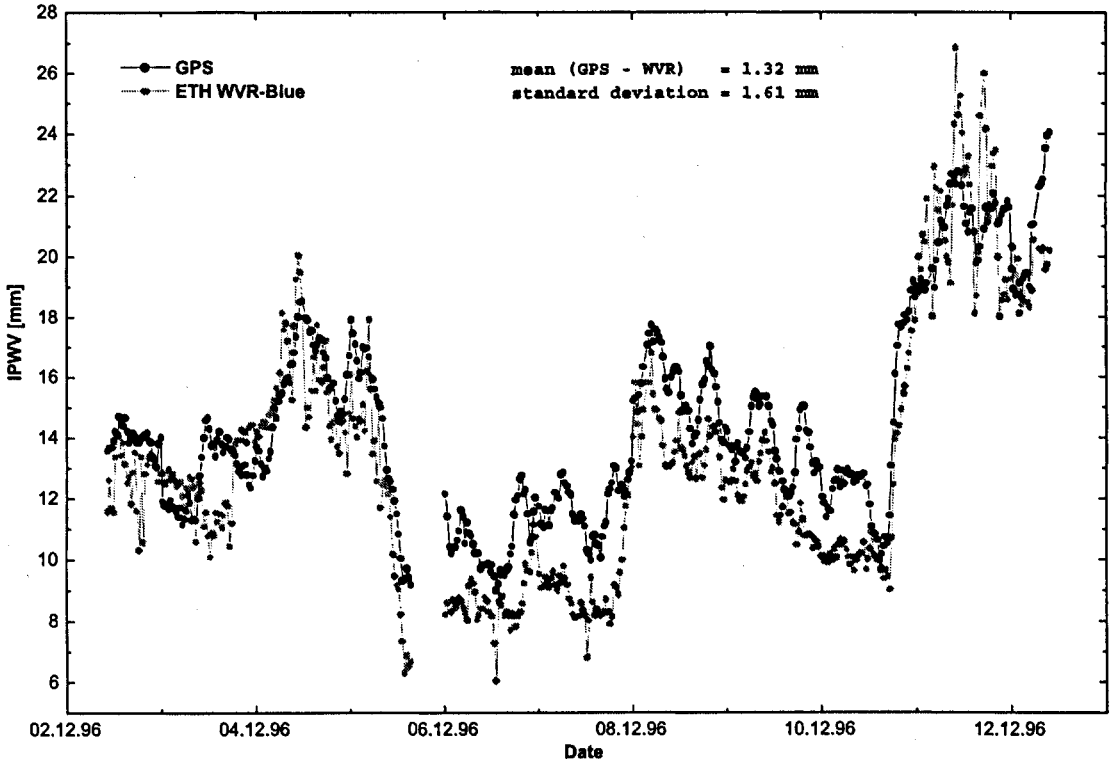

Figure 5.6: GPS and WVR estimates of IPWV at the European Space Agency (ESA) at Villafranca. The large increase in IPWV at the end of the period shown was followed by a period with rain for almost five days. The large scatter of the WVR results indicate an increase in cloud liquid water. The gap in the WVR time series on December 6. was caused by rain fall.

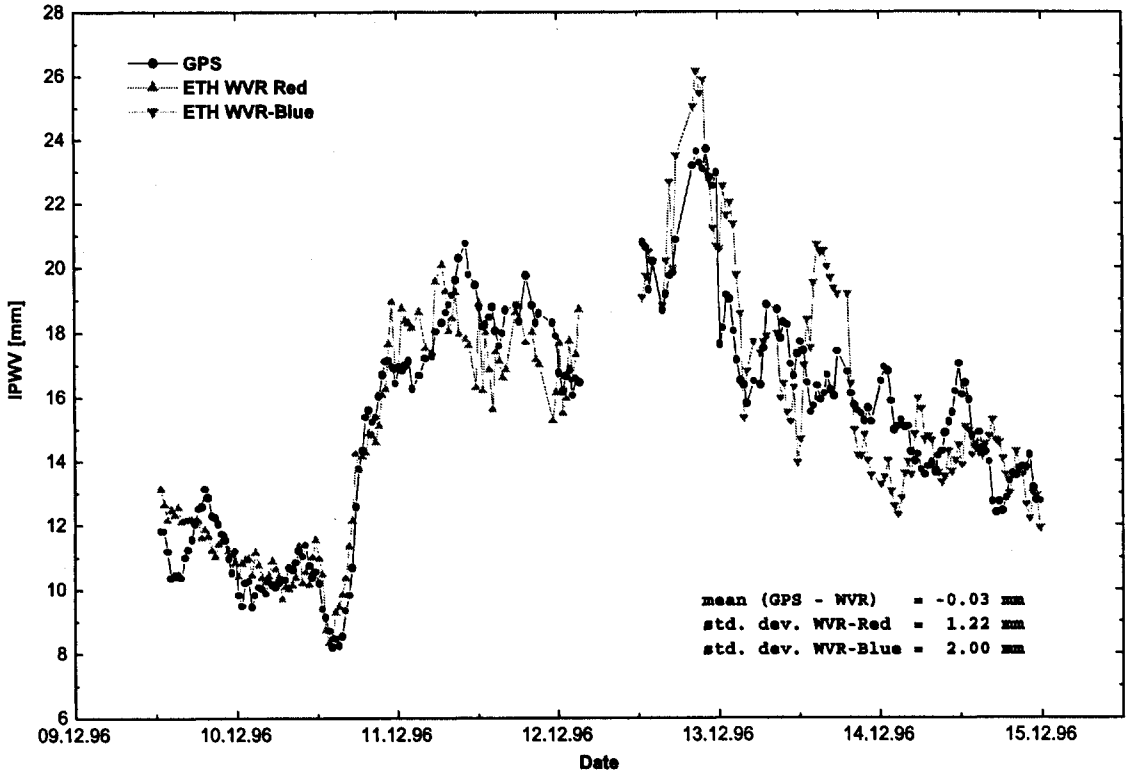

Figure 5.7: GPS and WVR estimates of IPWV at the INTA-NASA Deep Space Network Complex site in Robledo. Both ETH WVRs (Red and Blue) were operated at this site. The comparison with the JPL WVR at this site could not be performed due to rain and instrumental errors.

5.4.2 GPS-WVR comparison at Onsala

The second field campaign within the WAVEFRONT project was carried out at the Onsala Space Observatory. The dual channel WVR ASTRID is operating at this site for more than ten years. The goal of the campaign was to compare measurements of water vapor from two different types of WVRs. The Onsala WVR measures the sky brightness temperature at 21.0 and 31.4 GHz where as the ETH WVRs measure at 23.8 and 31.5 GHz.

The campaign started on August 11^{th} 1997 and lasted 11 days. The results of the comparisons are listed in Table 5.2. Details on the WVR/WVR comparisons can be found in Chapter 4.

Difference/WVR	ETH-RED [mm]	ETH-BLUE [mm]	ASTRID [mm]
Δ_{IPWV} GPS-WVR	-1.42	-1.34	+0.52
standard dev.	1.79	1.82	1.80
Δ_{IPWV} ASTRID-WVR	-1.84	-1.49	0
standard dev.	0.68	0.97	0
Δ_{IPWV} Radio sounding-WVR	-0.59	-0.46	1.35
standard dev.	2.19	2.12	2.10

Table 5.2: Statistics on the GPS, WVR and Radio soundings comparisons. The standard deviation of the three GPS - WVR and radiosonde - WVR differences are about the same for all three WVRs.

5.4.2.1 Results

The GPS Network solution included four IGS stations, Onsala (ONSA), Wettzell (WTZR), Kootwijk (KOSG) and Zimmerwald (ZIMM). Tropospheric parameters were estimated within 15-minute intervals with relative constraints of 1 mm. The WVR data were averaged over equal intervals to match the GPS estimates. Barometric pressure and temperature measurements from the ONSA site were used to calculate IPWV from total zenith delay estimates. The results listed in Table 5.2 show a standard deviation of the WVR - GPS difference of about 1.8 mm IPWV for all three WVRs. This relatively high scatter is due to positive and negative offsets at the maxima and minima of the GPS time series (Figure 5.8). The standard deviation of the radiosonde - WVR differences are about 2.2 mm IPWV for all three instruments. The higher scatter of the radiosonde - WVR differences compared to the GPS - WVR differences is due to three radiosonde results showing higher IPWVs than the WVRs. These deviations can be explained by the distance of 37 km between WVR and radiosonde launch site.

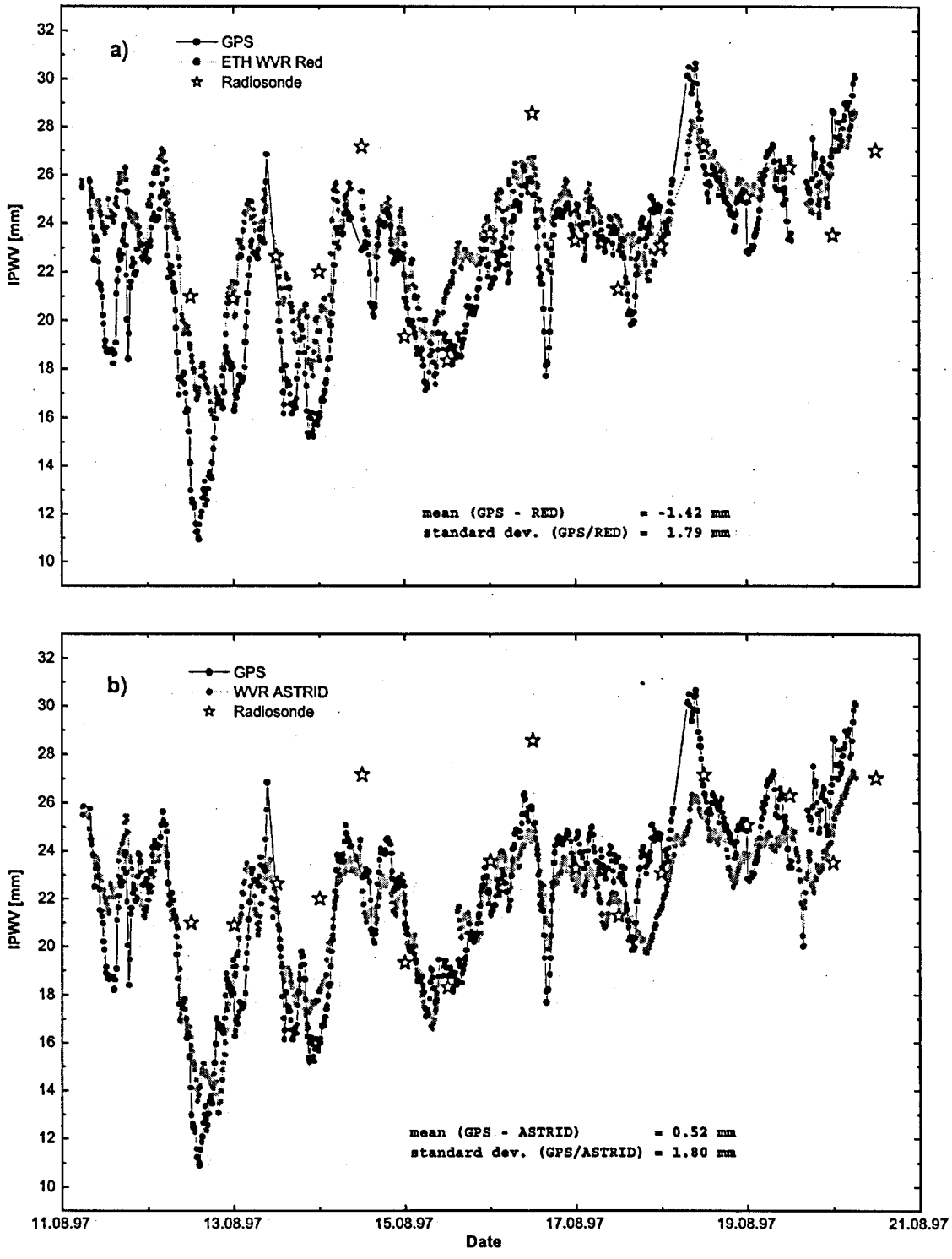

Figure 5.8: Comparison of IPWV from GPS, radiosonde and two WVRs at the Onsala Space Observatory. Figure a and b display both the GPS and radiosonde results compared with the ETH-Red WVR (a) and ASTRID (b), respectively. The radiosonde were launched at Landvetter airport (37km from the WVR site). The continuous WVR time series show large temporal variations that are not seen by the radiosondes due to the low sampling rate.

5.4.3 GPS-WVR comparison at Wettzell

For a period of nine days from June 22nd to July 1st 1998, four WVR instruments were co-located at the IGS station Wettzell.

The GPS Network solution included the stations WTZR, ONSA, KOSG, ZIMM and ETHZ. Coordinates were fixed to the ITRF94 (epoch 1998,176). Tropospheric parameters were estimated within 15-minute intervals with relative constraints of 2mm.The WVR data were averaged over equal intervals to match the GPS estimation intervals. Barometric pressure and temperature measurements from the Wettzell site were used to calculate IPWV. The effect of using offset-calibrated WVRs can be seen in table 5.3.

The biases using un-calibrated instruments (line one) are reduced for all instruments to agree with GPS within 1mm IPWV (line two). However, two of the Wettzell WVRs exhibit rather large standard deviations. In case of BKG-Green this was due to instable calibration loads of the instrument. The higher standard deviation of the BKG-White instrument was due to a shift in IPWV of about 1.75 mm. (see Section 4.3.2, Figure 4.8).

Difference/WVR	Red [mm]	Green [mm]	White [mm]	Yellow [mm]
Δ_{IPWV} GPS-WVR	-2.91	+1.44	-2.67	-5.61
Δ_{IPWV} *calibrated*	-1.07	-0.83	-0.90	-0.90
σ	1.18	2.64	2.94	1.40

Table 5.3: GPS/WVR comparison of all four WVRs. The mean of GPS - WVR differences are listed in row one. In row two the results from the four instruments are offset-calibrated with respect to the ASTRID radiometer by using the ETH-Red instrument as a calibration link between ASTRID and the BKG instruments. Applying the relative offsets between each WVR and ASTRID reduces the bias between the GPS and WVR estimates in all four cases considerably.

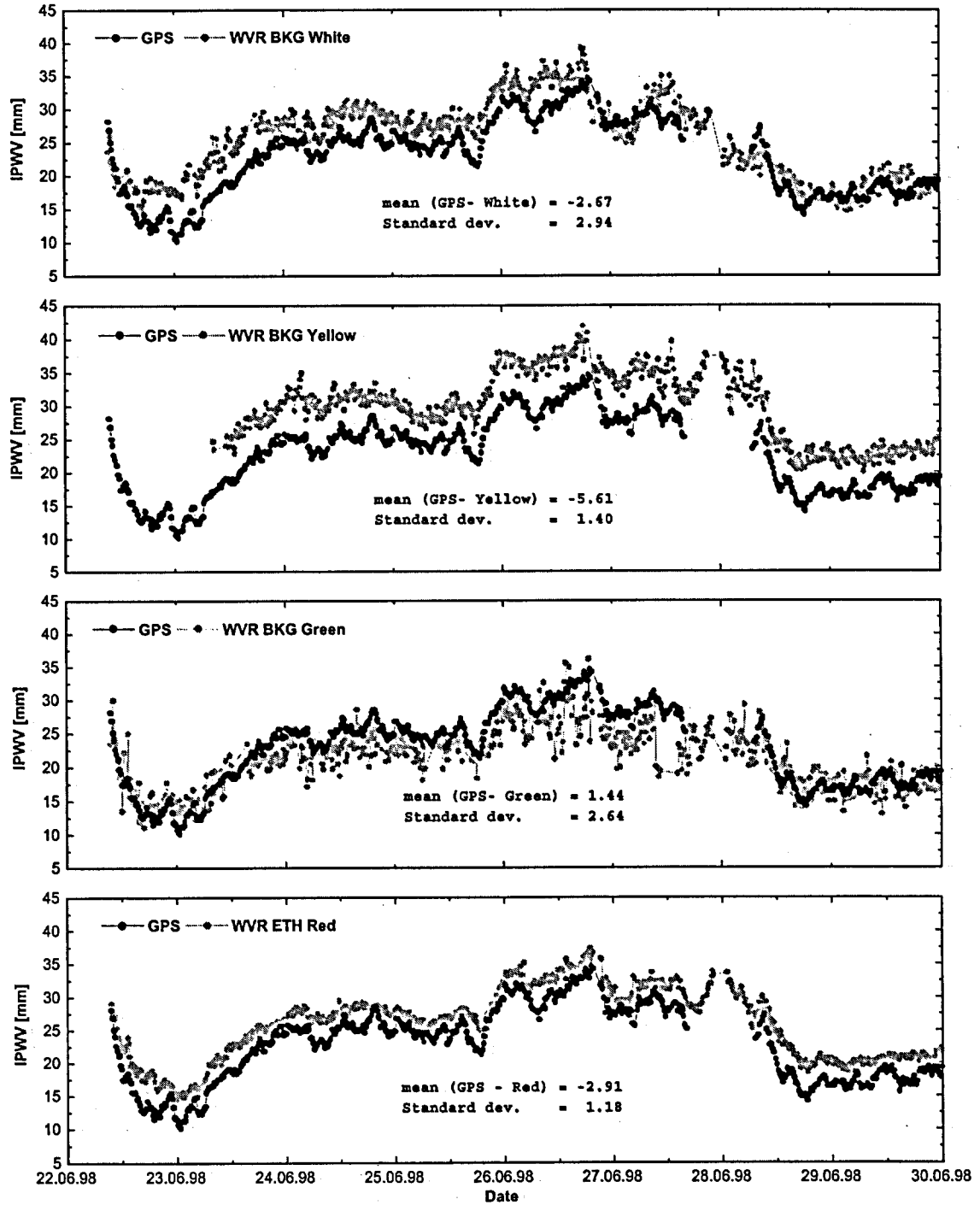

Figure 5.9: IPWV estimates from four WVRs and GPS at the IGS station Wettzell. Each point represent a mean of IPWV within an interval of 15-minutes. Seventeen hours of GPS recordings around June 28^{th} were not available for the processing and caused therefore a gap in the time serie. The individual offsets of the four WVRs with respect to the GPS results were considerably reduced after calibration (see also Table 5.3).

5.4.4 Long-term time series of water vapor acquired at ETH

Since October 1997 a continuous GPS receiver and one of the ETH WVRs has been operated at the Institute of Geodesy and Photogrammetry at the ETH Zurich. The GPS station (ETHZ) is part of the Automatic GPS Network of Switzerland (AGNES). Sixteen month of GPS data and 12 month of WVR data were processed for this comparison. In addition, meteorological modeling of IPWV was performed with the software package COMEDIE (see chapter 3) and the Saastamoinen formula.

5.4.4.1 GPS Processing

The GPS data from the ETHZ station were processed in a network including the IGS core stations Onsala (ONSA), Kootwijk (KOSG), Wettzell (WTZR) and Zimmerwald (ZIMM). Coordinates of the ETHZ station were estimated on a daily basis. The IGS sites were held fixed on extrapolated ITRF97 reference coordinates. Final precise IGS orbits were used and the daily coordinate solutions were estimated with 12 tropospheric parameters per site and day. The position of the antenna was moved about one meter on the 27th of march 1998. The number of daily solutions used were 171 and 275 for the old position and new position, respectively. Table 5.4 shows the coordinate solutions at the reference epoch 1.1.1997 for the old and new antenna position. The calculated velocities for the two antenna positions are listed in Table 5.5 and it can be seen that the two positions differ by 1.9 mm/year in the North - South direction, 7.2 mm/year in the East - West direction and 6.1 mm/year in the vertical direction. The relative small number of daily solutions for the old antenna position is expected to be too low for reliable velocity estimates [Calais, 1999]. However, the velocity of the new antenna position agrees within 1mm/year with the results obtained by Calais [1999] for the IGS station Zimmerwald.

In a second run all station coordinates were fixed to daily solutions within the ITRF97 reference frame and tropospheric parameters were estimated within 15 min intervals with a relative constraint of 3 mm between consecutive estimates. A total of 28'998 estimates were compared with 25'503 15 minute WVR estimates which gave a total of 19'741 comparisons. Nine month of 15 minute modeling estimates were compared with the GPS and WVR estimates. For completeness, the Saastamoinen model was evaluated. The results of the comparisons are listed in Table 5.6 and shown in Figure 5.12 and 5.14a, b and c.

5.4.4.2 Results and Comparisons

In Table 5.6 the results of the water vapor estimates from GPS, WVR, COMEDIE and Saastamoinen at the station ETHZ are shown. The time series for the four data set covers 12, 12, 9, and 9 month of almost continuous data. All four time series

	ETHZ(oldpoint)		*ETHZ(newpoint)*	
	[m]	σ[mm]	[m]	σ[mm]
X:	4277259.9706	3.6	4277260.2315	3.9
Y:	640044.3448	1.4	640044.5760	2.1
Z:	4672948.3282	4.0	4672949.2597	4.1
	deg./meter	σ	deg./meter	σ
Lat:	47.407065341	1.6E-8	47.407069076	2.2E-8
Long:	8.510528571	2.0E-8	8.510531089	2.3E-8
Height:	593.9531	5.1mm	594.8366	5.2mm

Table 5.4: Coordinate solutions for the ETHZ station in the ITRF97 reference at epoch 1.1 1997. The position of the antenna was moved about one meter on the 27th of march 1998. 171 and 275 daily solutions were used to calculated the old and new positions, respectively.

	ETHZ(oldpoint)		*ETHZ(newpoint)*	
	slope [mm/year]	σ	slope [mm/year]	σ
v_x	-10.1	$\pm$ 2.2	-16.7	$\pm$ 1.2
v_y	10.4	$\pm$ 0.9	16.6	$\pm$ 0.6
v_z	13.1	$\pm$ 2.4	9.8	$\pm$ 1.3
N	15.1	$\pm$ 1.1	17.0	$\pm$ 0.7
E	11.8	$\pm$ 0.9	19.2	$\pm$ 0.5
H	4.0	$\pm$ 3.0	-2.1	$\pm$ 1.6

Table 5.5: Geocentric and topocentric velocity solutions for the two antenna positions calculated within the ITRF97 reference frame. The disagreement between the two velocity estimates is on the order of 1 cm/year. The number of daily solutions for the old and new position are 171 and 275, respectively. The relative small number of daily solutions for the old antenna position is expected to be too low for reliable velocity estimates.

start on October 1^{st} 1997. WVR recordings from the last three month of 1998 were not available due to hardware failure of the instrument.

The GPS/WVR time series used for comparison (Figure 5.12a) cover a little more than one year of 15 minute estimates. A total of 19'741 GPS - WVR differences were calculated (Figure 5.12b). Typically a formal error of 1 mm for the GPS derived TZDs was achieved. Only GPS estimates with a formal error better than 5 mm were considered for the comparison. This reduced the number of GPS estimates by about 5%. The average standard deviation of the WVR IPWV estimates were 1.1 mm and an upper threshold of 1.6 mm was used to remove outliers. This reduced the amount of WVR estimates by about 5%. The standard deviation of the GPS -

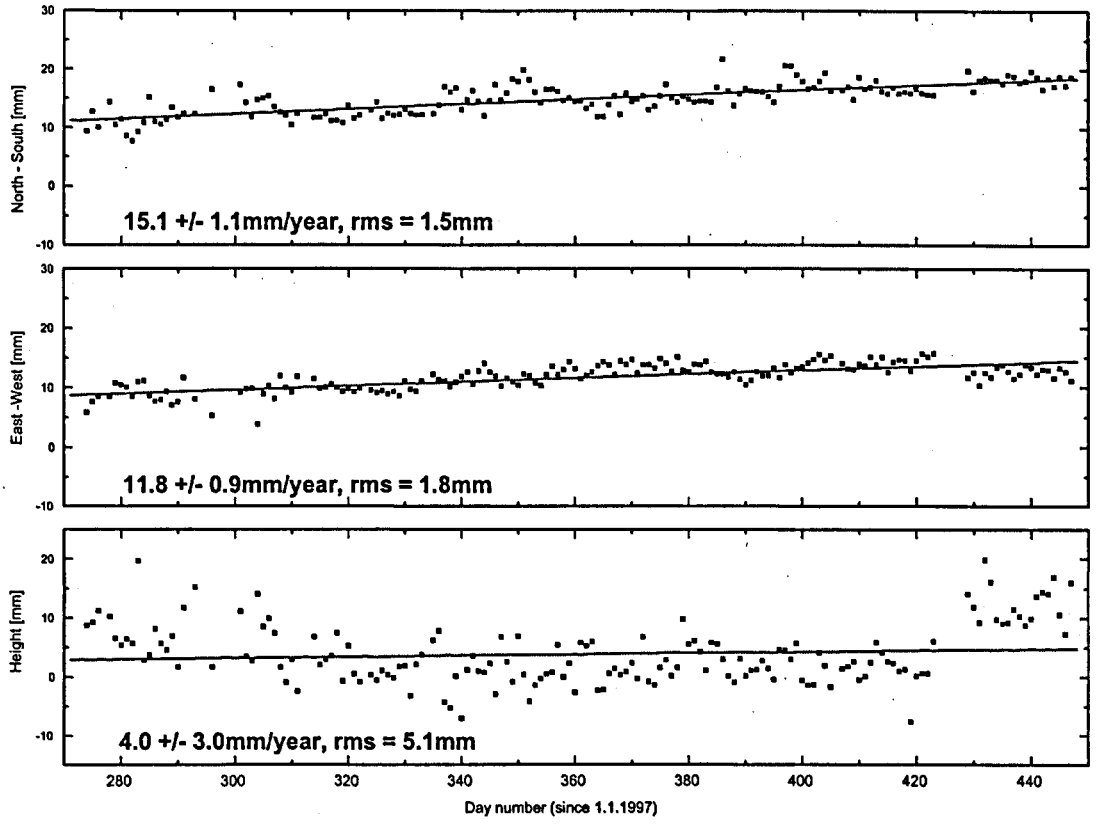

Figure 5.10: Daily coordinate solutions for the old antenna positions of the station ETHZ as a function of time since 1.1.1997 this date represents the reference epoch in the ITRF97 reference. The grey straight lines represent the linear best fit and their slope indicate the velocity of the point. Five days of GPS data are missing around day number 430 due to a computer hardware failure. The daily solutions for ETHZ were calculated by fixing the IGS station Onsala, Kootwijk, Wettzell and Zimmerwald on daily coordinates extrapolated from the ITRF97 reference.

WVR differences is 1.54 mm with a bias of 0.54 mm IPWV.

The ground meteo observations from the ANETZ network and radiosonde measurements from the station Payerne used to model tropospheric water vapor are identical to those described in chapter 3. Mean and standard deviation of the 20'520 GPS - Modeling differences (Figure 5.14a) are -2.23 and 2.88 mm IPWV.

The results obtained with the Saastamoinen formula were calculated with interpolated meteo parameters from the modeling since meteo recordings were not available at the station during this period. The mean and standard deviation of the 20'860 differences (Figure 5.14c) are 0.48 and 3.10 mm IPWV.

Figure 5.14a,b and c shows IPWV differences of a) GPS - Modeling, b) WVR -

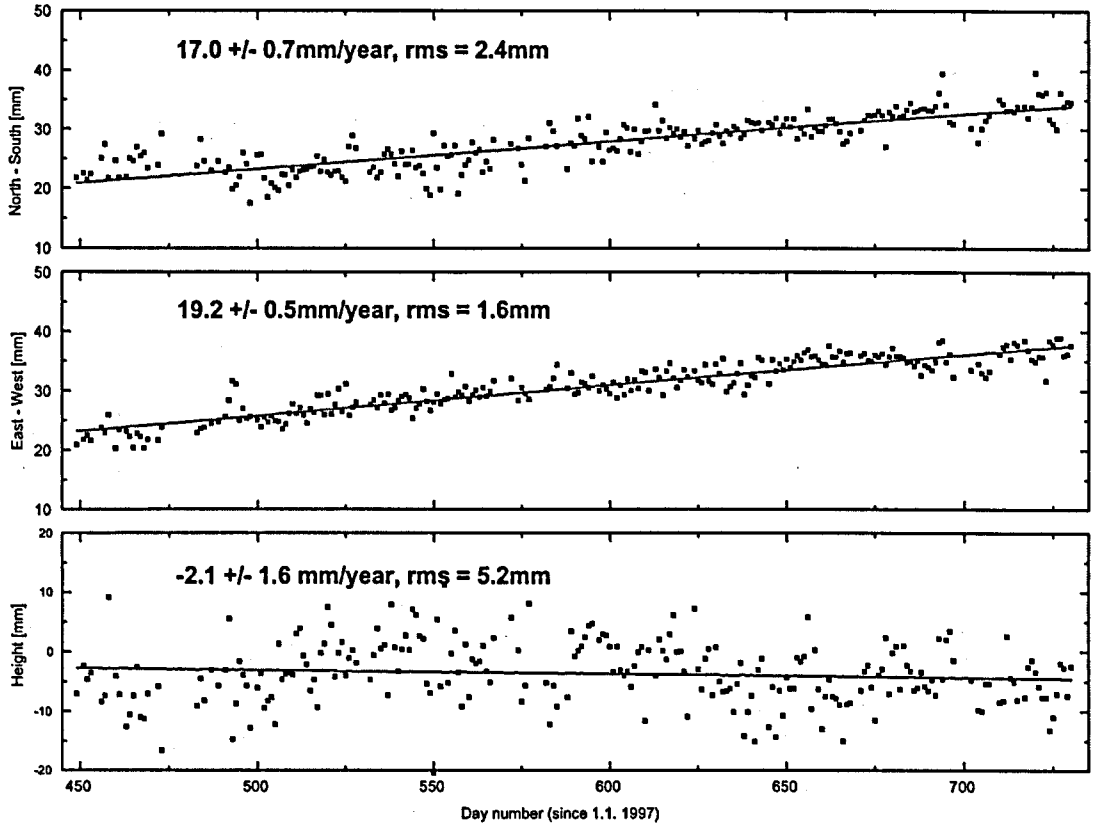

Figure 5.11: Daily coordinate solutions for the new antenna positions of the station ETHZ as a function of time since 1.1.1997, this date represents the reference epoch in the ITRF97 reference. The grey straight lines represent the linear best fit and their slope indicate the velocity of the point. The daily solutions for ETHZ were calculated by fixing the IGS stations Onsala, Kootwijk, Wettzell and Zimmerwald on daily coordinates extrapolated from the ITRF97 reference.

Modeling and c) GPS - Saastamoinen. The variation of the differences are small during the months November to April compared to the months October, May and June. This pattern is also visible in the GPS - WVR differences Figure 5.12b. The higher scatter of the differences during summer and autumn is correlated with the larger variability in IPWV during this period (Figure 5.12a). The differences a, b and c in Figure 5.14 show a large negative peak during a ten day period in May which is not visible in the GPS - WVR differences. A possible explanation for this feature could be a warm and humid boundary layer shifting the temperature and humidity profiles to higher values, which in turn causes an overestimation of IPWV from both modeling and Saastamoinen. The WVR - Modeling comparison show a better agreement on the absolute scale compared to the GPS - Modeling results.

difference	mean [mm]	σ[mm]	#
GPS-WVR	-0.54	1.54	19'741
GPS-Modeling	-2.23	2.88	20'520
GPS-Saastamoinen	0.48	3.10	20'860
WVR-Modeling	-1.60	2.74	17'529

Table 5.6: Mean and standard deviation of the four differences listed in the first colum. The period covered is one year for the GPS - WVR differences and nine month for the differences calculated from results obtained by modeling and the Saastamoinen formula. The number of differences used are shown in the last colum.

The better standard deviation of the WVR - Modeling differences is, however, small. This was also observed during the 21 day (December 1997) comparisons shown in chapter 3.

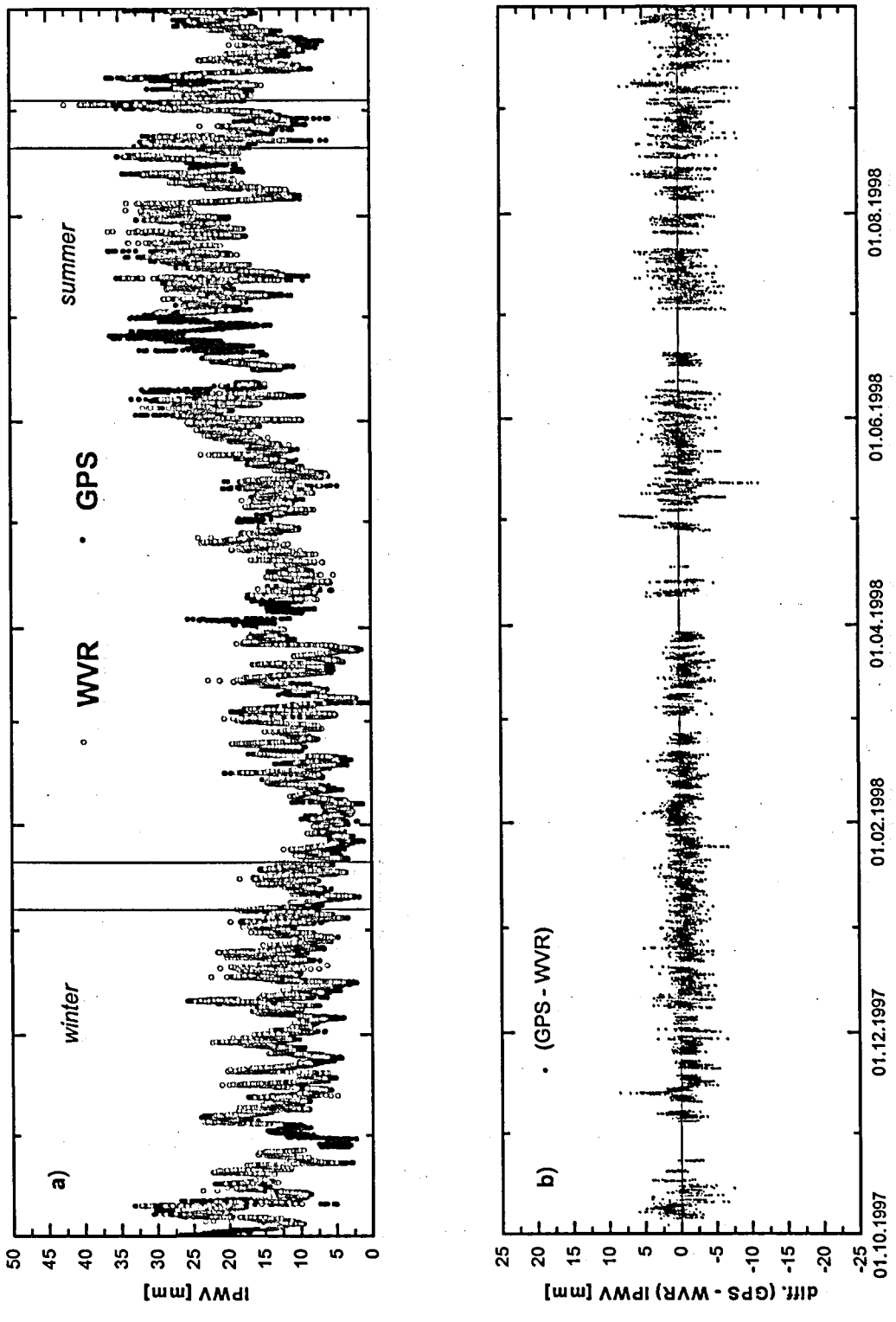

Figure 5.12: a) Twelve month of GPS- and WVR IPWV estimates at the ETHZ station. A total of 28'998 GPS and 24'157 WVR points are plotted. b) 19'741 GPS - WVR differences were calculated from the GPS and WVR estimates shown in a. The standard deviation of the differences is 1.54 mm with a bias of -0.54 mm IPWV.

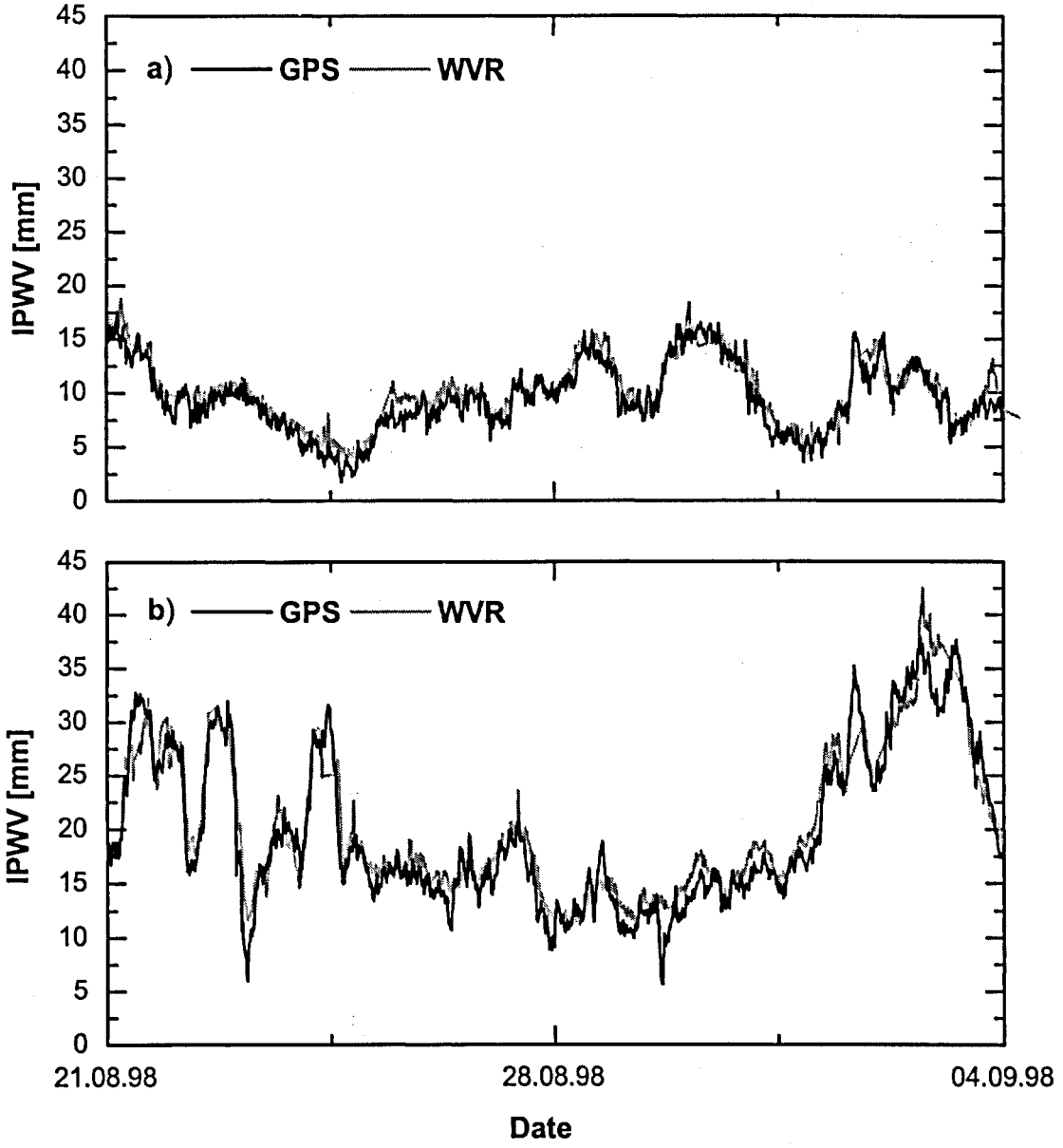

Figure 5.13: Two fourteen day periods of IPWV estimates from GPS and WVR at the station ETHZ. **a)** The IPWV estimates during January 1998 show a slowly varying water vapor content compared to the summer period **(b)** where large and rapid fluctuations of IPWV is seen.

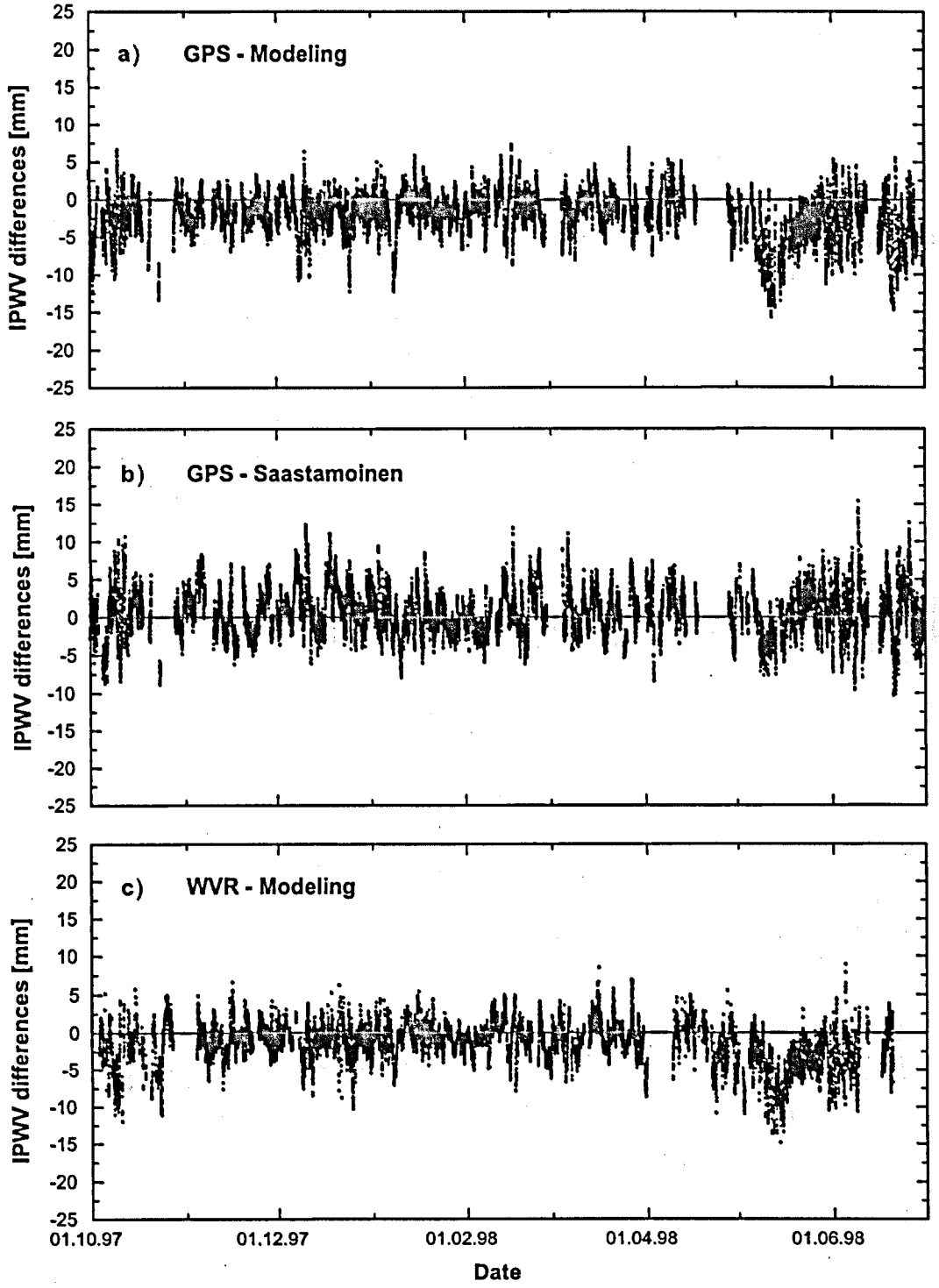

Figure 5.14: IPWV differences calculated for the period October 1997 to June 1998 at the station ETHZ. The number of differences are a) 20'520 (GPS - Modeling), c) 20'860 (GPS - Saastamoinen) and b) 17'529 (WVR - Modeling). Statistics on the differences are listed in Table 5.6. The large negative peak at the beginning of May is visible in all three difference plots.

5.5 Real-time GPS meteorology

5.5.1 Introduction

The research presented in this section was published by [Kruse et al., 1999].

Simulations of global and regional climate change using observations of IPWV were carried out by Yuan et al. [1993]. It has been shown [Kuo et al., 1996] that forecasts can be significantly improved by assimilating such data in numerical prediction models. Operational weather forecasters typically update their forecasts within a few hours. This means that GPS derived water vapor estimates have to be produced at the same rate. A crucial factor for GPS IPWV estimation is the accuracy of the orbit data. At present, precise orbits, available from IGS with a delay of 10 days, are not appropriate for near real-time applications. In this study we therefore investigate the feasibility of using predicted GPS orbits for accurate estimation of IPWV. The basis for the study is a data set of continuous GPS data, which was acquired during a 14-day field campaign in December 1996 near Madrid, Spain. The data were post-processed using both predicted and precise orbits to assess the impact of the orbit data on the GPS IPWV estimates. In addition different analysis strategies were tested and results from one of the campaign stations were compared with measurements of a co-located Water Vapor Radiometer (WVR).

5.5.2 Orbit Prediction at CODE

The IGS is producing combined rapid orbits with a delay of currently 22 hours. In addition to these (rapid) orbits the IGS also produces combined predicted orbits which are available for real-time usage. These predicted orbits, which are based on a 2-day extrapolation, are made available at 23:00 UTC. Note that these official IGS products are both based on a combination of the contributions of the individual IGS Analysis Centers. For more information about these and other IGS products we refer to the IGS annual reports [Kouba and Mireault, 1998].

The Center for Orbit Determination in Europe (CODE) contributes to both the IGS rapid and predicted orbits. At CODE the predictions are based on making a best fit, in the least squares sense, to the orbit positions of the last three CODE rapid orbit solutions. The resulting orbit is then extrapolated for 48 hours. The CODE rapid and predicted products are usually available before 12:00 UTC. Because CODE provides both 1-day and 2-day predictions the predicted orbits are more "recent" than the official IGS predictions. This reduction of the extrapolation time yields a significant improvement of the orbit quality, because the errors in the predicted orbits grow exponentially with time.

The major problem of predicted orbits is their integrity. Although the median of the predicted orbits, when compared to the final precise IGS orbits, is of the level of 20–50 cm the (weighted) RMS error is at the 50–100 cm level and is usually caused

by a single "bad" satellite (see Figure 5.15). The problem therefore is to predict the quality of the individual satellites' predicted orbits. At CODE this is done by fitting one single arc through the last seven rapid orbit solutions. The RMS of this fit is used to assign accuracy codes for the individual satellites. These accuracy codes may be applied by the user to downweight or remove bad satellites. The accuracy codes as provided by CODE have proven to be quite reliable [Kouba and Mireault, 1998]. However, there are still many days with bad satellite predictions. A sizable challenge for the near future will be to improve the integrity of the predicted orbit and to reduce the extrapolation time.

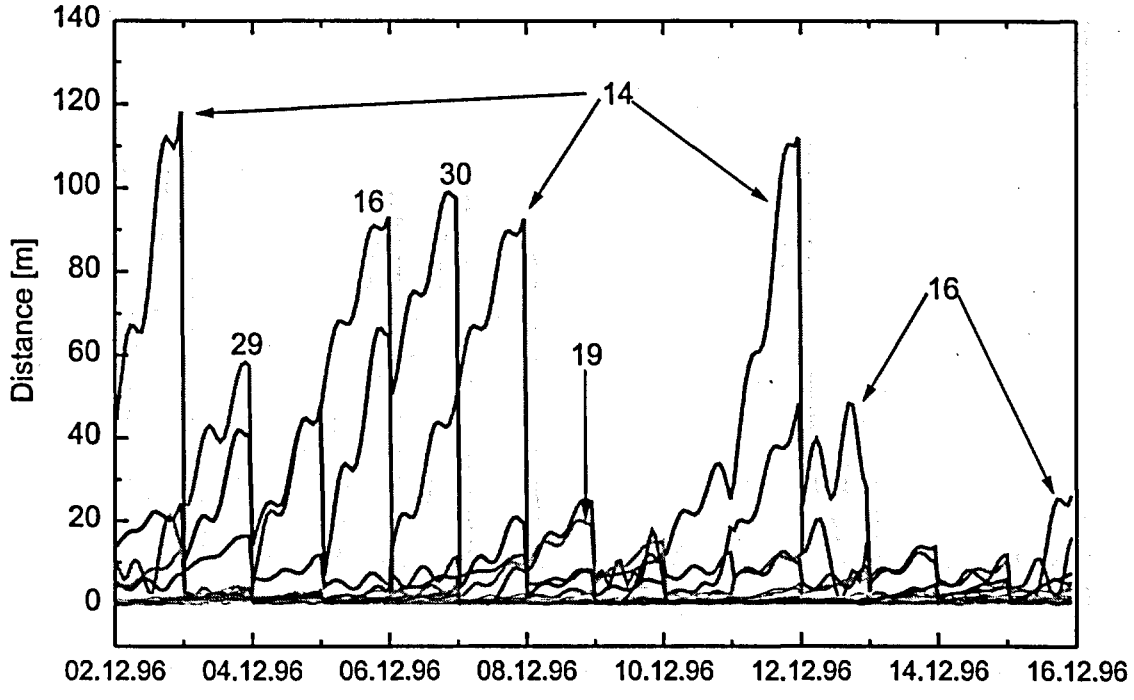

Figure 5.15: Distance in meters (at corresponding epochs) between final precise IGS orbits and two day predicted CODE orbits. The median distance over the fourteen day period is 0.8m (one day predictions reveal 0.3m). Satellites deviating from this median value have corresponding low accuracy values (e.g. sats. 14, 30, 16, and 29).

5.5.3 Results

In addition to the campaign stations remote IGS stations (HERS EBRE, MAS1 and BRUS) were introduced to determine campaign station coordinates (see below) and to achieve absolute GPS IPWV estimates. In a first step final precise orbits provided by the IGS were used in order to estimate the unknown coordinates of

the stations not belonging to the IGS network. The coordinates of the IGS stations were kept fixed to the International Terrestrial Reference Frame 1994 (ITRF94) extrapolated to December 1996. About 95% of the ambiguities were solved and fixed. Daily solutions of site coordinates were estimated over the 14-day period. The daily repeatability was 2 mm in the horizontal and 6 mm in the vertical component, respectively. A global solution based on the combination of the 14 daily solutions led to final coordinates that were kept fixed in the following investigations. Tropospheric parameters were estimated on a half hour basis without constraints. Although it is common to employ constraints on tropospheric estimates we decided not to do so because constraints would suppress or reduce orbital effects on the GPS estimates, which we intended to analyze. We chose a cut-off angle of 15deg to avoid higher noise and multi-path effects at lower elevations and the Hopfield mapping function to map the GPS estimates to the zenith.

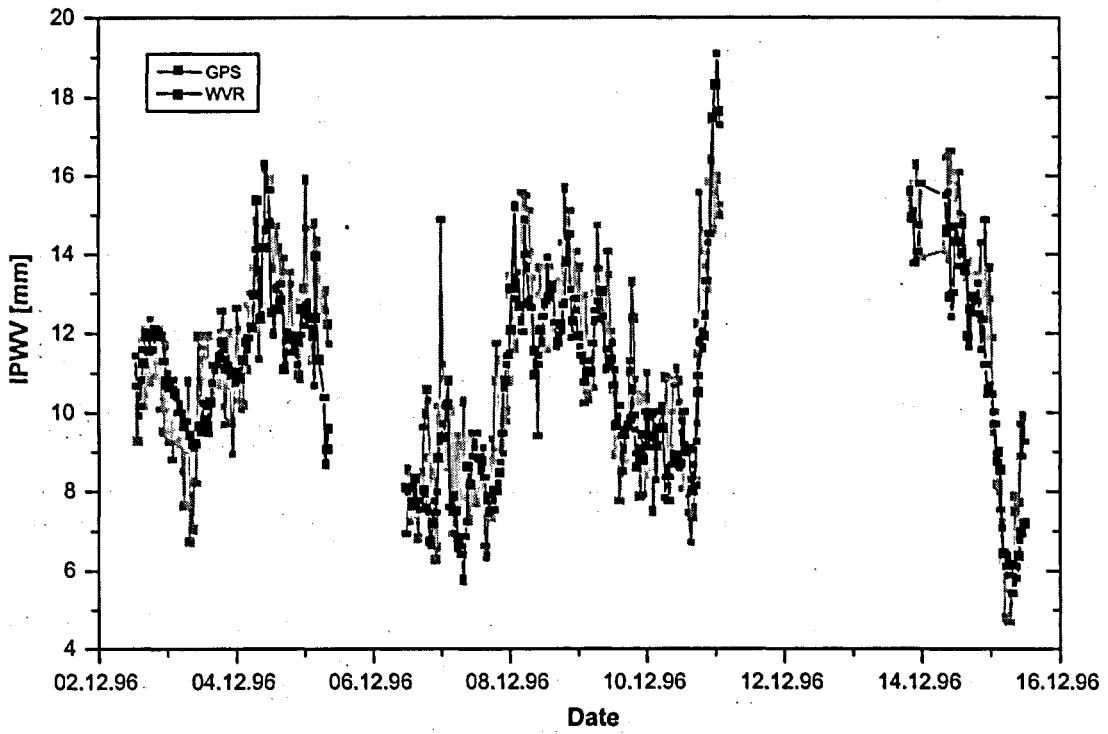

Figure 5.16: GPS and WVR estimates of IPWV. The independent WVR measurements were used as a reference for all GPS solutions presented in this study (black curve). The WVR curve is smoother than the unconstrained GPS estimates using final precise IGS orbits (gray curve). Large signal variations during the campaign covering a wide range of IPWV were observed. Rain fall caused interruptions in the WVR time series of several days.

The WVR data were averaged over half hour intervals to match the GPS estimates.

Barometric pressure measurements from the GPS/WVR site were used to divide the total path delay derived from GPS into a hydrostatic and a wet component. The latter was then compared with the results obtained with the WVR (see Figure 5.16). The comparison shows a bias of 0.4 mm and a standard deviation of 1.4 mm IPWV.

For a real-time determination of IPWV from GPS, however, final precise IGS orbits are not available. Therefore we repeated the computation of the tropospheric path delays using one and two day predicted ($P1$ and $P2$) orbits from CODE. For completeness broadcast orbits were considered as well.

As mentioned above the quality of the predicted satellite orbits is not the same for each individual satellite. Therefore orbit accuracy codes for all satellites are provided with the predictions (see section 5.5.2). Using this information three different solutions were calculated.

(a) orbit accuracy codes are ignored, all satellites are treated equally: $P[1,2]_{allsat}$

(b) accuracy codes in combination with a threshold value are used to eliminate those satellites with a bad orbit prediction: $P[1,2]_{selsat}$

(c) no satellite is eliminated, but the orbit accuracy codes are used to derive weights, which are introduced in the computation: $P[1,2]_{weights}$

The largest uncertainty in orbit prediction is the along-track component of the orbit. Therefore an additional solution (d) was also calculated allowing for adjustment of the argument of latitude.

(d) identical to version (c), but with one additional unknown orbital parameter per satellite (argument of latitude) with an a priori sigma of 0.006 arc-seconds : $P[1,2]_{weights+orb}$

The processing of all four versions (a-d) was performed using one day ($P1$) and two day ($P2$) predicted orbits. Tropospheric parameters were estimated as in the solution using final precise IGS orbits.

Table 5.7 summarizes the GPS-WVR comparisons using the different orbit types. The result of the first three versions (a to c) of $P1$ and $P2$ clearly demonstrate that the use of orbit accuracy information is mandatory. The two solutions $P[1,2]_{selsat}$ and $P[1,2]_{weights}$, make use of the quality information are more or less equivalent. A significant improvement is achieved when an additional orbit parameter (d) is estimated (see Figure 5.17) regardless which orbit ($P1$ or $P2$) is used. The comparison using broadcast orbits shows that this product is inadequate for GPS meteorology.

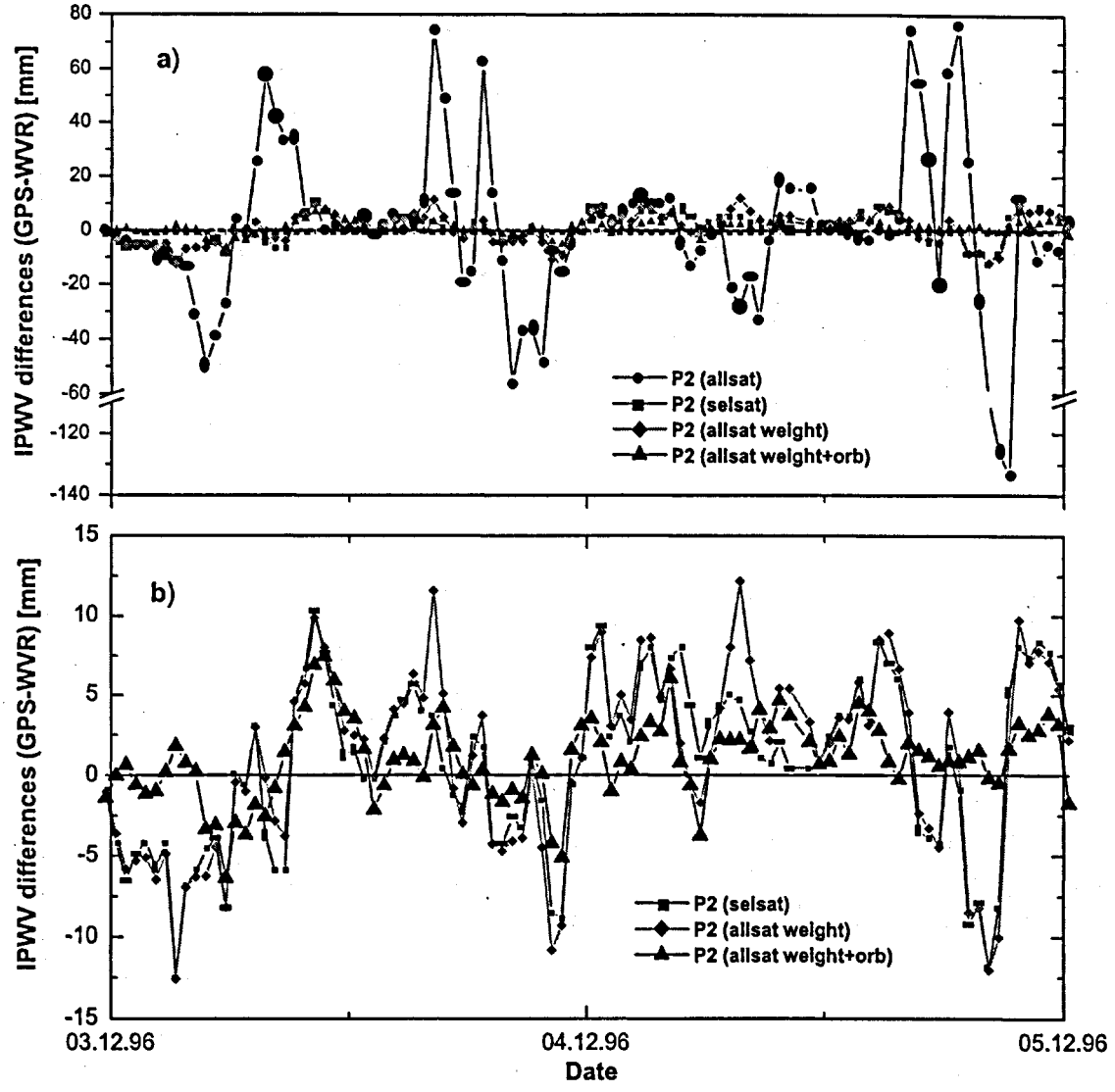

Figure 5.17: GPS-WVR differences over a two day period using two day predicted CODE orbits. **a)** The allsat solution (dots) ignoring orbit accuracy codes shows large deviations from the WVR reference. **b)** The three solutions (selsat, allsat weight, and allsat weight+orb) make use of the accuracy information provided with the orbits. The difference between selsat (diamond) and weight (square) is exclusion of satellites with accuracy codes lower than a threshold value and weighting according to the accuracy codes. The weight+orb solution (up-triangles) is a solution applying weights and estimating one along-track parameter per satellite.

Orbit	bias [mm]	Stddev. [mm]
Precise IGS	0.4	1.4
(a) $P1_{allsat}$	0.3	5.2
(b) $P1_{selsat}$	0.3	2.4
(c) $P1_{weights}$	0.4	2.4
(d) $P1_{weights+orb}$	0.3	2.0
(a) $P2_{allsat}$	0.5	21.1
(b) $P2_{selsat}$	0.7	5.0
(c) $P2_{weights}$	0.9	5.2
(d) $P2_{weights+orb}$	0.6	2.9
Broadcast	6.5	29.3

Table 5.7: Comparison of GPS-WVR solutions using different types of orbit information. The calculated biases and standard deviations are based on the results from 8.75 days.

5.5.4 Conclusion

We have investigated the impact of final precise IGS, 24 and 48 hour predicted CODE, and broadcast orbits on tropospheric GPS estimates. Four different GPS processing strategies for real-time estimations were evaluated and compared with data from a co-located WVR. The GPS-WVR comparison using final precise IGS orbits showed a good agreement which is comparable with recent results [Rocken et al., 1997; Dodson and Baker, 1998a,b].

For real-time applications the results will be degraded due to orbit accuracy, but we conclude that the predicted orbits as provided by CODE give significantly better results than broadcast orbits.

The comparison of the four processing strategies using one and two day orbit predictions shows that the incorporation of orbit accuracy information in the estimation procedure is mandatory for meteorological applications. The errors of predicted orbits are mainly in the along-track direction. The estimation of one single orbit parameter per satellite, to account for these along-track errors, improves the real-time GPS estimates significantly. The impact of this strategy is more pronounced for the two day than for the one day predicted orbits.

In our study, the best estimation strategy using the $P1$ orbits yields a standard deviation from the WVR curve that is about 1.4 times higher than the solution using final precise IGS orbits. For real-time GPS applications, however, one has to rely on a combination of one and two day predictions to achieve optimum results, since the release of the $P1$ product is delayed by about 12 hours. The currently obtainable precision will be 2-3 mm in real-time, less than a factor of 2 worse than the results achieved with final precise IGS orbits. At present GPS data from about

30 global stations are available as one hour observation files. This should bring us near to the 2 mm level or even below if we do orbit predictions more frequently (2 times per day, e.g. only 12 hour extrapolation).

6 The Hawaiian campaign

6.1 Introduction

A joint field campaign on Hawaii was initiated in order to investigate the feasibility of GPS tomography. For such an experiment a dense receiver network is required. Furthermore, large differences in station altitudes and strong fluctuations of humidity are desirable. A very dense CGPS network, almost perfectly meeting these requirements, is the Mt.Kilauea network on the Big Island of Hawaii. It is operated by the Hawaiian Volcano Observatory (HVO) of the U.S. Geological Survey, the School of Ocean, Earth, Science and Technology at the University of Hawaii (SOEST), and the University of Stanford.

6.1.1 Experiment description

One of the major goals was the comparison of tomographic GPS meteorology with several complementary techniques. Therefore the WAVEFRONT project group installed two ETH WVRs and a newly developed Solar Atmospheric MOnitoring Spectrometer (SAMOS) [Sierk, 2000]. In addition 18 radiosondes were launched in order to measure vertical meteorological profiles in several places of the Kilauea National Park. Measurements were performed during two weeks until February 28th, 1999. For the duration of the field experiment the core HVO/SOEST-network was reinforced by five additional receivers provided by the Onsala Space Observatory.

6.1.2 The CGPS network

The CGPS network at Mt. Kilauea consists of 16 stations distributed in an area of approximately 15x20 km within the Volcano National Park. Six of these stations are operated by SOEST, 12 sites are operated by HVO. The data of the receivers are automatically downloaded on a regular basis. The receivers operated within the CGPS network are of the type TRIMBLE 4000 (SSE and SSI) and ASHTECH Z-XII3 with the L1/L2 geodetic and Dorne Margolin choke ring antenna type, respectively. The additional receivers operated during the campaign were of the type Turbo Rogue with Dorne Margolin choke ring antennas. The network is used to

determine tectonic motions caused by volcanic activity in the area. The extraordinary close spacing of the GPS antennas, provides excellent conditions for GPS tomography.

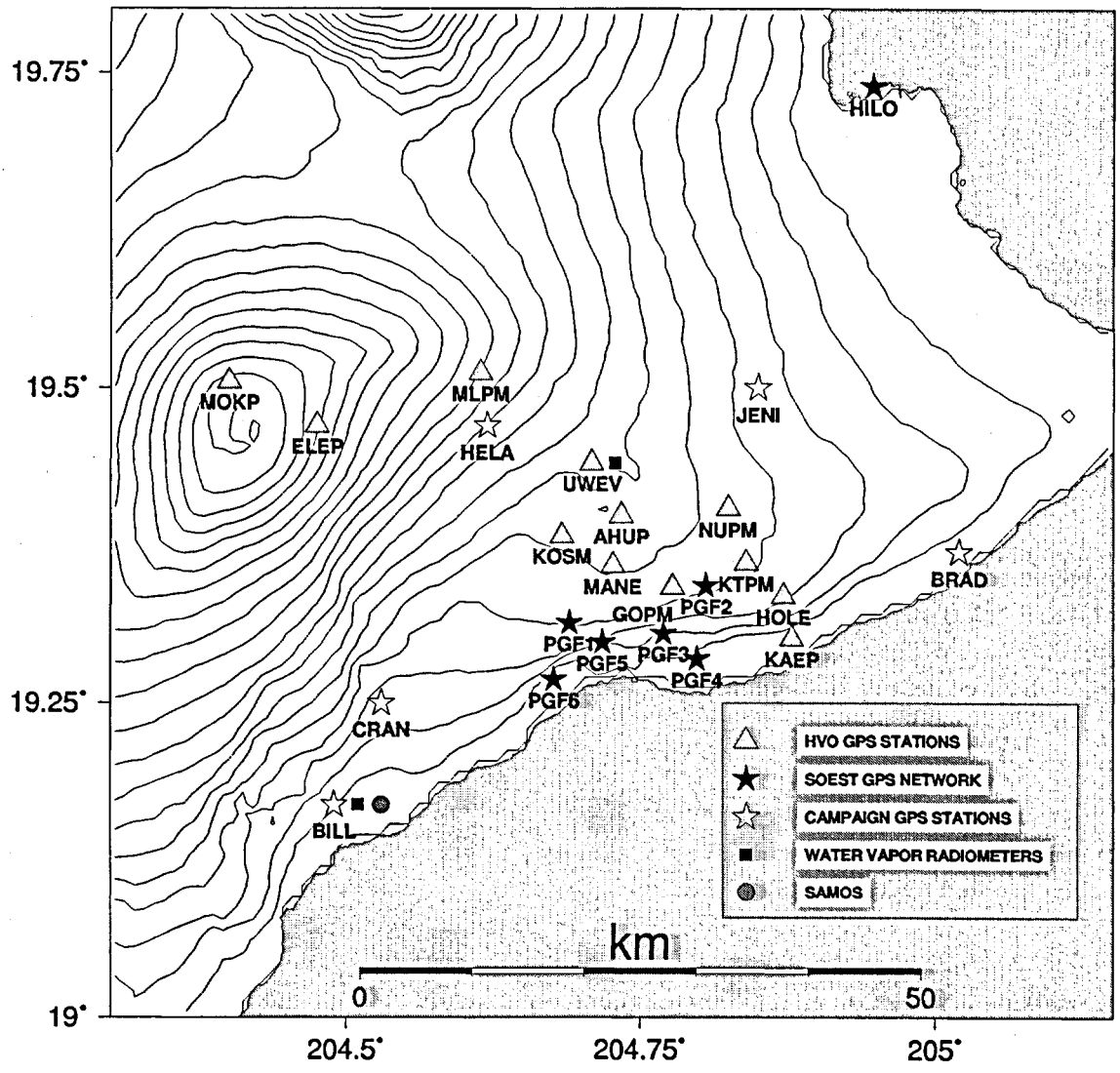

Figure 6.1: Mount Kilauea network on the Big Island of Hawaii. GPS WVR and SSM stations operated during the campaign. At the station BILL the three instruments GPS, WVR, SSM were operated simultaneously and seven radiosondes were launched from this site. The permanent CGPS network (*grey triangles and black stars*) consists of 6 SOEST and 12 HVO stations (see legend). The height difference from the lowest to the highest GPS station (PGF4 - MOKP) is about 4100 meters. At Hilo airport radiosondes are launched every twelve hours. The climate of the network region ranges from tropical in the east to arid in the west.

6.2 Data analysis

6.2.1 GPS analysis

The five IGS stations Mauna Kea (MKEA), Kokee Park (KOKB), Whitehorse (WHIT), Tsukuba (TSKB) and Kwajalein Atoll (KWJ1) (Figure 6.3) were introduced as fixed stations in the processing to achieve the best possible coordinate solution as well as absolute estimates of IPWV. Figure 6.2 displays a schematic view of the baseline configuration used. The Pacific GPS Facility (PGF) stations (Figure 6.1) were used as a base network to which the rest of the GPS stations was coupled. The GPS data from these stations were of the most complete during the campaign period, and relatively few cycle slips were detected when ambiguities were solved on baselines with these receivers only. The number of ambiguities to be solved for strongly depended on the receiver type combination. Up to 200 ambiguities were detected on baselines with Turbo-Rogue receivers compared to 50 on baselines with an ASHTECH-ASHTECH receiver combinations. This high number of ambiguities from the Turbo Rogue receivers was also observed within the IGS network [Schaer, 1999]. Wide-lane ambiguities were slowed with the Melbourne-Wübbenea linear combination on baselines ranging from 500 - 4500 km and the L_5 linear combination on short baselines. All narrow-lane ambiguities were solved with the L_3 (ionosphere free) linear combination. The percentage of solved ambiguities on short baselines was in the range of 70 - 98% depending on the receiver combination.

In a first step daily coordinates of the PGF stations were estimated. Table 6.1 shows the RMS of daily coordinate solutions of the PGF stations and the five IGS stations mentioned above. The station coordinates were estimated with the five IGS stations held fixed to the ITRF96 reference frame extrapolated to February 15^{th} 1999. The RMS of the daily repeatabilities in Table 6.1 reflects the type of receiver used and the site at which it was operated. The smallest RMS is achieved with the PGF stations (ASHTECH) and the highest with the campaign stations (Turbo Rogue). The station BRAD was operated in an urban environment with several trees shielding the view of low elevation satellites which explains the much higher RMS of the daily repeatability from this station. Schaer [1999] investigated ionospheric effects on GPS observations from Turbo Rogue receivers from the IGS network and showed that the quality of the observations around local noon decreased with decreasing latitude. In addition, the number of satellites that can be tracked by the Turbo-Rogue receivers is limited to 8, which reduces the number of observations considerably.

Before estimating the final tropospheric parameters daily normal equations with all 23 stations were built. These normal equations contain station coordinates and tropospheric parameters as unknowns where the integer ambiguities were pre-eliminated. 48 daily troposphere parameters per station were estimated with coordinates held fixed on the mean value of the daily solutions (Table 6.1).

Station	days	$\Delta North$ [mm]	$\Delta East$ [mm]	ΔUp [mm]	Lon. ° ' "	Lat. ° ' "	Height [m]
PGF1	16	2	3	6	-156 41 23.8049	19 17 35.9089	698.350
PGF2	16	2	3	5	-156 48 21.0685	19 19 23.5894	723.378
PGF3	16	3	2	8	-156 46 11.3070	19 17 05.9070	223.974
PGF4	16	3	2	6	-156 47 53.3435	19 15 52.3870	41.844
PGF5	17	3	3	7	-156 43 03.7100	19 16 40.4285	288.788
PGF6	17	3	3	9	-156 40 36.1721	19 14 54.9609	58.183
BILL	16	4	5	7	-156 31 30.7814	19 12 01.9999	279.299
BRAD	8	8	25	42	-155 04 06.0067	19 23 43.5422	50.491
CRAN	14	4	5	17	-156 32 55.2905	19 16 31.6056	658.143
JENI	17	3	4	12	-156 51 36.7665	19 30 57.0009	676.890
KONA	2	-	-	-	-157 56 27.1702	19 43 35.7576	26.361
HELA	14	3	3	6	-156 38 08.9114	19 28 36.0203	1758.379
HOLE	15	3	5	8	-156 52 17.5454	19 18 53.5834	408.397
ELEP	15	3	4	8	-156 28 30.2059	19 27 01.0133	3378.162
GOPM	11	2	4	7	-156 46 39.5267	19 19 20.3751	759.288
KAEP	10	3	2	8	-156 52 42.9186	19 16 51.2594	38.012
KOSM	16	2	3	6	-156 41 00.7334	19 21 47.9596	990.300
KTPM	11	3	2	9	-156 50 23.5186	19 20 28.7659	783.033
MANE	16	2	3	9	-156 43 36.2805	19 20 20.6064	996.553
MLPM	14	2	3	5	-156 36 50.8510	19 29 31.2129	2059.128
MOKP	16	3	6	9	-156 24 02.2555	19 29 07.2498	4132.748
NUPM	12	2	4	6	-156 49 28.9211	19 23 05.0008	933.259

Table 6.1: RMS of daily coordinate differences in the directions North, East and Up and the mean position of the stations in geographical coordinates. The coordinates of all stations were estimated with the five IGS stations MKEA, KOKB WHIT, TSKB and KWJ1 held fixed on the ITRF96 reference coordinates extrapolated to February 15^{th} 1999. Only one coordinate solution was calculated for the station KONA.

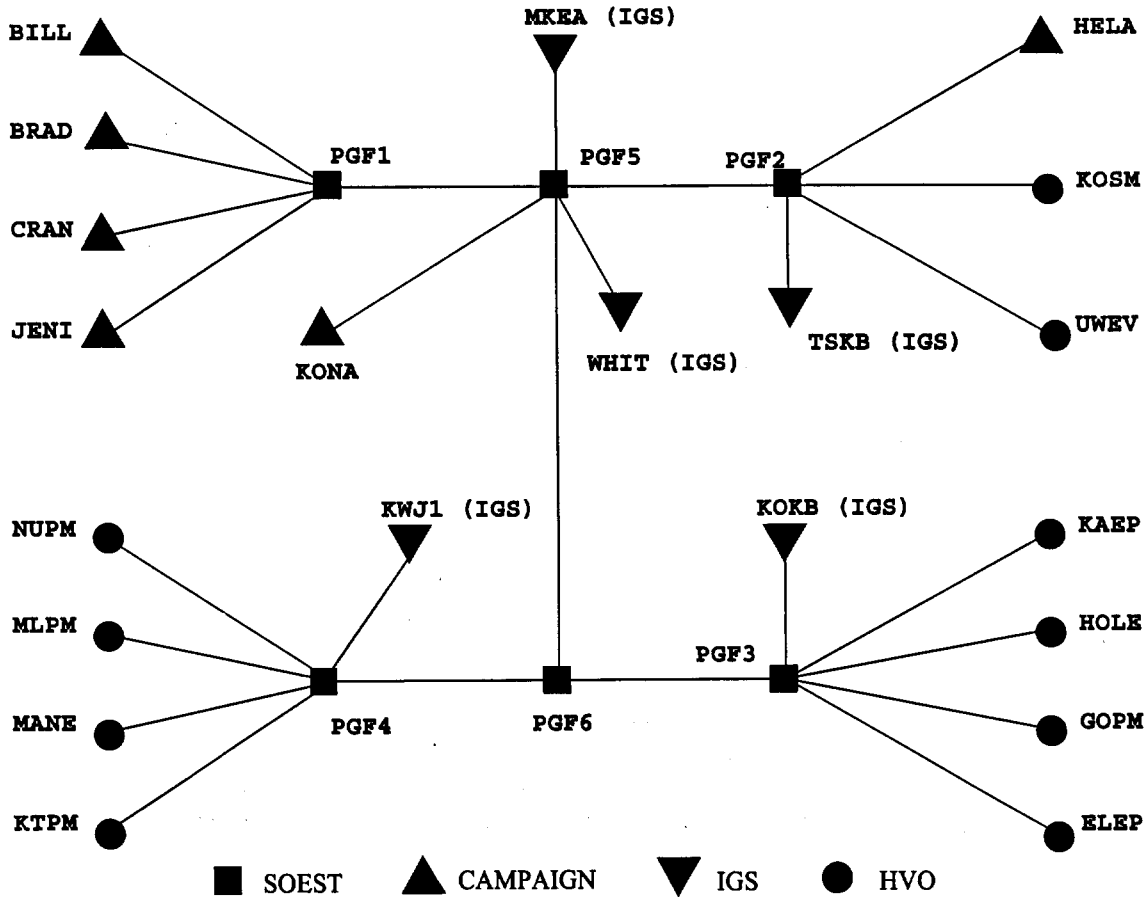

Figure 6.2: Schematic view of the baseline configuration used in the processing of the GPS network

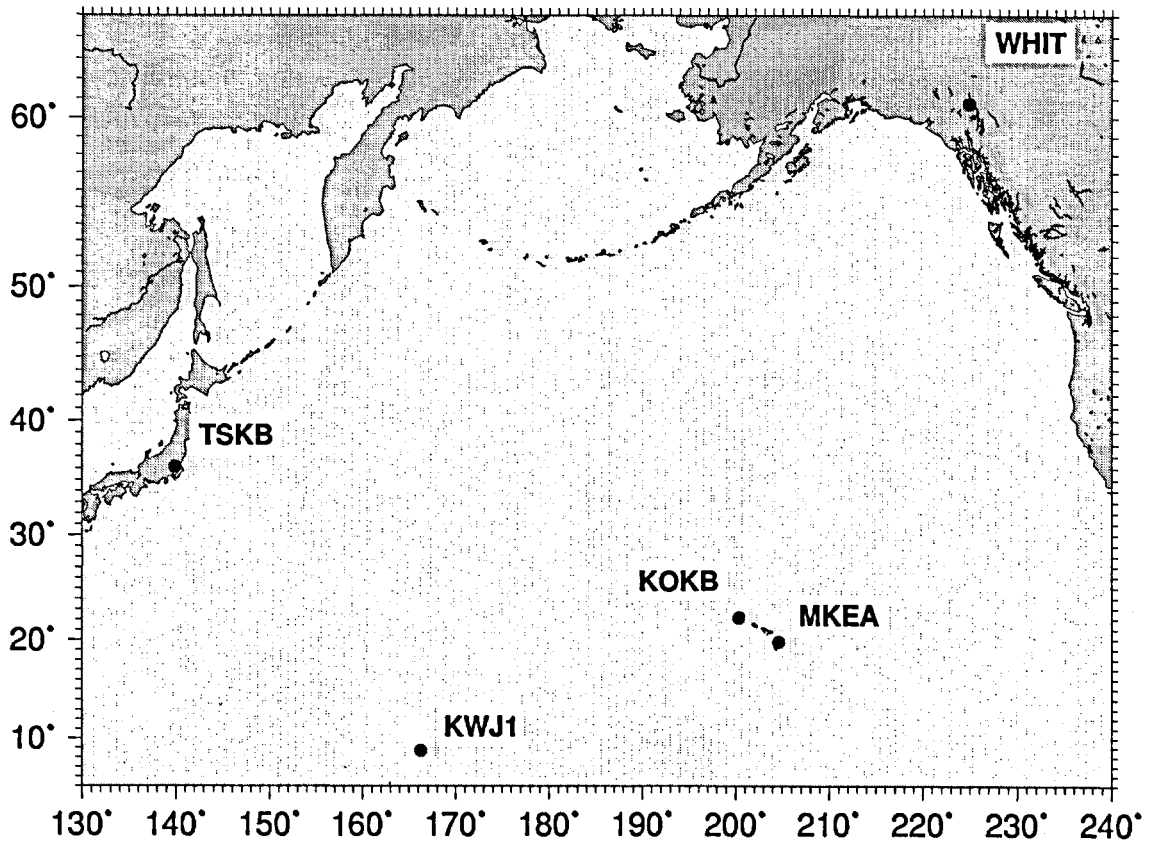

Figure 6.3: IGS stations used in the processing to estimate coordinates of the campaign stations. The baselines between the IGS stations and the Hawaiian network stations range from 30 - 4500 km

6.2.2 WVR Processing

The two ETH WVRs were operated at the BILL and HVO site (see Figure 6.1) and recorded continuously during the campaign period. Unfortunately the measurements from the instrument operated at the HVO station could not be used for water vapor estimates due to a hardware failure. Except of two days with rain (21^{nd} and 22^{th} of February) the second WVR worked well throughout the period. Inversion coefficients were calculated with radiosonde launches from Lihui and Hilo airport (see Table 4.2) with a distance of about 500 and 30 km from the WVR stations, respectively. For comparison, inversion coefficients were also calculated from the LIHU radiosonde launch station. The differences in c_{eff} are, however, small. So we decided to use the coefficients calculated from the HILO radiosondes.

6.2.3 Meteorological Modeling

Figure 6.4 shows all meteorological recordings made during the period. The horizontal lines indicate the duration of meteo recordings from ground stations whereas the vertical lines indicate radiosonde launches together with information of the launch site by the color of the line. Ground Meteorological data were recorded at ten GPS sites. At six of the permanent PGF GPS stations temperature, pressure and relative humidity are recorded at intervals of 10 minutes. Four portable Meteo logging units were installed at the stations BILL, BRAD, CRAN, HELA, KONA and MOKP. The meteo unit at the station MOKP (summit of Mauna Loa 4132m) was a VAISALA MAWS Automatic Weather Station provided by KELAG Inc. Schwerzenbach, Switzerland for the experiment. The other three units were made by CAPTEC Switzerland equipped with a dew point temperature sensor to calculate the relative humidity. The VAISALA and CAPTEC pressure sensors were compared with a calibrated digital pressure gauge SETRA, model 370. The accuracies of the meteo units are listed in Table 6.2. The pressure offsets between the meteo units and the SETRA pressure gauge were less than 1 hPa which is within the resolution of the signal output.

The radiosondes used in the experiment were of the type VIZ MARC II MICROSONDE. These sondes measure pressure, temperature and relative humidity. The recordings are transmitted by radio signals in the FM band to a receiver at the ground at a rate of one second. From the receiver the thermodynamic data are decoded and sent via RS-232 to a personal computer. There the data are further processed to get the desired meteorological parameters. Calibration information is encoded in the radiosonde EEPROM and is transmitted with the signal. At launch time pressure recordings from the sonde and the SETRA barometer at ground were registrated to avoid introducing a bias in the pressure to height conversion. The manufacturer's calibrations of the temperature and humidity sensors were used.

The height of the radiosondes were calculated with the formula published by Richner and Viatte [1995] based on the hydrostatic equation in the form

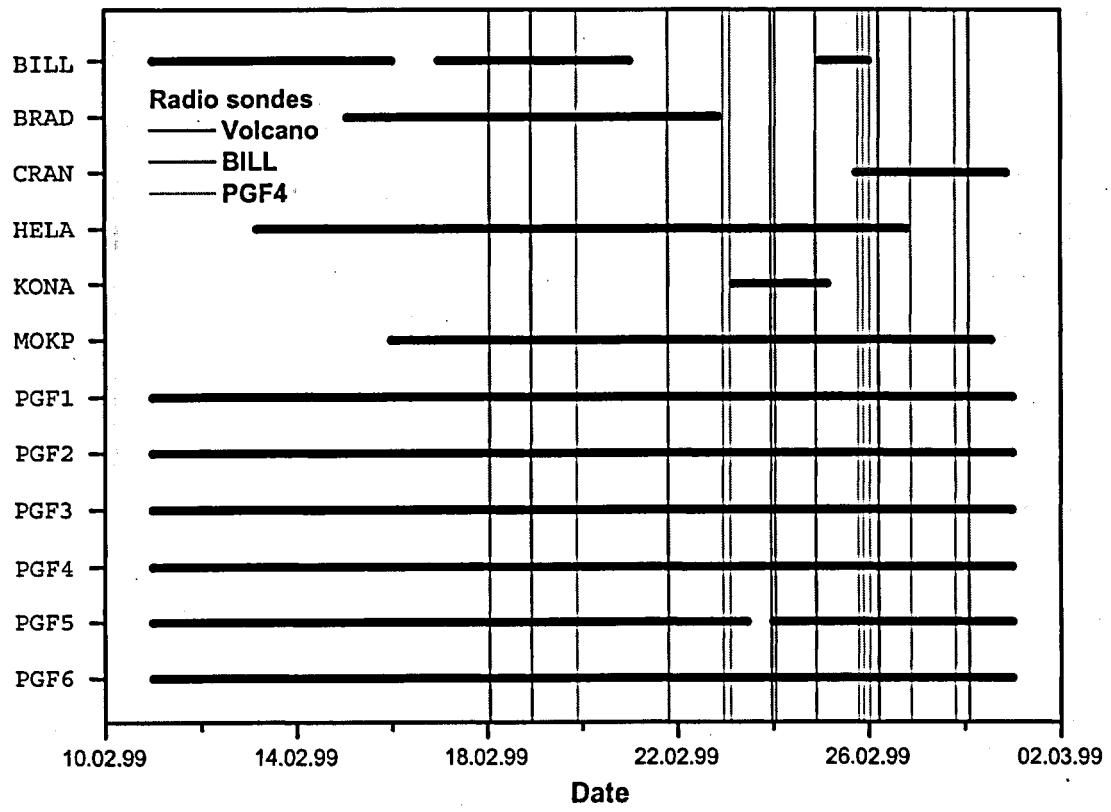

Figure 6.4: Meteorological recordings during the campaign period. The horizontal lines represent the ground based observations and the vertical lines indicate radiosonde launches.

$$z = -\frac{R}{g}\int_{p_0}^{p} T_v \, d(lnp) \tag{6.1}$$

where z is the geopotential height difference between the layers with pressure p_0 and p, R is the universal gas constant for air, T_v is the absolute virtual temperature of the air and g is gravitational acceleration. The integral in Eq. 6.1 can be rearranged to get Eq. 6.2.

$$z_k = z_{k-1} + \frac{R}{g}\frac{T_{v,k-1} + T_{v,k}}{2} ln\frac{p_{k-1}}{p_k} \tag{6.2}$$

The height z is calculated by successive accumulation of the thickness of horizontal isothermal layers by the indices k and $k-1$ indicating upper and lower boundaries, each giving pressure temperature and humidity. The reference pressure $P_{0,ref}$ measured at the launch site with the SETRA barometer and the sonde pressure P_0'

	Pressure [hPa]	Temperature [^oC]	Relative humidity [%]
Radiosondes			
Range:	3-1080	-90< T <60	5 -100
Accuracy:	± 0.5	± 0.2	± 2 (RMS)
Resolution:	0.1	0.1	1
CAPTEC Meteo unit			
Range:	600 -1100	-40< T < 60	0 - 100
Accuracy:	± 1.0	± 0.1	± 0.5
Resolution:	0.6	0.01	0.1
VAISALA MAWS			
Range:	600-1100	-40< T < 60	0-100
Accuracy:	± 0.3	± 0.1	± 3
Resolution:	0.1	0.1	1
SETRA, Model 370			
Range:	600-1100	-	-
Accuracy:	± 0.1	-	-
Resolution:	0.01	-	-

Table 6.2: Meteorological instruments used in the experiment with their respective measurement ranges, resolution and accuracy.

from the radiosonde sensor was used to correct the pressure measurements along the profile by

$$P_k'' = P_k' \left(\frac{P_{0,ref}}{P_0'} \right) \tag{6.3}$$

where P_k' and P_k'' are the measured and corrected pressure, respectively. The importance of pressure calibration on the ground on the height accuracy was investigated by Richner and Viatte [1995]. Height errors of up to 1.4 km at 25 km caused by introducing a 5 hPa bias in the ground pressure were calculated. To validate the pressure to height conversion the radiosonde pressure measurements were compared with pressure measurements from the VAISALA meteo station operated on top of Mauna Loa at 4132 m a.s.l. The height differences were all below 30 meters which corresponds to about 1.5 hPa. Since relative humidity is not a measure of the water vapor content the humidity measurements from the radiosonde, given as relative humidity, have to be converted to partial water vapor pressure e and/or absolute humidity ρ_v. The conversion from relative humidity to water vapor pressure is given by

$$e = e_{sw} \left(\frac{RH}{100} \right) \tag{6.4}$$

where e_{sw} is the saturated water vapor pressure over a liquid water surface. We used

the modified Goff-Gratch [Goff, 1965] equation for water to calculate e_{sw}.

$$\begin{aligned} log_{10}(\frac{e_{sw}}{e_1}) = 10.79586 \left(1 - \frac{T_1}{T}\right) - 5.02808\ log_{10}\left(\frac{T}{T_1}\right) \\ +1.50474\ 10^{-4}(1 - 10^{-8.29692(\frac{T}{T_1}-1)}) \\ +4.2873\ 10^{-4}(10^{4.76955\ (1-\frac{T_1}{T})} - 1) \\ -2.2195983 \end{aligned} \tag{6.5}$$

where $e_1 = 1013.25$ hPa: saturation pressure at the steam point
$T_1 = 273.16$ K: triple point temperature
$T = 273.16 + \Theta$: temperature in Kelvin and Θ is temperature in ^oC

By inserting the expression of e_{sw} in Equation 6.4 and combining this with Equation 2.19 we have an expression for absolute humidity ρ_v. The IPWV was calculated by numerical integration of 2.18 using the trapezoidal method

$$IPWV = \frac{1}{2}\sum_{k=0}^{n}(\rho_k + \rho_{k-1})(z_k - z_{k-1}) \tag{6.6}$$

Comparison of IPWV from radiosondes calculated with the often used empirical equation [Magnus, 1844] $e_{sw} = 6.1086\ e^{(17.865*t/245.52+t)}$ and the Goff-Gratch expression for water vapor saturation pressure was below 0.1%. In Figure 6.5 the three radiosonde launches (a, b and c) display the evolution of the vertical temperature and water vapor pressure profile during the period where radiosondes were launched. The temperature inversion zones start at about 9 km (a) drops then down to about 2 km (b) characterized by a sharp increase of almost 10°C and rises slowly at the end of the period (c) where the sharpness of the temperature increase is diminished.

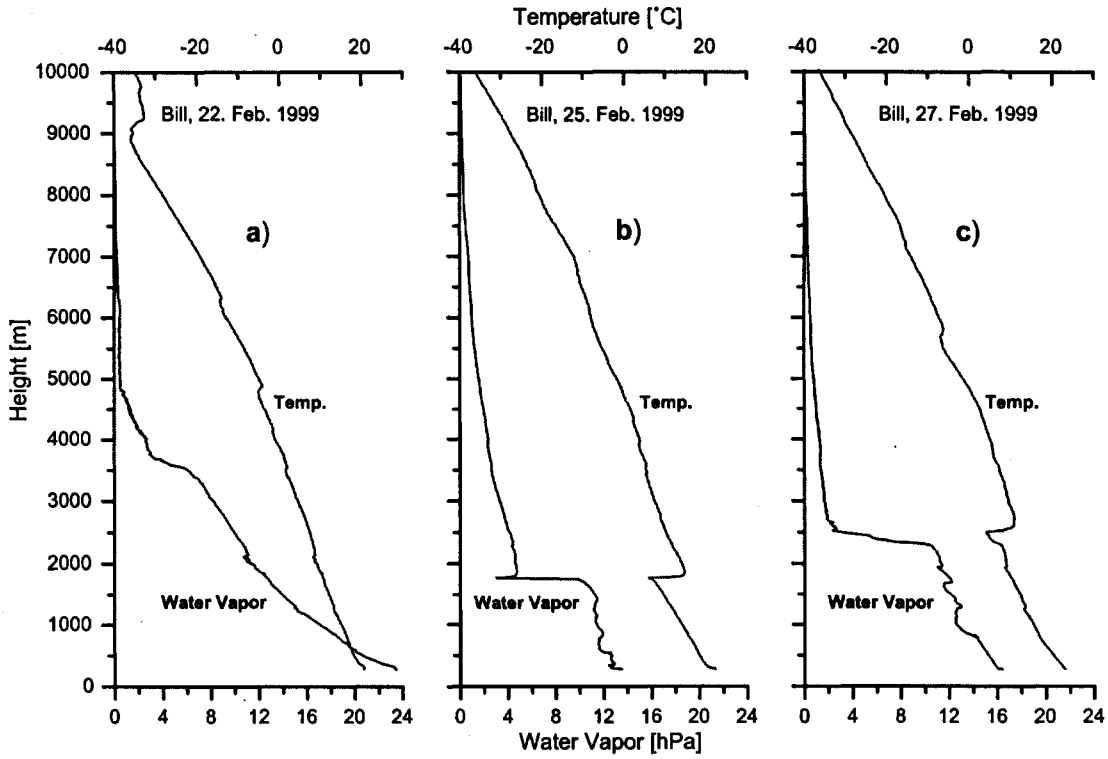

Figure 6.5: Three profiles (a,b and c) of temperature and water vapor pressure recorded at the station BILL. The three profiles (from left to right) show trade wind inversions at the altitudes of about 9, 1.8 and 2.0 km. The dry and warm trade winds cause a rapid decrease in water vapor pressure (profile b and c). The breakup of this inversion layer is visible in profile c where the sharpness of the temperature increase is weakened.

6.3 Comparisons and Results

6.3.1 GPS results

Figure 6.6 shows 16 days of GPS IPWV estimates from 23 stations. In general the highest amount of IPWV were estimated from the lowest stations and vise versa. The temporal change in the bandwidth of IPWV reflects the variability of water vapor content in the layer between the lowest and highest station at 40 m and 4132 m, respectively. The percentages of IPWV within the highest and lowest stations was 90.1% $\pm$ 0.6% for the whole period with a drop to about 83% during the two day period with rain. The IPWV estimates from the highest station Mauna Loa (MOKP) drops below 0 mm at a few occasions at the beginning and at the end of the period which may be caused by wrong pressure modeling due to missing data during the periods. The number of estimates below 0 mm is 48 with a mean and standard deviation of 0.5 mm $\pm$ 0.5 mm which is less than 8% of all estimates at this station.

6.3.2 GPS-Radiosonde Comparisons

In Figure 6.7 comparisons of GPS IPWV estimates and 16 radiosonde launches (GPS - radiosonde) together with the height of the temperature inversion layer (square dots) are shown. The radiosonde measurements were integrated from the heights of the GPS stations and compared with the GPS IPWV estimates at the corresponding height. The lateral distances between the launch site and the GPS station range from 0 to about 40 km which may, to some extent, contribute to the biases. However, the GPS estimates at or near the launch site (marked with blue dots) show comparable offsets with other stations. The comparisons also show height-dependent offsets which are pronounced for the launches number four and five and a change from positive differences at the beginning of the period to negative differences at the end of the period. Because of this time dependency it is unlikely that the sensors of the sondes used at the beginning of the period should be biased in one way and in the opposite way at the end of the period. The GPS - radiosonde differences are especially large for the lower stations at the end of the period and seem to be constant for launches number 8, 9, 10, 11, 13 and 14. In the search for possible explanations of the offsets, possible biases of the radiosonde measurements were investigated. From the pressure comparisons at 4132 meters (see above) error contributions from wrong radiosonde heights could be neglected. A reduction of 15 % $\approx 3^{o}C$ of the temperature measurements or 20% reduction of the relative humidity measurements was necessary to remove the GPS - radiosonde bias. Such corrections are, however, too large and not justified because the bias changes in time.

The RMS of the daily coordinate repeatabilities (Table 6.1) does not indicate vertical movements of the points introduced by either ground motion or tropospheric effects. During the campaign period no earthquakes or large volcanic eruptions

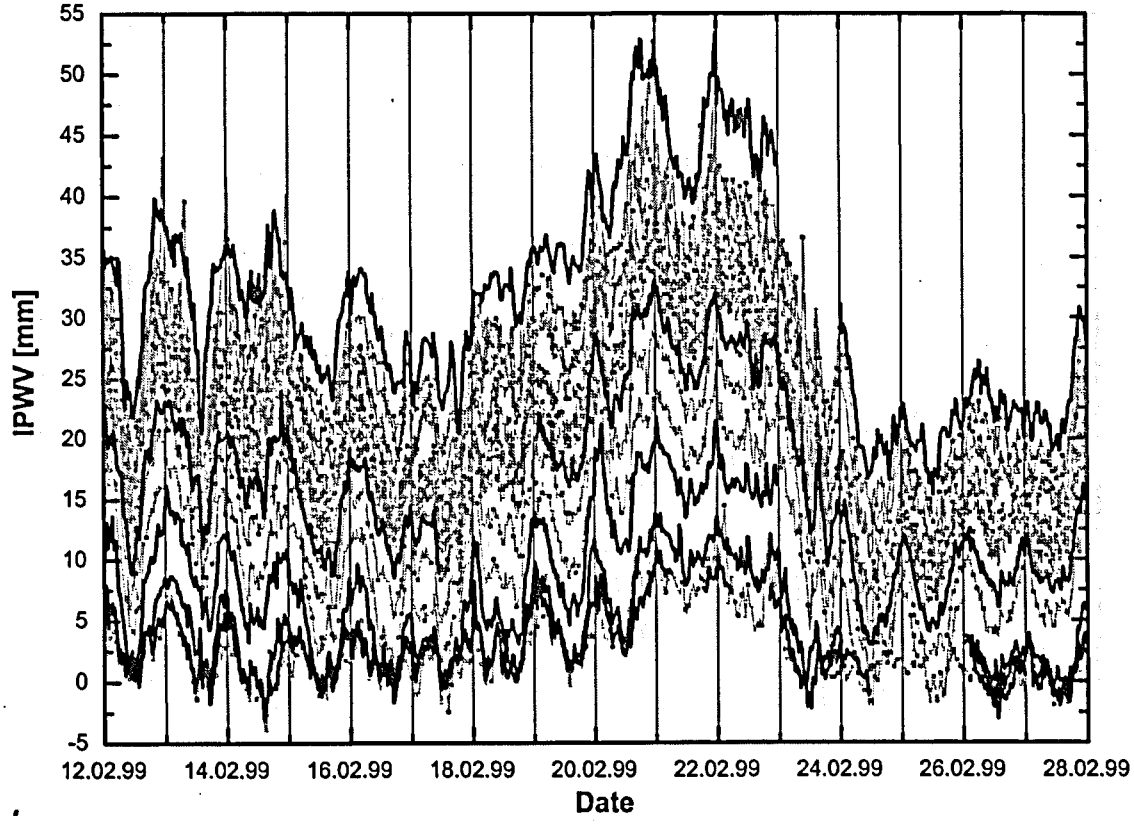

Figure 6.6: IPWV estimates from 23 stations within the Kilauea area. The four thick lines from top to bottom represent IPWV estimates from stations at 0, 1000, 2000 and 4100 m altitude, respectively. Large fluctuations of about 30mm for the lower stations were measured during the campaign period. The vertical lines are day boundaries of UT and correspond to 13:00 hours local time. The daily fluctuations of water vapor with a maximum at local noon are clearly visible. The temporal change in the bandwidth of IPWV reflects the variability of the water vapor profile. Two days (21^{nd} and 22^{th})of heavy rain fall caused a major rise in IPWV. A pronounced drop in IPWV after the rain period of about 25mm IPWV was measured.

were recorded [Lisowski, 1999]. In Figure 6.7 the height of the temperature inversion layer together with a color scale indicating the sharpness of the temperature increase is shown. The correlation between the GPS - radiosonde IPWV differences and the height of the inversion layer is clearly visible. The corresponding water vapor pressure profiles (appendix) show a rapid decrease at the inversion zone. Elevation dependent models such as the mapping function may contribute to the GPS - radiosonde bias because of such irregular water vapor distributions.

A subset of 10 network stations all equipped with Dorne Margolin antennas and

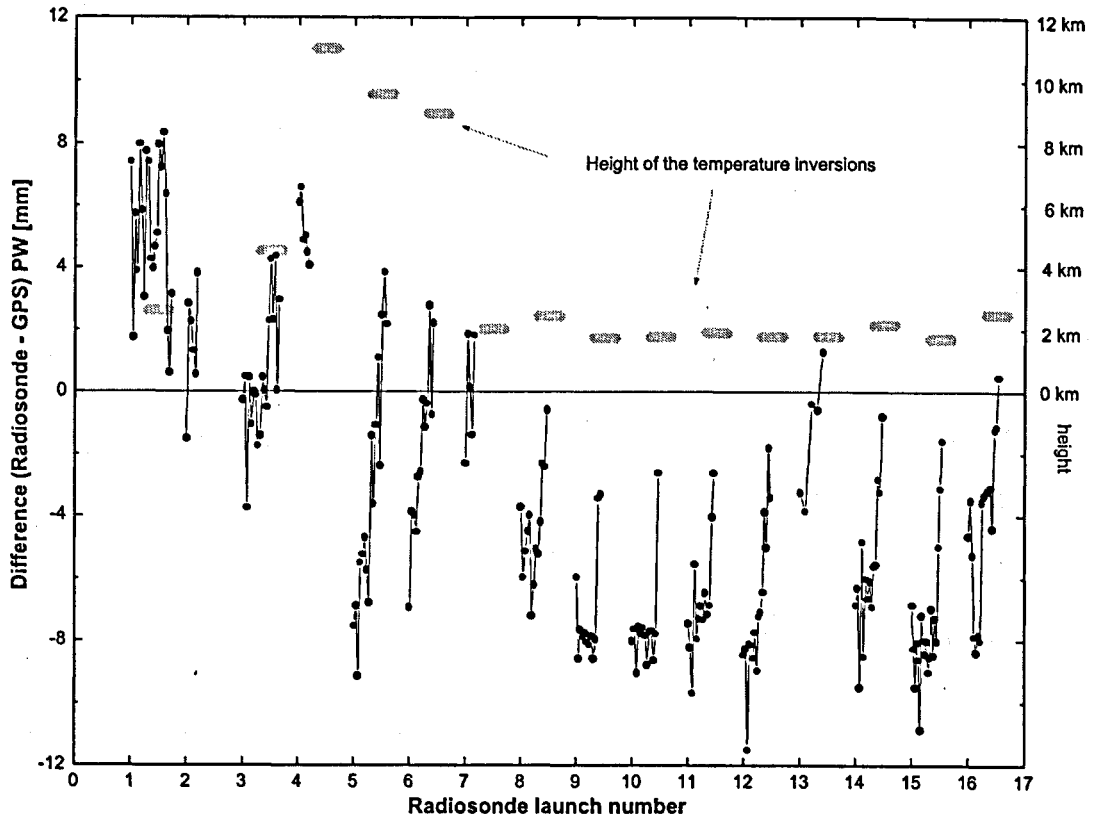

Figure 6.7: IPWV differences between GPS estimates and radiosondes measurements shown as black squares. The radiosondes were integrated from the height of every GPS station. The grey bricks in the upper part of the Figure indicate the height of the temperature inversion measured (see legend).

ASHTECH Z-XII3 receivers except for the station MLPM which was equipped with a Trimble L1/L2 geodetic antenna and a Trimble SSI receiver was combined with the five IGS stations used in the network solution described above. Twelve tropospheric parameters together with three coordinate parameters were estimated per day and station over 17 days. Three such solutions with elevation cut-off angles of 10, 20 and 30 degrees were compared with a solution using a elevation cut-off angle of 10 degrees with coordinates fixed of those of the network solution described above. Tropospheric estimates with an RMS higher than 5 mm delay were excluded from the comparison. The mean difference of the tropospheric estimates with respect to the solution with fixed coordinates were calculated for the three elevation cut-off angle solutions. Figure 6.8a shows the differences in total zenith delay as a function of the corresponding differences of the height component. The linear fit of the data was calculated with respect to the coordinate axis. The negative slope of about -0.5 shows that an increase of the tropospheric estimates is followed by a

decrease of the height component by a factor of 2. The IGS antenna phase center models provided by the University of Berne describe no elevation dependency for the Dorne Margolin antenna type. The Hopfield mapping function was used to model the elevation dependency of the atmosphere. Santerre et al. [1995] compared 15 different mapping functions and their effects on station coordinates for three sites at different latitudes. Their results revealed the least satisfactory performance for mapping functions based on the Hopfield model [Hopfield, 1969]. This is because these mapping functions disregard the geometric part of the propagation delay. The effect of the Hopfield based mapping functions on coordinate heights compared to the Herring [1992] mapping function was on the order of 30 mm at 10 degree elevation to about 4 mm at 30 degrees. In case the mapping function would perfectly model the atmospheric propagation delay at any angle the absolute estimates of troposphere and coordinates would not show any elevation dependency. However, the stochastic errors of the parameters may increase due to a decrease in observation geometry (see Figure 5.2).

From this investigation we conclude that a part of the GPS - radiosonde bias ($\approx$2 mm IPWV) may be explained by inadequate modeling of the atmospheric propagation by the Hopfield mapping function. The mean tropospheric estimates for the three elevation cut-off angles are plotted against height in Figure 6.8b. In general the delay differences are reduced with height except for the 30 degree solution from the station at 2000 meter. The sign of the delay differences with height go from positive except for one station to negative at 2000 meters to positive at the top of Mauna Loa. The significance of the change to negative difference at 2000 meter is, however, questionable due to the number of stations compared to the difference below 1000 meters. One can speculate whether the height of the temperature inversion zone (and the corresponding rapid decrease of water vapor) at $\approx$ 2000 meters may be the reason for this shift or not. The station BILL showing negative differences was operated in the dry area of the network which may explain the "outlier" thus demonstrating the very particular microclimatical weather conditions dominating the southern part of Big Island.

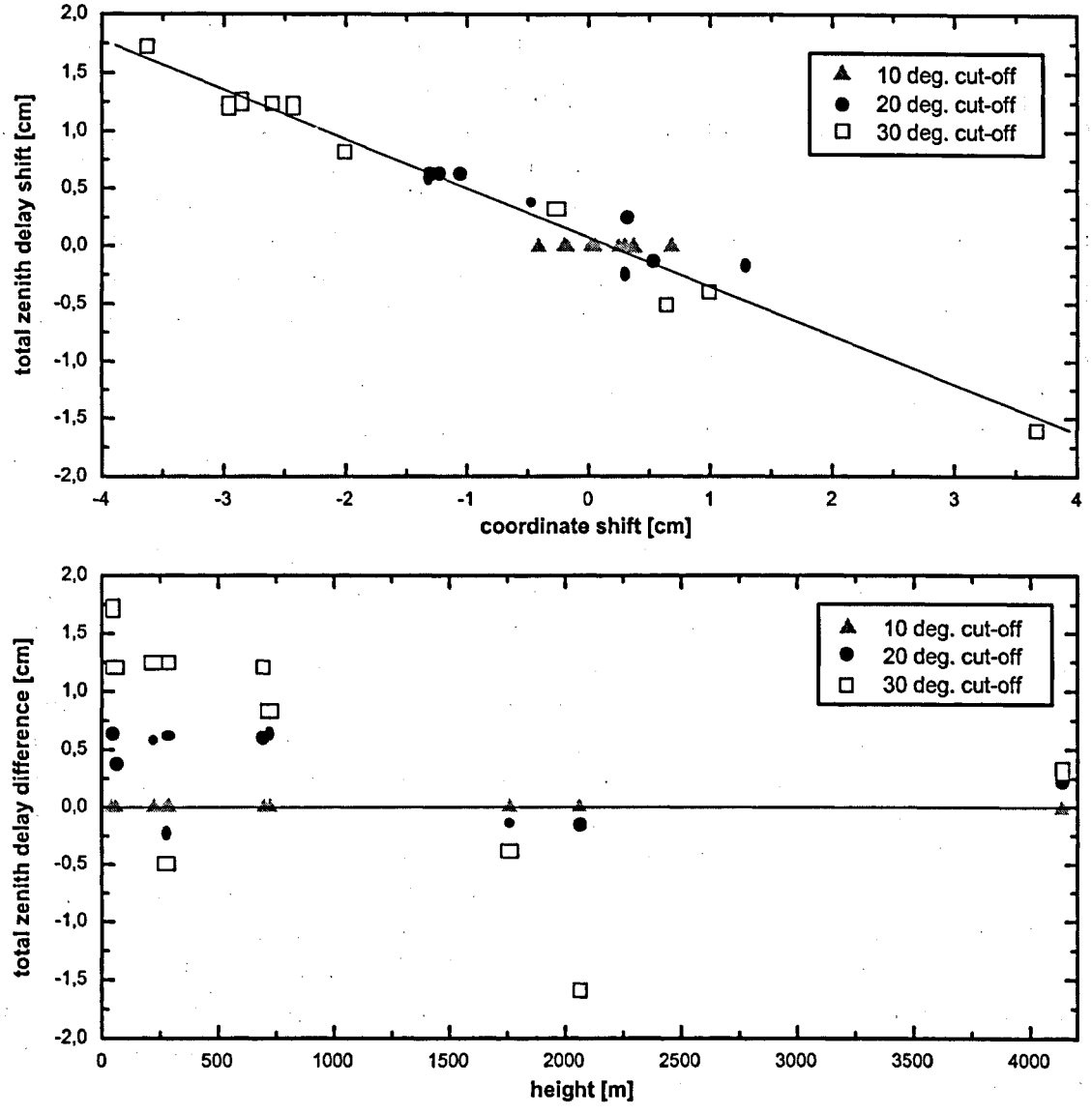

Figure 6.8: a) Correlation between shifts in delay and height coordinate estimates. A 10 degree cut-off solution with fixed coordinates was used as reference to calculate the mean differences of total delay and coordinate estimates with 10 20 and 30 degree cut-off angles. Each point represents the mean difference of 17 daily height solutions and the mean difference of all tropospheric estimates with respect to the reference solution. The slope of the linear fit with respect to the coordinate axis is -0.48. A downward shift in the coordinate estimate of 2 cm is followed by an upward shift of about 1 cm the tropospheric estimate. b) Mean differences of zenith delay as a function of height. The sign of the delay difference with height goes from positive except for the station BILL to negative at 2000 meters to positive at the top of Mauna Loa.

6.3.3 GPS-Modeling Comparisons

Atmospheric water vapor was modeled with COMEDIE (see chapter 3) with radiosonde and ground based measurements from the stations shown in Figure 6.4. At each GPS station zenith wet path delays were calculated and compared with the GPS estimated zenith wet path delays. Figure 6.9a and b display zenith wet delay differences for the period where radiosonde measurements were available. The gap in the time series was due to missing radiosonde measurements during a period of two days with rain. The offset of the differences in Figure 6.9a are more of less constant compared to the differences in Figure 6.9b were large variations are visible. The mean difference and standard deviation for every station during the two periods displayed in Figure 6.9a and b are plotted against height in Figure 6.9c and d. The elevation dependency of the differences from the first period (c) shows a constant offset for stations below 800 meters from where it increases to the station at 2000 meters and then decreases again to the station at 4132 meters. However, most of this variation is within the standard deviation indicated by the error bars.

In contrast, the elevation dependency of the offset in the second period is much more pronounced and the offsets seem to decrease almost linearly with height. The differences correspond to the GPS - radiosonde differences shown in Figure 6.7. This is not surprising since the modeling uses this information. The weight of the radiosonde measurements below 1000 meters are, however, limited because measurements from ground meteo stations dominate the interpolated results. In contrast the model of the atmosphere above the highest ground meteo station at 4132 meter is solely determined by the radiosonde measurements. Between these limits measurements from two ground meteo stations at 1758 and 4132 meters and radiosondes are the main contributors for the interpolation of meteorological parameters.

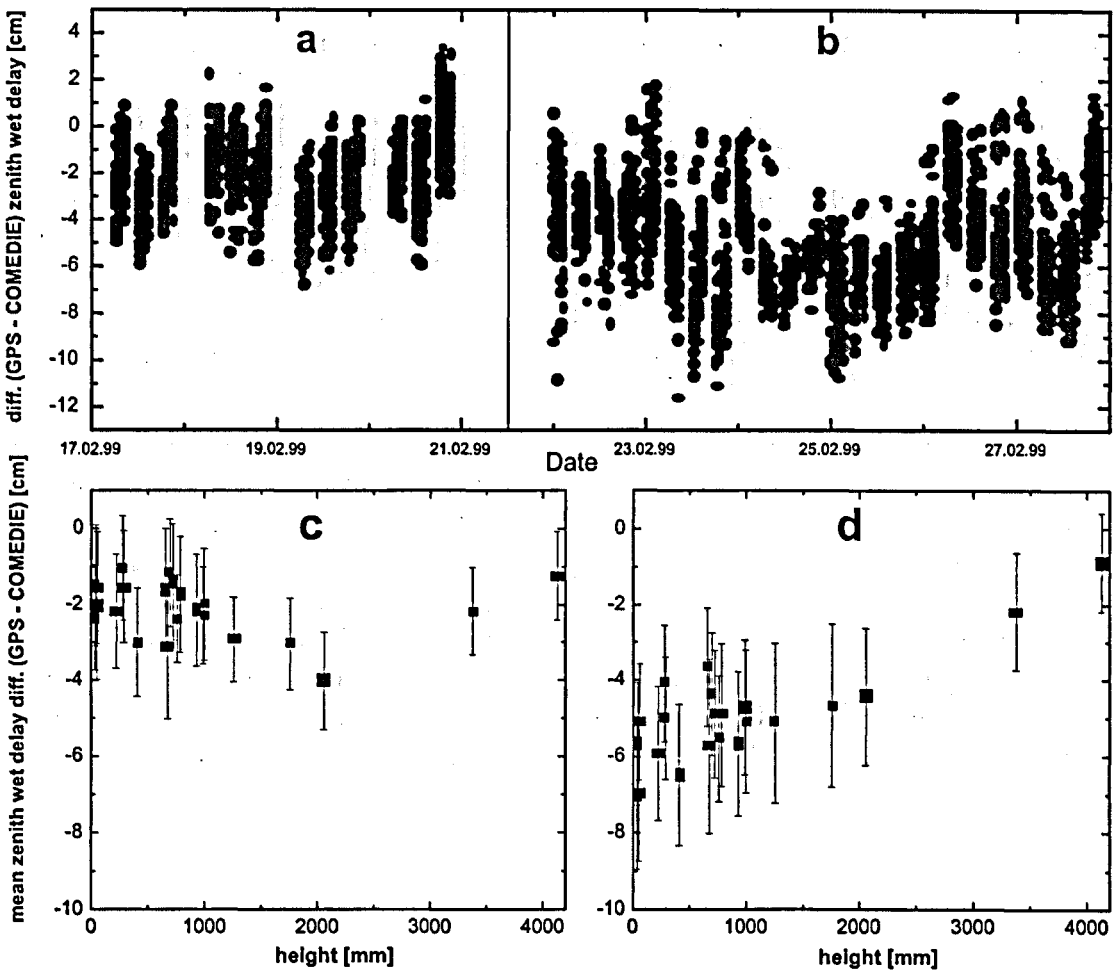

Figure 6.9: a and b) Differences in zenith wet delay between GPS estimates and modeling. About 200 differences (30 minutes intervals) for each of the 22 GPS stations are displayed. The time series is divided into two parts a and b by the vertical dashed line. For each station the mean of the differences shown in a and b is plotted with respect to height in c and d, respectively. The standard deviations of the differences at each station are indicated by error-bars.

6.3.4 Results and Intercomparisons at the station BILL

The comparison results from the station BILL are listed in Table 6.3. The standard deviation of the GPS - WVR differences for all data is about 1 mm higher than have been seen from other comparison campaigns. The differences plotted in Figure 6.10b change during the period as indicated by the vertical lines. The differences ranges from -0.6 in sector C to 2.04 in sector B. The mean and standard deviation within the sectors A to C are also listed in Table 6.3. To verify whether these "jumps" are caused by the WVR or GPS we compared the WVR estimates with water vapor measurements from the co-located Solar SpectroMeter (SSM). Figure 6.12a and b show first results from the SSM compared with WVR. The dots and squares indicate that two different absorption spectra were used to calculate the SSM-IPWV. The results listed in Table 6.3 document a good agreement with GPS and WVR. As can be seen in Figure 6.12b only few results from the SSM could be processed due to cloud cover. The verification of the "jumps" mentioned above is therefore not justified. The GPS - Modeling comparison (Figure 6.11) also shows jumps in the mean differences indicated by the three sectors D, E and F. The differences during the period D increase steadily with time most probably due to a build up of an inversion layer which causes deviations from an exponential distribution modeled by COMEDIE. The rapid decrease of the differences at the end of sector D is due to the high altitude measurements from the radiosondes (see also Figure 6.4). The mean difference and standard deviation of the data in sector E is relatively low and can be compared with section B in Figure 6.10. In sector F the mean differences are shifted by more than 5 mm IPWV. The difference between sector E and F reflects the GPS - radiosonde differences in Figure 6.7. The GPS - WVR and GPS - Modeling comparisons both reveal similar shifts from positive to negative before and after the rain period at the maximum IPWV peak. However, the differences are smaller for the GPS - WVR comparison than for the GPS - Modeling comparison.

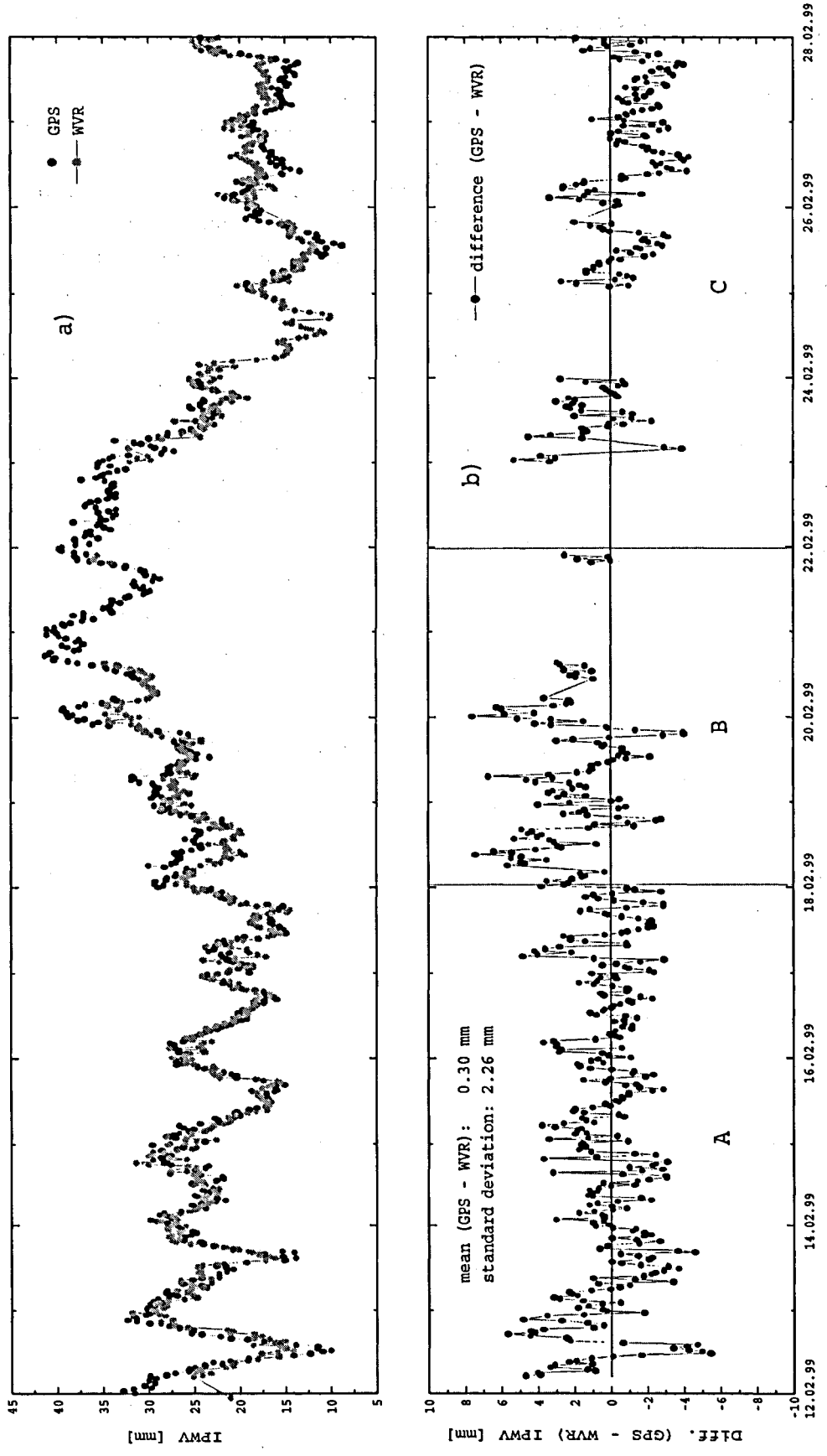

Figure 6.10: a) IPWV estimates from GPS and WVR and b) GPS - WVR differences as observed at the station BILL. Changes in the offsets between GPS and WVR are marked with vertical lines dividing the time series into three intervals A, B and C.

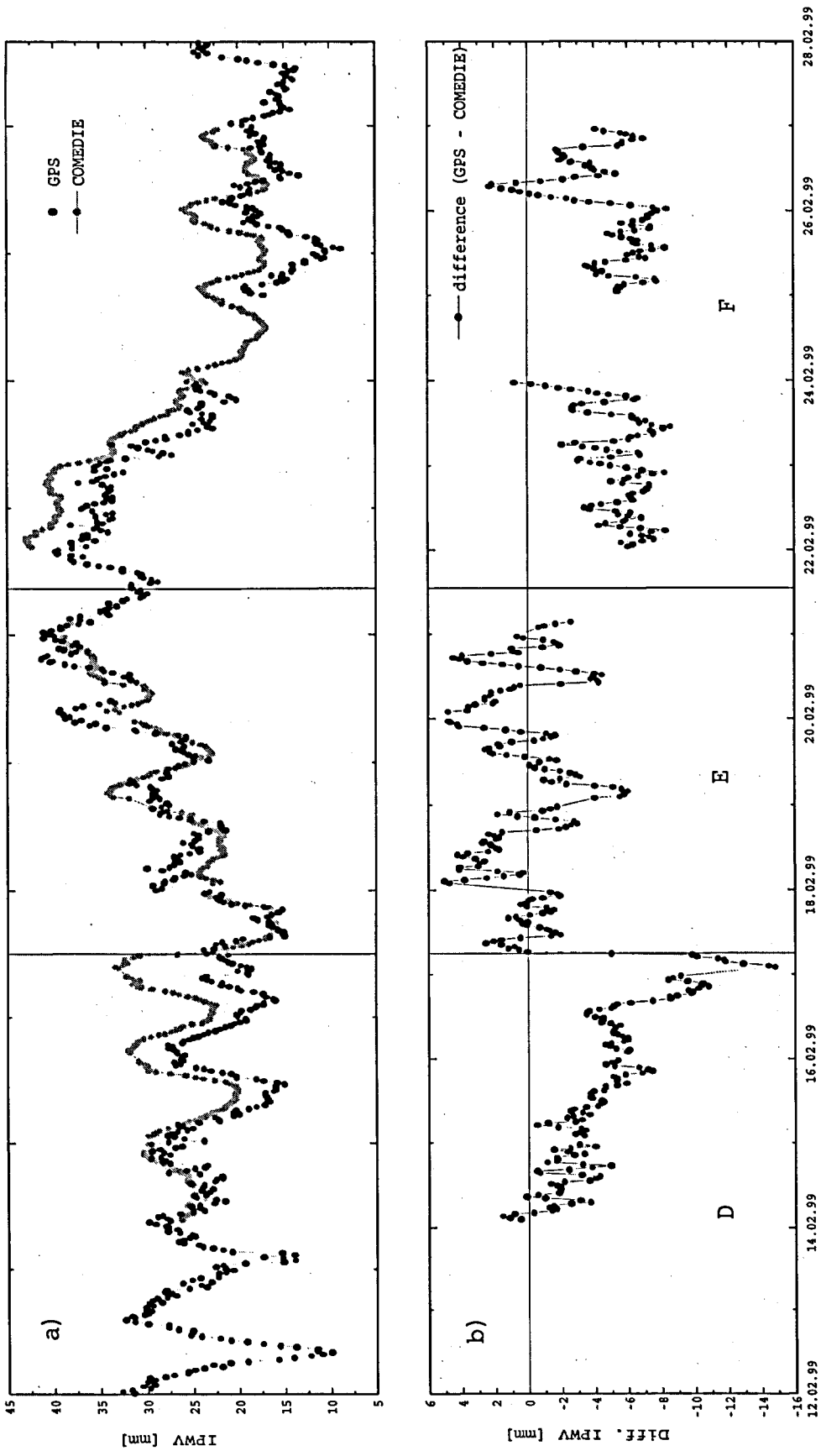

Figure 6.11: a) IPWV estimates from GPS and modeling at the station BILL. b) Differences (GPS - Modeling) of the estimates shown in a. The three time intervals D, E and F are identical to those in Figure 6.10. The rapid reduction of the offset in D is due to the positive impact of radiosonde measurements on the modeling. The differences within the two time intervals E and F were calculated with radiosonde measurements. Large differences in the offsets from the two periods can be seen. The gap in the time series of the modeling results is due to missing radiosonde measurements.

Comparison	Period	Difference	Standard deviation
GPS-WVR:		IPWV [mm]	IPWV [mm]
	A - C	0.34	2.29
	A	0.14	2.01
	B	2.04	2.32
	C	-0.6	1.94
GPS-COMEDIE:			
	D	-3.75	3.38
	E	0.38	2.74
	F	-5.06	2.21
GPS-radiosonde:		-5.25	4.74
WVR-radiosonde:		-3.84	4.75
GPS-WVR	*radiosondes**	-1.41	2.52
GPS-SSM:		0.35	1.89
WVR-SSM:		0.31	1.3

Table 6.3: Intercomparison statistics of the five methods GPS, WVR, radiosondes, COMEDIE and SSM at the station BILL.

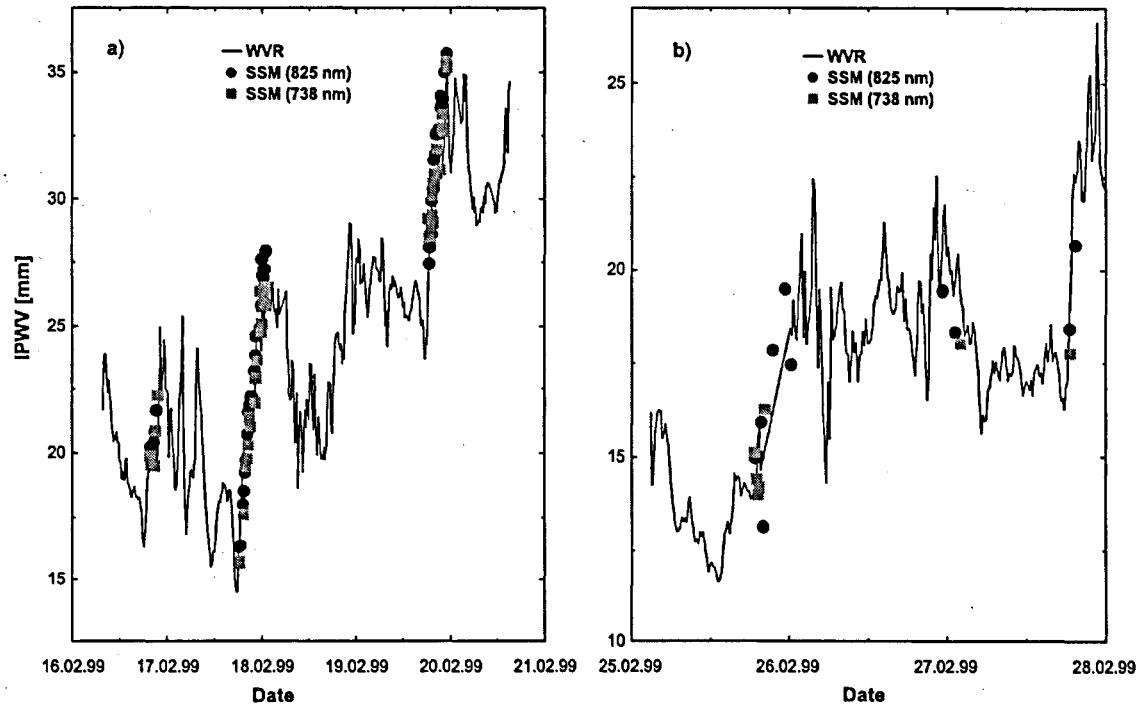

Figure 6.12: IPWV estimates from SSM and WVR. The SSM results shown were derived from measurements at two different absorption spectra (825.4 and 738.9 nm wavelengths).

7 GPS Tomography

7.1 Introduction

Applications of the tomographic method have been utilized and successfully established in many areas such as medicine, geophysics etc. Applying the tomographic method to resolve spatial structures of tropospheric water vapor is a new application in the field of GPS. The resolution of three dimensional water vapor distributions by the use of integral tropospheric delay measurements requires a well distributed network geometry. Since the observed signal itself carries no profile information on the water vapor distribution the design of the network geometry is important (section 7.2).

A tomographic software package called AWATOS (Atmospheric WAter Vapor TOmography Software) was developed within this work. The software is capable of assimilating data from different sources such as GPS double difference residuals (e.g. from GPS processing using the Bernese Software), slant path delays (from WVRs, solar spectrometers, etc.), and meteorological observations (radio soundings and ground based meteo). The atmosphere above the receiver network is divided into a box model and the wet microwave refractivities within these boxes are calculated using a least squares algorithm (see section 7.2). The tomographic algorithm is tested on the high density network at Hawaii and compared with radiosondes.

7.2 Inversion

7.2.1 Theory

The signals emitted by the GPS satellites propagate thorough the atmosphere with a varying speed and direction depending on the refractive index along the ray path. Ignoring the geometry effect (see chapter 2) the integral effect of tropospheric refraction is written

$$\rho = \int_A^B \mu \, ds \tag{7.1}$$

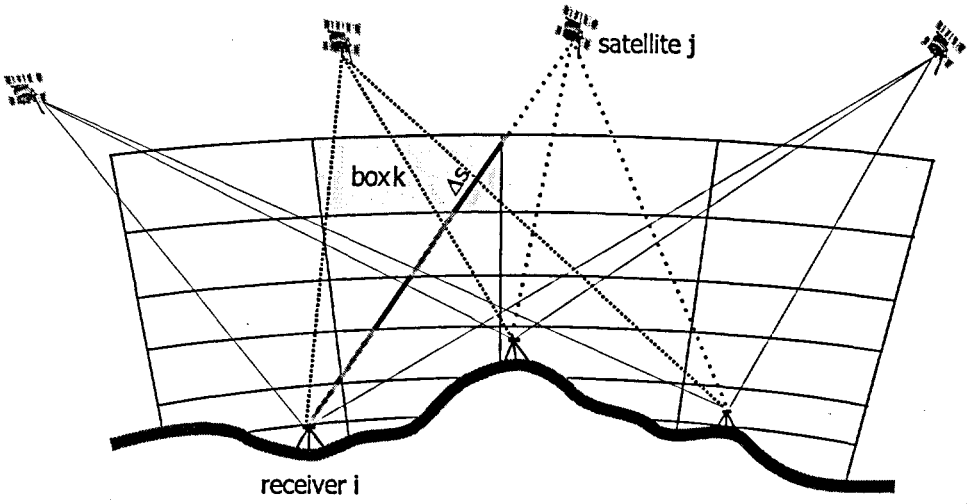

Figure 7.1: Principle of GPS tomography. The atmosphere above the receiver network is parameterized by a discrete number of box elements in which the refractivity is assumed constant. The distances (Δs) within each box is calculated by ray-tracing through the elements of the model, based on a straight line from the antenna position to the satellite.

The tropospheric model is described by a discrete number of elements in which the refractivity μ is constant. The discretion of Eq. 7.1 is

$$\rho = \sum_{i=1}^{k} \mu_i \, \Delta s \tag{7.2}$$

The observation ρ is regarded as a sum of discrete contributions $\mu_i \Delta s_i$ along the ray path where Δs_i is the distance of the ray within the box element i. The discrete observation equation can be written as a product of vectors

$$\rho = \mathbf{s}^{\mathbf{T}} \cdot \mu \tag{7.3}$$

where

$\mathbf{s}^{\mathbf{T}}$	=	$(\Delta s_1, \cdots, \Delta s_k)$	ray distance within the box element$i$
$\mu^{\mathbf{T}}$	=	$(\Delta \mu_1, \cdots, \Delta \mu_k)$	refraction within the box element$i$
k	=		number of model elements

Equation 7.3 is a linear observation equation of the unknown refraction coefficients μ_i. In matrix notation we can write

$$\rho = \mathbf{A} \, \mu \tag{7.4}$$

The inverse of Equation 7.4 is written as

$$\mu = [\mathbf{A}^T\ \mathbf{P}\ \mathbf{A}]^{-1} \cdot \mathbf{A}^T\ \mathbf{P}\ \rho \tag{7.5}$$

where $\mathbf{A}$ is the design matrix, $\mathbf{P}$ is the weight matrix of the observations. The inverse of the normal equation $\mathbf{N} = [\mathbf{A}^T\ \mathbf{P}\ \mathbf{A}]$ can be solved if the observation equation $\mathbf{A}\mu = \rho$ provides enough information to determine the model parameters μ. If this is not the case the inverse of N is singular. Below two cases are discussed to illustrate the solvability of the inversion of $\mathbf{N}$.

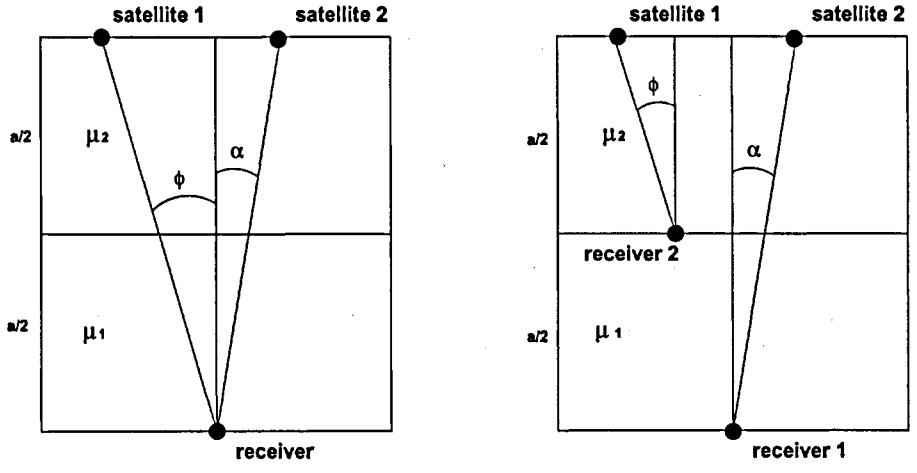

Figure 7.2: Two horizontal layers of refractivity μ_1 and μ_2 each with vertical distances $a/2$. *Left*: rays from two satellites crossing the layers and recorded by one station. *Right*: two stations at different altitudes each recording a satellite signal.

The observation equations in matrix notation for the case in Figure 7.2(*left*) is:

$$\mathbf{N} = \begin{bmatrix} (\frac{a^2}{cos^2\phi} + \frac{a^2}{cos^2\alpha}) & (\frac{a^2}{cos^2\phi} + \frac{a^2}{cos^2\alpha}) \\ (\frac{a^2}{cos^2\phi} + \frac{a^2}{cos^2\alpha}) & (\frac{a^2}{cos^2\phi} + \frac{a^2}{cos^2\alpha}) \end{bmatrix}$$

The rows of $\mathbf{N}$ are linear dependent and the matrix is singular. The inverse of a matrix is proportional to the inverse of the determinant $\mathbf{Det[N]}$ which is zero in this case. The condition of the problem is said to be ill posed since only the average refractivity $(\mu_1+\mu_2)/2$ can be calculated. In case of two stations at different altitudes each observing one satellite (Figure 7.2(*right*)) the Normal equation matrix $\mathbf{N}$ is:

$$\mathbf{N} = \begin{bmatrix} (\frac{a^2}{cos^2\alpha}) & (\frac{a^2}{cos^2\alpha}) \\ (\frac{a}{cos\phi} \cdot \frac{a}{cos\alpha}) & (\frac{a^2}{cos^2\phi} + \frac{a^2}{cos^2\alpha}). \end{bmatrix}$$

The determinant of $\mathbf{N}$ is non zero and the refractivity in each layer can be estimated. From the two examples discussed above we see that layers without at least one

receiver cannot be determined without introducing a priori information. To prevent the normal equation from being singular such a priori information of the parameters can be applied. In matrix notation we can write the a priori information as $\mu_0 = \mathbf{I}\ \mu$ where μ_0 is an arbitrary constant for all parameters. Combining this a-priori information with the observations we get

$$\begin{aligned} \rho &= \mathbf{A}\ \mu \\ \mu_0 &= \mathbf{I}\ \mu, \end{aligned}$$

from were we can build the normal equation N with the corresponding weight matrix **P**

$$\mathbf{N} = \begin{bmatrix} \mathbf{A} \\ \mathbf{I} \end{bmatrix}^T \begin{bmatrix} \mathbf{P_{ll}} & \mathbf{0} \\ \mathbf{0} & \mathbf{P_{oo}} \end{bmatrix} \begin{bmatrix} \mathbf{A} \\ \mathbf{I} \end{bmatrix} = [\mathbf{A}^T\mathbf{P}\mathbf{A} + \epsilon\ \mathbf{I}]$$

where

$$\epsilon = \frac{\sigma_{ll}^2}{\sigma_{oo}^2} \tag{7.6}$$

is called the regularization term and σ_{ll} and σ_{oo} are observation and a priori errors, respectively. P_{ll} and P_{oo} are weight factors of the observations and the a priori information, respectively.

7.2.2 Model description

The calculation of 3-dimensional distributions of water vapor is performed using GPS processed data. The distribution is modeled by spheric boxes where top and bottom surfaces are defined by horizontal ellipses. The vertical sides of the boxes are plane and conical in the longitude and latitude direction, respectively. The geometry of the elements within a layer is defined by equidistant spacing in both longitude and latitude direction. The height of the layers and the longitude and latitude spacing within each layer is defined by the user. The distances (Δs) within each box is calculated by ray-tracing through the elements of the model, based on a straight line from the antenna position to the satellite.

7.2.3 Observations

The observations (ρ) used for the tomographic inversion are double difference GPS residuals and Total Zenith Delay (TZD) estimates.

The TZDs and double difference residuals are processed using a ionospheric free linear combination with fixed station and satellite positions. Ambiguities that could not be solved in the pre-processing (real value ambiguities) are estimated, and the solved ambiguities (integer values) are then introduced as known. Hourly tropospheric parameters are estimated using the cosine mapping function.

In order to get observations in terms of double difference path delays, the TZD estimates are mapped back to the direction of the satellite with the same mapping function as used in the GPS processing. For each baseline, four slant delays are calculated and combined in order to form one double difference total delay. The final double difference observation is the sum of the re-constructed double difference total delay and the double difference residual. Wet delay double difference observations are generated by subtracting the double difference hydrostatic delay from the double difference total delay. The hydrostatic delay is modeled by the Saastamoinen model [Saastamoinen, 1973]. The double difference residuals are the sum of contributions from atmospheric inhomogeneities, mapping function errors, ionospheric effects from higher order terms not modeled by the ionosphere free linear combination, multipath effects and measurement noise.

The double difference observations were compared with modeled double difference total path delays. In Figure 7.3a results from one baseline are shown. The modeled delays were calculated with TZD estimates from the solution described in chapter 6, and a two layer model defined by the height of the two stations. Figure 7.3b shows the differences of observed - modeled double differences with respect to the elevation angle of one of the two observed satellites. An general increase of the scatter with decreasing elevation angle is visible.

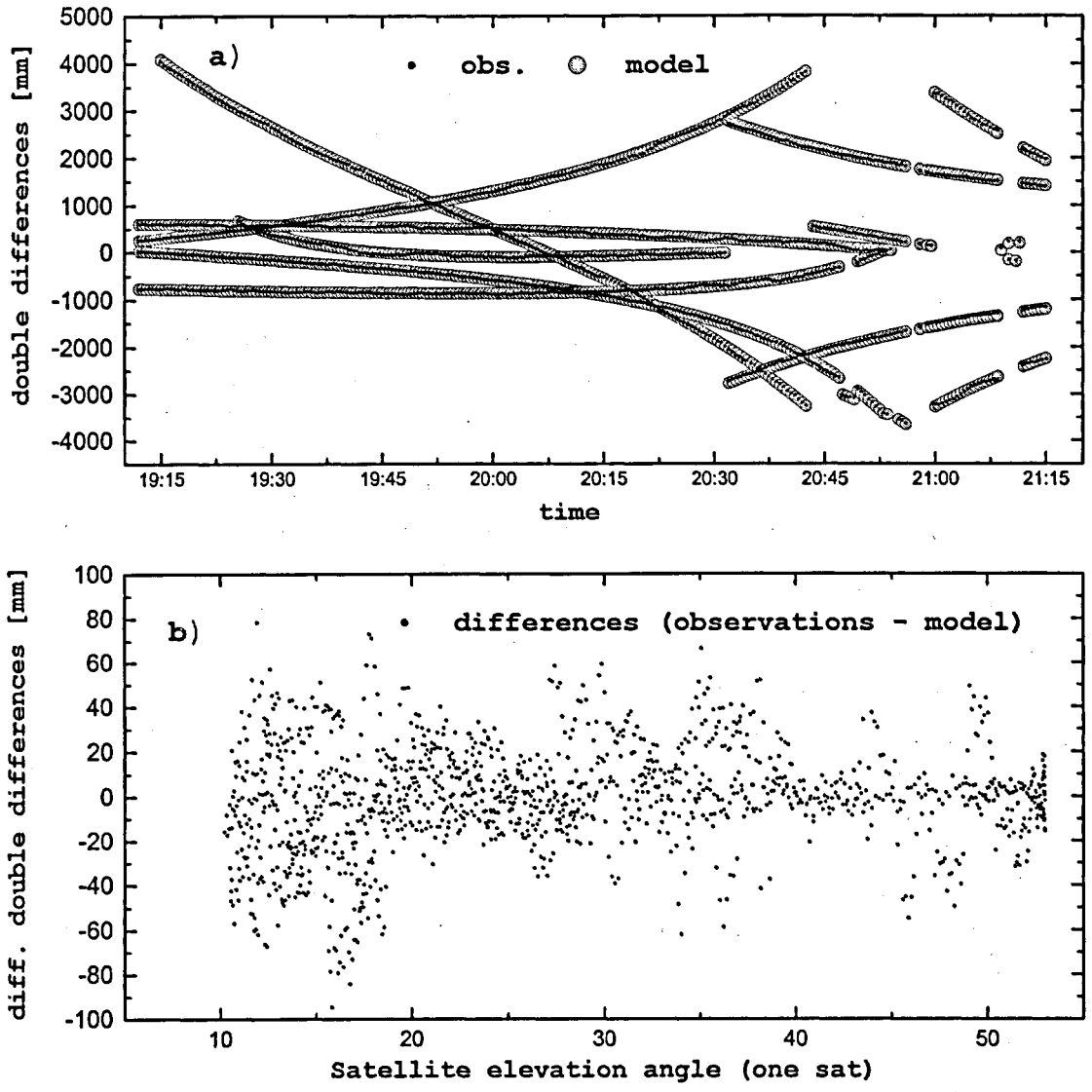

Figure 7.3: a) Modeled and observed double differences for a period of 2 hours from one baseline. The height difference between the two stations is about 3500 m. b) Differences of observed and modeled double differences with respect to the elevation angle of one of the two observed satellites. The standard deviation of the differences is 28.8 mm with a bias of 0.8 mm.

7.3 Results

The results of the tomographic analysis were calculated with GPS data from the Hawaiian Campaign. The tomograms display cross sections through the atmosphere above the experiment area along constant latitudes. The color scale represents the dimensionless wet refractivity as calculated by AWATOS. Two solutions were calculated for two different days. The radiosonde profiles from these two days are shown in Figure 7.4. The first profile (a) was launched at the station BILL in the western part of the network on February 19. It shows a relatively smooth decrease of water vapor pressure with height. From the second profile (b) a dramatic decrease of water vapor pressure at about 1700 meter is visible. This radiosonde was launched near the station PGF4 (see Figure 6.1 chapter 6) at the southern coast on February 26.

These two profiles are used for comparison with the tomographic solutions. Figure 7.5 and 7.7 display absolute estimates of wet refractivity. The results shown in Figure 7.6 and 7.8 are wet refractivity differences with respect to profile a) (Figure 7.4). The a priori information used in the tomographic processing was calculated by piecewise integration of profile a) within all layers as defined by the model. Vertically, the model is defined by 10 layers with an increasingly spacing from 0 to 15 km. Within each layer, 25 (5 by 5) equally distributed boxes define the model laterally. The top layer shown in the cross sections (between 4.1 to 5 km) represents the atmosphere from 4.1 up to 15 km.

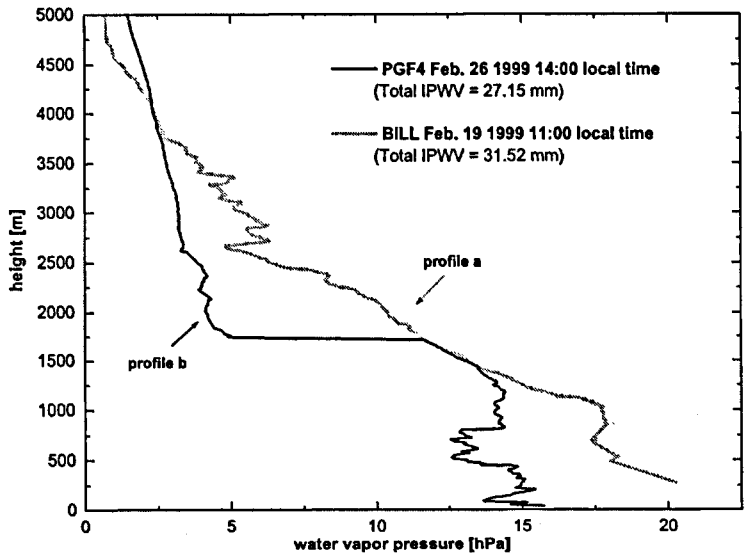

Figure 7.4: Two radiosonde profiles (a and b) of water vapor pressure launched on February 19, and 26, 1999. Profile a shows a smooth decrease of water vapor with height whereas profile b shows a rapid decrease at about 1.7 km.

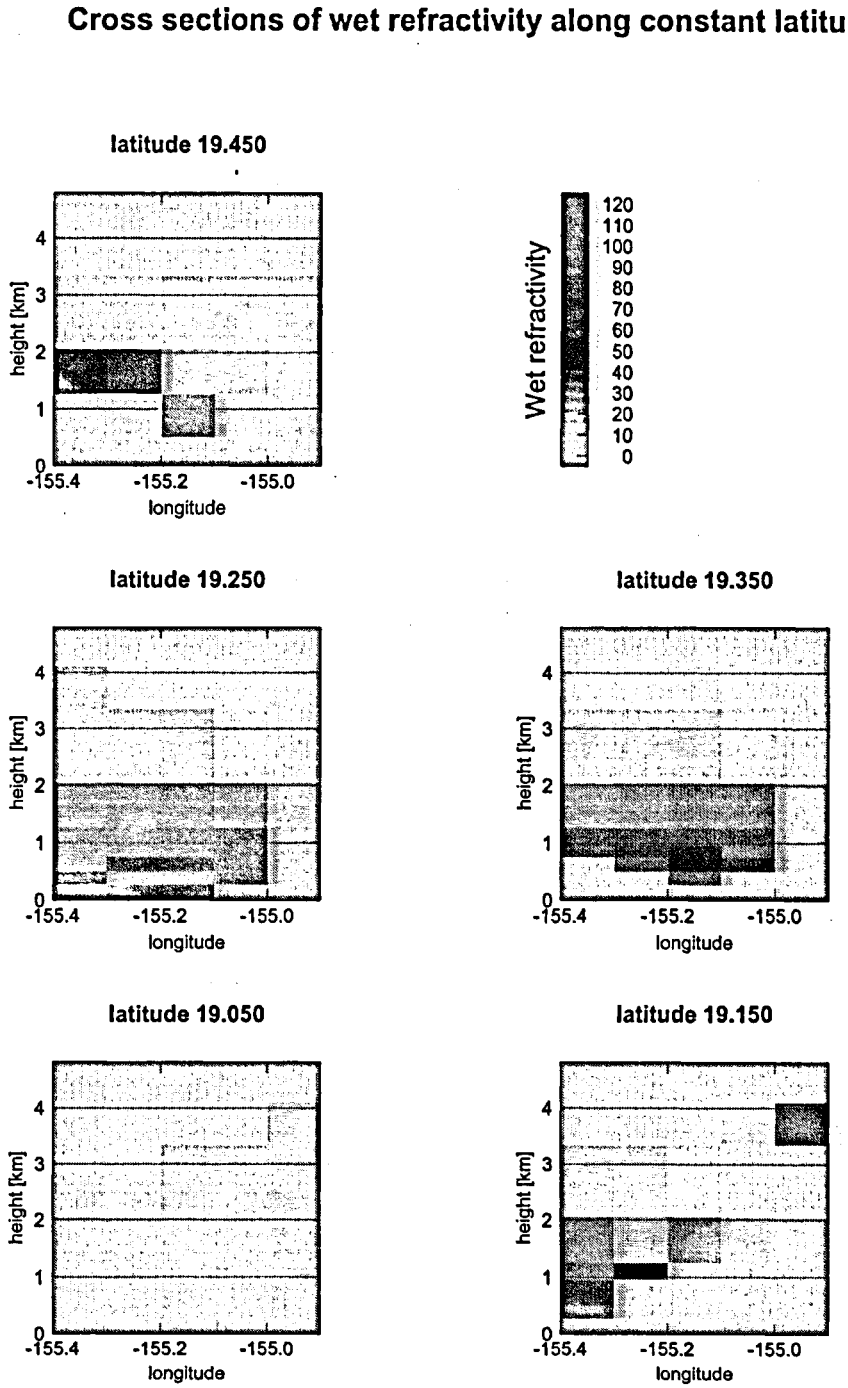

Figure 7.5: Absolute estimates of wet refractivity along constant latitudes on February 19 1999 11:00 local time. Gray shaded areas indicate that the boxes were not hit by a ray. Except for the cross section at latitude 19.05 all sections show higher refractivity to the west than to the east.

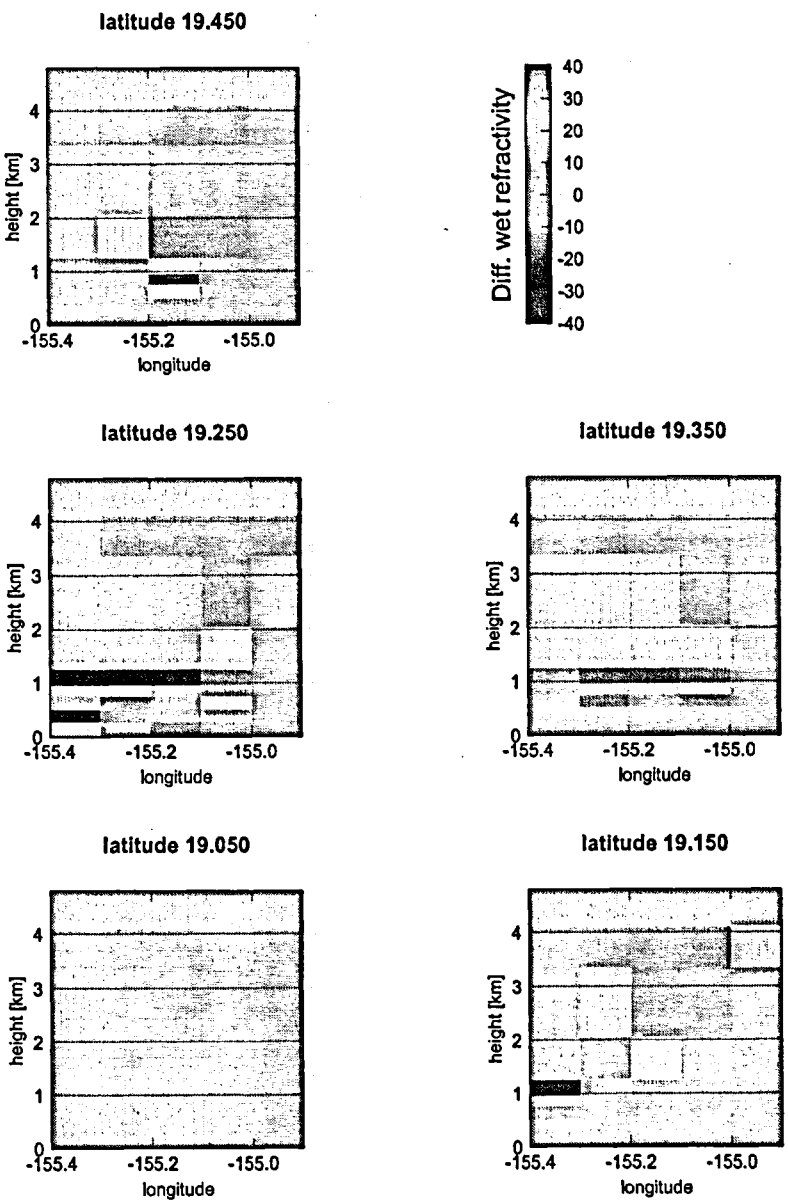

Figure 7.6: Wet refractivity differences between the tomographic solutions and a layered solution calculated with radiosonde measurements. Below 1250 meters strong positive and negative deviations from the radiosonde can be seen.

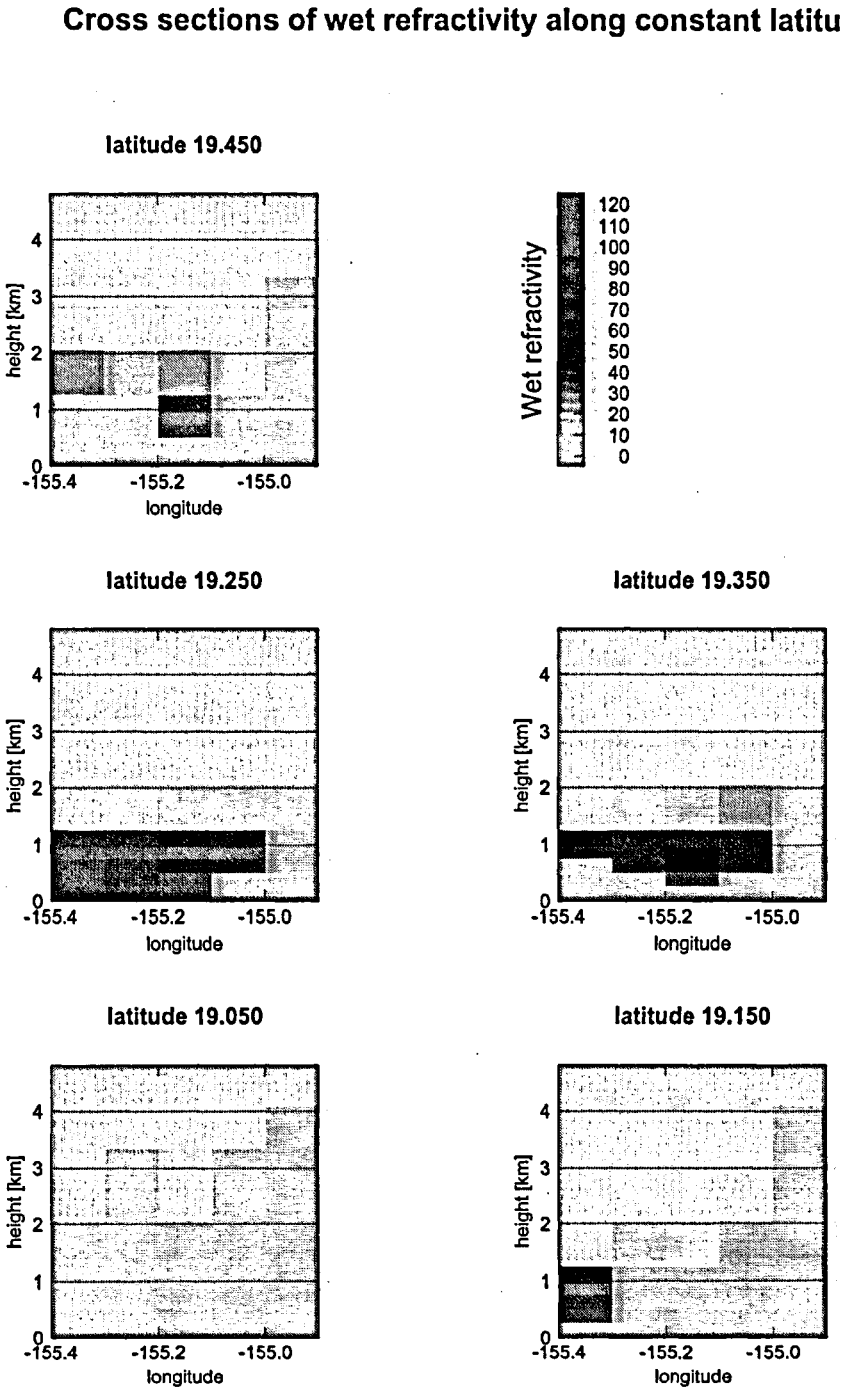

Figure 7.7: Absolute estimates of wet refractivity along constant latitudes on February 26 10:00 local time. The solution shows a rapid decrease of refractivity at a height of 1.25 km. The associated change in water vapor pressure is located at 1.7 km. The response of the tomographic model reproduces this inversion boundary at 1.25 km where the layer boundary is defined.

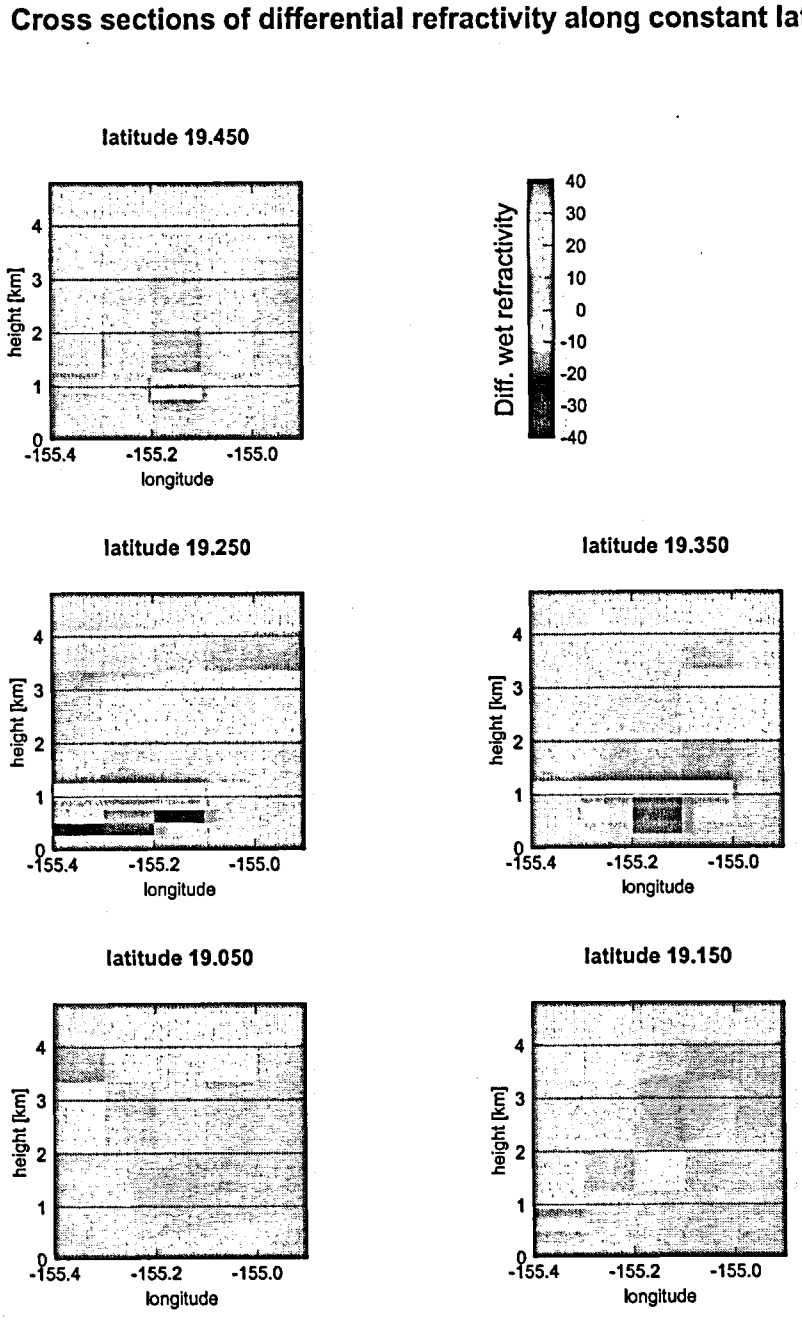

Figure 7.8: Wet refractivity differences between the tomographic solution shown in Figure 7.7 and the radiosonde launched five days earlier. Below 1250 meters the differences show in general negative values which are due to the higher water vapor content as measured by the radiosonde.

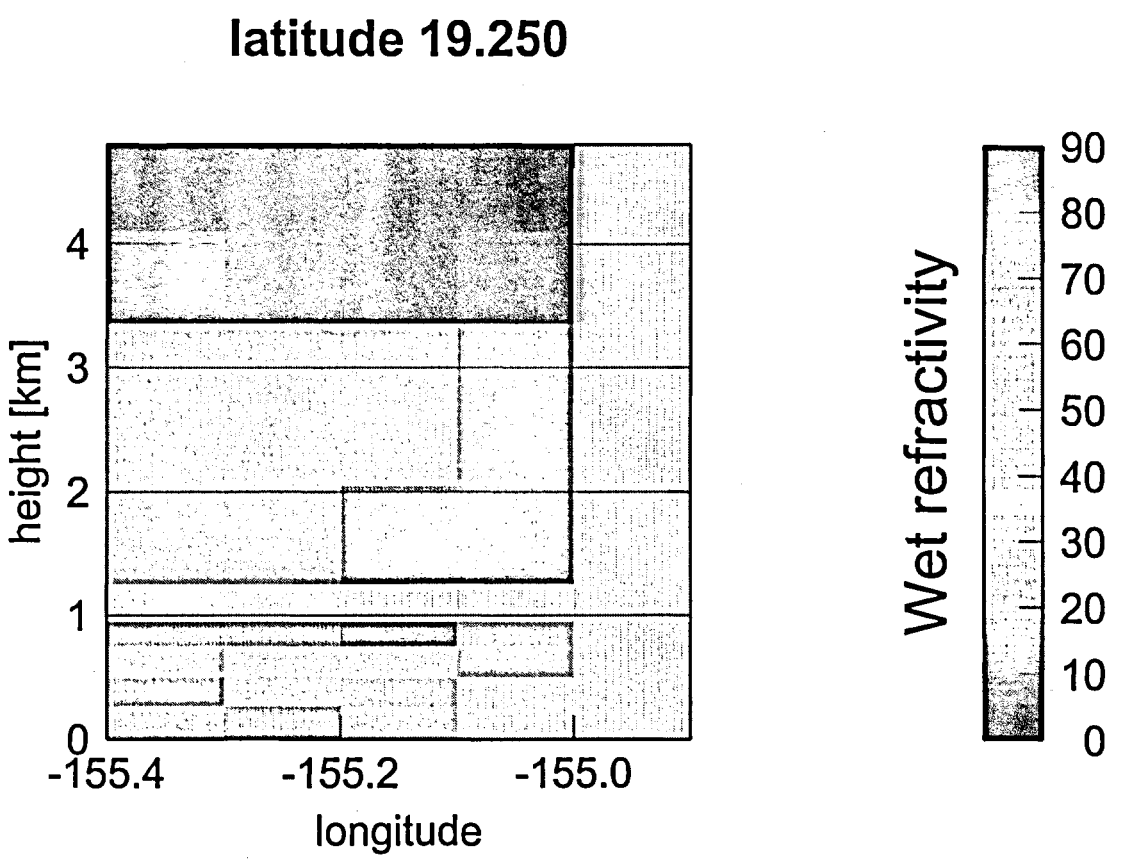

Figure 7.9: Wet refractivity cross section of the tomographic solution along latitude 19.25 calculated with GPS double difference observations.

7.3.1 Radiosonde Comparison

The radiosonde launched at the station PGF4 (Figure 7.4) was used for comparison with the tomographic solution. The radiosonde measurements of temperature and humidity was used to calculated the wet refractivity within heights defined by the box model. The a priori information was calculated using the radiosonde launched at the station BILL shown in Figure 7.4 (profile a). The results shown in Figure 7.10 show a good agreement. The decrease in wet refractivity between 500 and 1000 meters measured by the radiosonde is also detected by GPS. The largest deviation in wet refractivity is about 10 in the layer between 750 and 1000 m which corresponds to a difference in delay of 2.5 mm wet path delay.

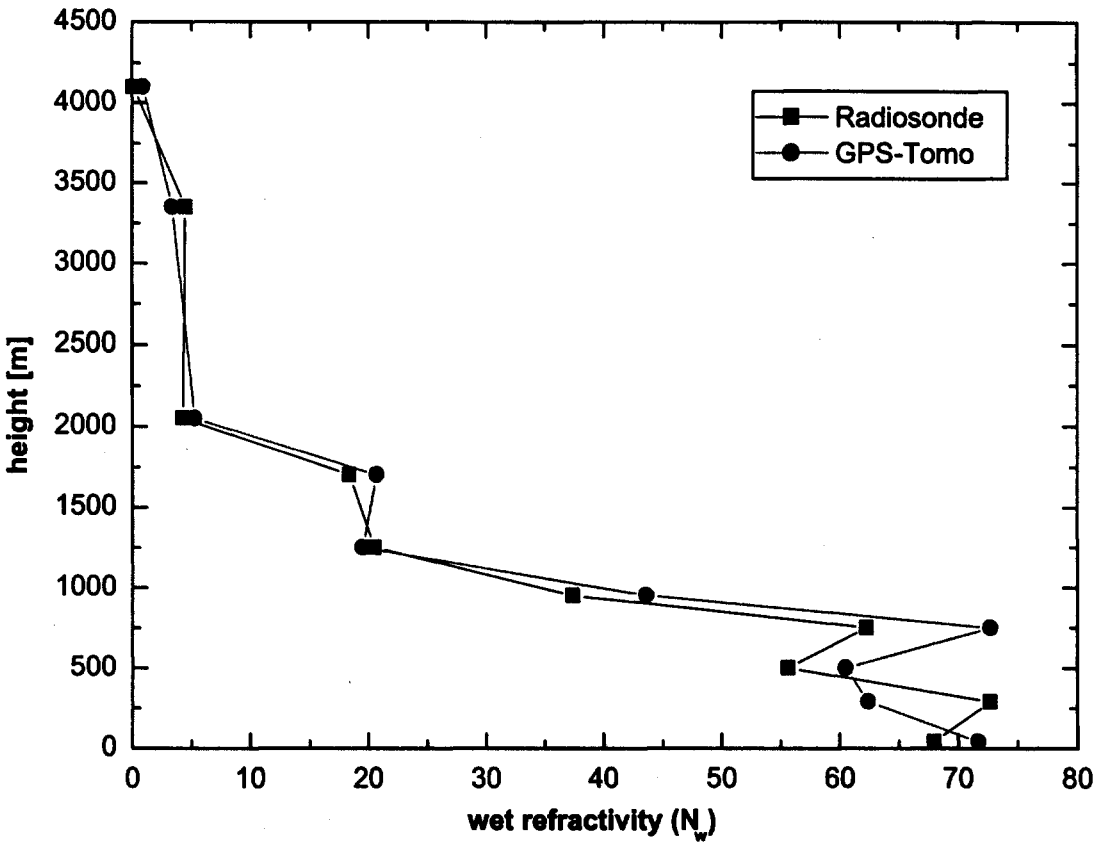

Figure 7.10: Wet refractivity profiles calculated from radiosonde measurements and tomography. The wet refractivity was calculated from radiosonde measurements of temperature and humidity within intervals defined by the box model.

8 Conclusions

The variety of applications based on the GPS system is steadily growing. They comprise classical positioning purposes as well as determination of earth rotation properties, mapping of the total electron content of the ionosphere, and determination of tropospheric water vapor content expressed in millimeter Integrated Precipital Water Vapor (IPWV). Because GPS is a multi-purpose technology several interests can easily be met without great effort. A GPS receiver set up for positioning purposes can at the same time be used for atmospheric water vapor monitoring by installing a barometer and a thermometer. In this work GPS receivers have been used as a remote sensing tool for determination of tropospheric water vapor utilized and validated by comparison with independent techniques such as water vapor radiometers (WVR), solar spectrometers, radiosondes, and modeling of tropospheric water vapor.

The modeling of tropospheric water vapor with the collocation method at ETH Zurich showed a good agreement with estimates from GPS and WVR at the 2 mm IPWV level. The main reason for this good agreement is the dense vertical distribution of the ANETZ network in Switzerland which provides meteorological measurements every 10 minutes from stations at about 400 to 3600 meters altitude. Because networks with such a distribution are rare, modeling in regions with smooth topography may therefore not be evaluated with a comparable accuracy as shown here.

One problem of such models is the fact that in the absence of radiosonde data the water vapor content tends to be overestimated due to a lack of vertical profile information in the data. By constraining the water vapor pressure at high altitudes to zero, the overestimates of water vapor could be reduced. In contrast the Saastamoinen solution underestimates the water vapor content when an inversion layer is present. The lower water vapor pressure measured at ground in combination with a standard profile of water vapor distribution misses the associated increase in water vapor pressure.

The overall accuracy of the modeling examples shown is lower than those of the GPS and WVR estimates. The intercomparison of the three approaches showed significant deviations of the model solutions from the two remote sensing techniques, which mutually agree within their limits of accuracy. These discrepancies are pronounced during periods with short time water vapor fluctuations detected by GPS and WVR but not by the model. A possible explanation for this shortcoming is an inadequate modeling of the upper local humidity profile interpolated from distant alpine

high-altitude stations. The upper air profiles at the station Zurich are interpolated from distant alpine stations and radiosondes thus transferring local phenomena to non-alpine sites. Improvements of the model parameters by introducing a piecewise fitting of the temperature lapse rate to account for inversions at low altitudes and the almost constant temperature of the stratosphere might improve the overall results of the modeling. The accuracy of atmospheric modeling can be improved by introducing GPS propagation delay estimates in forecast models. On the other hand such improved models could be used as refraction corrections for GPS positioning purposes.

Apart from the intercomparison of different techniques, an extensive investigation of the radiometric technique has been carried out, comparing several radiometers in Europe. The WVRs have been operated in co-location in order to assess the absolute accuracy of the technique and instrumental biases between the individual systems. For this purpose the portable WVRs of ETH acted as calibration link between the ASTRID WVR at Onsala Space Observatory, Sweden and the WVRs operated by the Bundesamt für Kartographie und Geodäsie in Wettzell, Germany. The comparison of the ETH-Red WVR with ASTRID showed good agreement between measurements of the two instruments. The standard deviation of the differences reveals 0.68 mm, with a constant offset of 1.84 mm IPWV. Since the stationary Swedish WVR has the longest history of WVR recordings and validation with other techniques, it was selected as a reference instrument for the other instruments. The biases of the ETH and BKG-WVRs were determined as calibration offsets. This procedure is based on the assumption that the instrumental offset between ASTRID and ETH WVRs are constant over 10 months. Experiences with the two ETH radiometers have shown that the offset of 0.3 mm IPWV between the instruments has been stable for more than 6 years. By applying the ASTRID calibration offsets to the ETH and BKG WVRs the absolute agreements with GPS estimated IPWV was improved.

The portable ETH WVRs were compared with GPS estimates at the four European stations Onsala (Sweden), Madrid (Spain) Wettzell (Germany) and Zurich (Switzerland) and on Hawaii (USA). The results from these comparisons show in general good agreement at the 1 - 2 mm IPWV level. There are, however, significant temporal disagreements that are not fully explained.

The results from the one year GPS-WVR comparison at the ETH showed a clear seasonal dependency on the GPS - WVR differences. The higher scatter of the differences during summer and autumn months correlate well with the higher fluctuations of water vapor during these months. The results from the GPS - WVR comparisons in Spain (winter), Sweden and Wettzell (summer) confirm this behavior.

Such seasonal differences are less pronounced on Hawaii where the difference in monthly maximum and minimum temperatures is about 6°C. However during the campaign, daily fluctuations of water vapor up to 20 mm IPWV were observed. The intercomparison of GPS, WVR and modeling showed systematic errors of the GPS estimates. Preliminary results from solar spectrometer (SSM) measurements seem to confirm the results obtained with the WVR. The relative strong dependency

of the tropospheric GPS estimates on the elevation cut-off angle implies that the Hopfield mapping function may not be adequate for this climate region.

The GPS - radiosonde comparison showed that the offset was time dependent and highly correlated with the height and intensity of the temperature inversion layer. The intensity of the inversion layer is highly correlated with a rapid decrease of the water vapor content. Such abnormal distributions of water vapor are not modeled by mapping functions and are therefore an error source. The comparison of GPS estimates with modeling showed the same time dependency of the offsets as was seen in the GPS - radiosonde comparison. The offset between GPS and modeling also showed a strong dependency with height during the period with temperature inversion.

To test the impact of the mapping function a re-processing of the GPS data with the new version 4.2 of the Bernese Software, offering the possibility to process GPS data with other mapping functions, should be made.

With the point positioning method the impact of the network strategy on water vapor estimates could be investigated.

In meteorological GPS networks, independent techniques like WVR and/or SSM are essential to calibrate the IPWV estimates (especially for real-time applications).

Regarding real-time applications of GPS meteorology, the impact of predicted CODE orbits on water vapor estimates were investigated. The errors of predicted orbits are mainly in the along-track direction. The estimation of one single orbit parameter per satellite, to account for these along track errors, improved the real-time GPS estimates significantly. The impact of this strategy is more pronounced for the two day orbit predictions than for the one day orbit predictions. In our study, the best estimation strategy using the one day predicted orbits yielded a standard deviation from the WVR curve that was about 1.4 times higher than the solution using final precise IGS orbits. Since the release of the one day predicted orbit product is delayed by about 12 hours one has to rely on a combination of one and two day predictions to achieve optimum results for real time GPS applications. The obtainable precision in 1996 was estimated to be about 2-3 mm in real-time, less than a factor of 2 worse than the results achieved with final precise IGS orbits. At present, GPS data from several global stations are available as one hour observation files. This should bring the agreement near to the 2 mm level or even below provided orbit predictions are done more frequently (e.g. 2 times per day with 12 hours extrapolation). With the point positioning method no distant stations are required for absolute tropospheric estimates. However, for real-time applications predicted satellite clocks must be available. Such clock predictions with their corresponding errors may therefore further degrade the accuracy.

The resolution of three-dimensional water vapor distributions by means of a tomographic approach as discussed in chapter 7 showed the feasibility of the method. The preliminary results revealed the presence of horizontal inhomogeneities. The comparison of wet refractivity between the radiosonde and the tomographic solu-

tion indicate that modeling of the atmosphere above a receiver network improves the solution compared to a stratified atmosphere defined by the heights of the GPS antennas. Although the tomographic approach provided good results this method is not yet fully exploited. Further improvements of the software such as the implementation of more sophisticated mapping functions and elevation dependent weighting of the observations should be investigated. In this respect the application of GPS tomography might be feasible even in networks with sparsely distributed GPS receivers.

Bibliography

Alber, C., Ware, R., Rocken, C., and Solheim, F. (1997). GPS surveying with 1 mm precision using corrections for atmospheric slant path delay. *Geophysical Research letters*, 24(15):1859 – 1862.

Askne, J. and Nordius, H. (1987). Estimation of tropospheric delay for microwaves from surface weather data. *Radio Sci.*, 22:379–386.

Askne, J. and Westwater, E. R. (1986). A review of ground-based remote sensing of temperature and moisture by pasive microwave radiometers. *IEEE Trans. on Geosci. and Remote Sensing*, GE-34(3).

Baker, H. (1998). *GPS Water Vapour Estimations For Meteorological Applications.* PhD thesis, University of Nottingham, Institute of Engineering Surveying and Space Geodesy.

Becker, M., Zerbini, S., Baker, T., Bürki, B., Galanis, J., Garate, J., Georgiev, I., Kotzev, V., Lobazov, V., Marson, I., Negusini, M., Richter, B., Veis, G., and Yuzefovich, P. (2000). Assesment of Height Variations by GPS at the Mediterranean and Black Sea Coast Tide Gauges from the SELF Project. *Submitted to Global and Planetary Change.*

Bevis, M., Businger, S., Herring, T., Rocken, C., Anthes, R., and Ware, R. (1992). GPS Meteorology: Remote Sensing of Atmospheric Water Vapor Using the Global Positioning System. *Geophys. Res. Lett.*, 97:15,787–15,801.

Bevis, M., Chriswell, S., Businger, S., Herring, T., and Bock, Y. (1996). Estimating wet delays using numerical weather analyses and predictions. *Radio science*, 31:477–487.

Bürki, B., Cocard, M., Geiger, A., Gyger, R., and Kahle, H.-G. (1992). Development of a portable dual frequency microwave water vapor radiometer for geodetic applications. *in Refraction of Transatmospheric Signals in Geodesy, Proceedings of the Symposium, Publ.*, pages 129–133.

Bürki, B., Sierk, B., Kruse, L., Kahle, H.-G., Lisowsky, M., Bevis, M., and Dodson, A. (1999). Field experiment for an integrated study of tropospheric water vapor at Hawaii. *Geophysical Research Abstr*, page 230.

Calais, E. (1999). Continuous GPS measurements across the Western Alps, 1996-1998. *Geophysical J. Int*, 138:221–230.

Chandrasekhar, S. (1960). *Radiative Transfer.* Dover Publications, Inc., New York.

Cruz-Pol, S., Ruf, C., and Keihm, S. (1998). Improved 20- to 32GHz atmospheric absorption model. *Radio Sci.*, 33:1319–1333.

Davis, J. L., Hering, T. A., Shapiro, I. I., Rogers, A. E. E., and Elgered, G. (1985). Geodesy by radio interferometry: Effects of atmospheric modeling errors on estimates of baseline length. *Radio Sci., Vol. 20 No. 6*, pages 1593–1607.

Decker, M., Westwater, E., and Guiraud, F. (1978). Experimental evaluation of ground-based microwave radiometric sensing of atmospheric temperature and water vapor profiles. *Journal of Appl. Meteorology*, 17(12):1788 – 1795.

Dodson, A. and Baker, H. (1998a). Accuracy of Orbits for GPS Atmospheric Water Vapour Estimation. *Phys. Chem. Earth*, 23:119–124.

Dodson, A. and Baker, H. (1998b). Interim progress report on the wavefront project. *European Commission contract no ENV4-CT96-0301.*

Duan, J., Bevis, M., Fang, P., Bock, Y., Chiswell, S., Businger, S., Rocken, C., Solheim, F., Hove, T. V., Ware, R., Mc-Clusky, S., Hering, T., and King, R. (1996). GPS Meteorology: Direct Estimation of the Absolute Value of Precipitable Water. *Journal of Appl Meteor. Volume 97*, pages 830–838.

Eckert, V., Cocard, M., and Geiger, A. (1992). Collocation of Meteorological Data for Interpretation and Estimation of Tropospheric Pathdelays. Technical Report 194, Institute of Geodesy and Photogrammetry, ETHZ, Zürich.

Edmarson, T. and Derks, H. (1999). On the relation between the wet delay and the precipitable water in the european atmospher. *EOS, Trans. AGU*, 173.

Elgered, G. (1993). Tropospheric radio path delay from ground-based microwave radiometry. *Atmospheric Remote Sensing by Microwave Radiometry*, pages 215–258.

Elosegui, P., Rius, A., Davis, J., Ruffini, G., Keim, S., Bürki, B., and Kruse, L. (1998). An experiment for estimation of the spatial and temporal variations of water vapor using gps data. *Phys. Chem. Earth.*, 23:125–130.

Gassner, M. (1990). Vergleich von Temperatur und Taupunkt in der freien Atmosphäre im Gebirge mit den ANETZ Stationswerten und der Sondierung von Payerne. Diploma Thesis, Institute of Atmospheric Research LAPETH, ETHZ, Zürich.

Geiger, A. (1987). Einfluss richtungsabhängiger Fehler bei Satellitenmessungen. Technical Report 130, Institute of Geodesy and Photogrammetry, ETHZ, Zürich.

Goff, J. (1965). Saturation pressure of water on the new kelvin scale. *Humidity and Moisture*, 3:289–292.

Herring, T. (1992). Modelling Atmospheric Delays in the Analysis of Space Geodetic Data. In *Refraction of Transatmospheric Signals in Geodesy, Proceedings of the Symposium*, volume Publ. Geod. 36, pages 157–164.

Hirter, H. (1998). *Mehrdimensionale Interpolation von Meteorologischen Feldern zur Berechning der Brechungsbedingungen in der Geodäsie.* PhD thesis, ETH Zürich. No. 11578.

Hopfield, H. (1969). Two-quartic tropospheric tropospheric refractivity profile for correcting satellite data. *Journal of Geophysical Research*, 74(18):4487 – 4499.

Jarlemark, P. (1997). *Analysis of Temporal and Spatial Variations in Atmospheric Water Vapor Using Microwave Radiometry.* PhD thesis, School of Electrical and Computer Engineering Chalmers University of Technology. Technical Report 308.

Johansson, J., Elgered, G., and Davis, J. L. (1993). Wet Path Delay Algorithms for Use with Microwave Radiometer Data. *Contributions of Space Geodesy to Geodynamics Technology*, 25:81–98.

Kahle, H.-G., Cocard, M., Peter, Y., Geiger, A., Reilinger, R., McClusky, S., King, R. W., Barka, A., and Veis, G. (1999). GPS derived strain field in the Eastern Mediterranenan and Near East. *JGR.* submitted.

Kouba, J. and Mireault, Y. (1998). Analysis coordinator report. *IGS 1997 Technical Reports*, pages 23–69.

Kruse, L., Sierk, B., Springer, T., and Cocard, M. (1999). Gps-meteorology: Impact of predicted orbits on precipitable water estimates. *Geophys. Res. Lett.*, 26:2045–2048.

Kuo, Y.-H., Zou, X., and Guo, Y.-R. (1996). Variational assimilation of precipitable water using a nonhydrostatic mesoscale adjoint model. *Mon. Weather Rev*, 124:122–147.

Liebe, H. (1985). An update model for millimeter wave propagation in moist air. *Radio Sci.*, 20:1069–1089.

Liebe, H. (1987). A Contribution to Modeling Atmospheric Millimeter-wave Properties. *Frequenz*, 41:31–36.

Liebe, H. J. (1992). Atmospheric Spectral Properties Between 10 and 350 GHz: New Laboratory Measurements and Models. *proc. Specialist Meeting on Microwave Radiometry and Remote Sensing Applications.*

Lisowski, M. (1999). PhD thesis. Pers. com.

Magnus, G. (1844). Versuche über die Spannkräfte des Wasserdampfs. *Ann. Phys. Chem.*, 61:225–247.

McClusky, S., Balassanian, S., Barka, A., Demir, C., Georgiev, I., Hamburger, M., Hurst, K., Kahle, H.-G., Kastens, K., Kekelidze, G., King, R. W., Kotzev, V., Lenk, O., Mahmoud, S., Mishin, A., Nadariya, M., Ouzoun is, A., Paradissis, D., Peter, Y., Prilepin, M., Reilinger, R., Sanli, I., Seeger, H., Tealeb, A., Tokzoz, M., and Veis, G. (2000). GPS constraints on crustal movements and deformations in the Eastern Mediterranean (1988-1997): Implications for plate dynamics. *JGR.* In press.

Moritz, H. (1973). Least-Square Collocation. DKG, Bayrische Akademie der Wissenschaften. Reihe AA: Theoretische Geodäsie, Heft Nr. 75, p 91.

Moritz, H. (1980). Advanced Physical Geodesy. H. Wichmann Verlag, Karlsruhe, p 500.

Owens, J. (1967). Optical refractive index of air: Dependence on pressure, temperature, and composition. *App. Opt.*, 6:51–58.

Penna, N. (1997). *Monitoring Land Movement at UK Gauge sites using GPS.* PhD thesis, University of Nottingham.

Richner, H., Joss, J., and Ruppert, P. (1996). A Water Hypsometer Utilizing High-Precision Termocouples, journal = Journal of Atmospheric and Oceanic Technology. 13(1):175 – 182.

Richner, H. and Phillips, P. (1984). A comparison of temperature from mountaintops and the free atmosphere - thier diurnal variation and mean difference. *Monthly Weather Review*, 112(7):1328 – 1340.

Richner, H. and Viatte, P. (1995). The hydrostatic equation in the evaluation algorithm for radiosonde data. *Journal of Atmospheric and Ocean Tec.*, 12:649 – 656.

R.McIlven (1989). *Basic Meteorology, a physical outline.* Van Nostrand Reinhold, ISBN 0 442 31769 7, UK.

Rocken, C., Hove, R., Johnson, J., Solheim, F., Ware, R., Bevis, M., Businger, S., and Chiswell, S. (1995). GPS Storm –GPS Sensing of Atmospheric Water Vapor for Meteorology. *Journal of Oceanic and Atmospheric Technology*, 12:468–478.

Rocken, C., Hove, R., and Ware, R. (1997). Near real-time gps sensing of atmospheric water vapor. *Geophys. Res. Lett.*, 24:3221–3324.

Rothacher, M. (1999). *Collection, Processing and Archiving of a European IGS Network of GPS IWV Estimates.* Final report on the European WAVEFRONT Project.

Rothacher, M. and Mervart, L. (1996). *The Bernese GPS software version 4.0 user manual.* report, Astron. Inst., Univ. of Bern, Bern Switzerland.

Ruffini, G., Kruse, L. P., Rius, A., Bürki, B., and Cucurull, L. (1998). Estimation of Tropospheric Zenith Delay and Gradients over the Madrid Area Using GPS and WVR data. *Submitted to Geophysics. Res. Lett.*

Saastamoinen, J. (1973). Contributions to the Theory of Atmospheric Refraction / Introduction to Practical Computation of Astronomical Refraction. Bulletin géod ésique Nrs 105, 106, 107, pp.50.

Santerre, R., Forgues, I., Mendes, V., and Langley, R. (1995). Comparison of Tropospheric Mapping Functions: Their Effects on Station Coordinates. *IUGG XXI General Assembly Boulder Colorado.*

Schaer, S. (1999). *Mapping and Predicting the Earth's Ionosphere Using the Global Positioning System.* PhD thesis, University of Berne, Astronomical Institute University of Berne.

Schmid, H. (1977). Ein allgemeiner Ausgleichungs-Algorithmus für die numerische Auswertung in der Photogrammetrie. IGP, Mitteilung Nr. 22, ETH Zürich, p45.

Seeber, G. (1993). Satellite Geodesy: Foundations, Methods and Applications. de Gruyter, ISBN 3-11-012753-9.

Sierk, B. (2000). *Solar spectrometry for determination of tropospheric water vapor.* PhD thesis, ETH Zürich. Pers. com.

Skoog, B., Askne, J., and Elgered, G. (1982). Experimental determination of water vapor profiles from ground-based radiometer measurements at 21.0 and 31.4ghz. *Journal of Appl. Meteorology*, 21:394 – 400.

Smith, E. and Weintraub, S. (1954). The constants in the equation for atmospheric refractive index at radio frequencies. *Proc. Inst. Radio Engineers*, 41:1035.

Solheim, F., Godwin, J., and Ware, R. (1998). Passive ground-based remote sensing of atmospheric temperature, water vapor, and cloud liquid water profiles by a frequency synthesized microwave radiometer. *Meteorologische Zeitschrift*, (7):370–376.

Solheim, F. and Keihm, S. (1994). New designs for portable microwave temperature profilers and water vapor profilers. *Proceedings of the Specialist Meeting on Microwave Radiometry and Remote Sensing of the Environment, Rome Italy.*

Springer, T. (1999). *Modeling and Validating Orbits and Clocks Using the Global Positioning System.* PhD thesis, University of Berne, Astronomical Institute University of Berne.

Staelin, D. (1966). Measurements and Interpretation of the Microwave Spectrum og Terrestrial Atmosphere near 1-Centimeter Wavelength. *Journal of Geophysical Research*, 71:2875–2881.

Teunissen, P. and Kleusberg, A. (1998). GPS for Geodesy. Springer, ISBN 3-540-63661-7.

Thayer, G. (1974). An improved equation for the radio refractive index of air. *Radio Sci.*, 9:803–807.

Tschirren, J. (1989). Räpresentivität von Bodenmessstationen (ANETZ) für die Bestimmung des Wasserdampfdrucks in der freien Atmosphäre. Diploma Thesis, Institute of Atmospheric Research LAPETH, ETH, Zürich. pp 78.

Vleck, J. V. and Huber, D. (1974). Absorption, emission and linebreadths: A semihistorical perspective. *Reviews of Modern Physics*, 49(4):939 – 959.

Waters, J. (1976). Absorbtion and Emission by Atmospheric Gases. *Methods of Experimental Physics*, 12B:142–176.

WAVEFRONT (1999). Final report on the wavefront project. *European Commission contract no ENV4-CT96-0301.*

Westwater, E., Snider, J., and Carlson, A. (1975). Experimental determination of temperature profiles by ground-based microwave radiometry. *Journal of Appl. Meteorology*, 14(4):524 – 539.

Wiget, A., Brockmann, E., Schneider, D., Signer, T., and Geiger, A. (1999). The First Re-observation of the Swiss GPS Control Network. *IUGG. Abstracts*, A:410.

Wu, S. (1979). Optimum Frequencies of a passive Microwave Radiometer for Tropospheric Path-Length Correction. *IEEE Trans. Ant and Prop.*, AP-27,No. 2:233 – 239.

Yuan, L., Anthes, R., Ware, R., Rocken, C., Bonner, W., Bevis, M., and Businger, S. (1993). Sensing Climate Change Using the Global Positioning System. *Journal of Geophysical Research*, 98:14925–14937.

9 Appendix

9.1 WVR Stochastic Error estimates

The stochastic error estimate of the path delay is estimated by calculating the partial derivatives of Equation 9.1, 9.2, and 9.3 with respect to the variables listed in Table 9.1

$$\begin{aligned}\Delta L_w = c_{eff}\Big[1 + c_1(P_o - \overline{P}_o) + c_2(T_{o,max} - \overline{T}_{o,max}) \\ + c_3(X - \overline{X})\Big] \cdot (1 + 6 \cdot 10^{-5} T_{o,max})\, X\end{aligned} \tag{9.1}$$

where

$$X = \left[\left(\frac{f_2}{f_1}\right)^2 T'_{s,f_1} - T'_{s,f_2} - T_{bg+ox}\right] \tag{9.2}$$

is the linear combination of the two brightness temperatures and the combined background and oxygen temperatures. The combined model derived for the cosmic background and the oxygen contribution Jarlemark [1997] is

$$T_{bg,ox} = \left[\left(\frac{f_2}{f_1}\right)^2 - 1\right] T_{bg} + \left(\frac{f_2}{f_1}\right)^2 T_{ox.f_1} - T_{ox.f_2} \tag{9.3}$$

An example of the total error contribution is calculated below. The estimated standard deviation of the following variables are:

Inserting the absolute quantities in the partial derivatives multiplying by the square of the standard deviation yield the following variance;

$P = 1013.0$	$\Delta P = \pm\ 1.0$	[hPa]: abs. pressure and measurement error
$\overline{P} = 994.9$	$\Delta\overline{P} = \pm\ 10.95$	[hPa]: year mean and Stdv. of pressure
$T = 288.2$	$\Delta T = \pm\ 0.5$	[K]: temperature and measurement error
$\overline{T} = 283.6$	$\Delta\overline{T} = \pm\ 7.07$	[K]: year mean and Stdv. of Temperature
$X = 27.31$	$\Delta\overline{X} = \pm\ 11$	[K]: year mean and Stdv. of X
$C_{eff} = 0.307$	$\Delta C_{eff} = \pm$ 2.1404e-4	[cm/K]: inversion coefficient
$c_1 =$ -0.937e-4	$\Delta c_1 = \pm$1.7983e-5	[1/hPa]: retrieval coefficient (pressure term)
$c_2 =$ -0.111e-2	$\Delta c_2 = \pm$3.2264e-5	[K]: retrieval coefficient (temperature term)
$c_3 =$ 0.277e-3	$\Delta c_3 = \pm$1.50841e-5	[K]: retrieval coefficient (X term)
$T_{s,f1} = 98.082$	$\Delta T_{s,f1} = \pm$1.0 Kelvin	[K]: brightness temperature 23.8 GHz
$T_{s,f1} = 108.937$	$\Delta T_{s,f2} = \pm$1.0 Kelvin	[K]: brightness temperature 31.5 GHz

Table 9.1:

$$\left[\frac{d(\Delta L_w)}{d(T_{s,f1})}\right]^2 < \Delta T_{s,f1} >^2 = 3.0302e-01 \approx 63.51\%$$
$$\left[\frac{d(\Delta L_w)}{d(T_{s,f2})}\right]^2 < \Delta T_{s,f2} >^2 = 9.8749e-02 \approx 20.70\%$$
$$\left[\frac{d(\Delta L_w)}{d(T)}\right]^2 < \Delta X >^2 = 3.9110e-02 \approx 8.20\%$$
$$\left[\frac{d(\Delta L_w)}{d(\overline{T})}\right]^2 < \Delta\overline{T} >^2 = 2.3680e-02 \approx 4.96\%$$
$$\left[\frac{d(\Delta L_w)}{d(T_{bg+ox})}\right]^2 < \Delta T_{bg+ox} >^2 = 8.3134e-03 \approx 1.74\%$$
$$\left[\frac{d(\Delta L_w)}{d(\overline{X})}\right]^2 < \Delta\overline{X} >^2 = 3.5534e-03 \approx 0.74\%$$
$$\left[\frac{d(\Delta L_w)}{d(c_3)}\right]^2 < \Delta c_3 >^2 = 5.7360e-04 \approx 0.12\%$$
$$\left[\frac{d(\Delta L_w)}{d(\overline{T})}\right]^2 < \Delta\overline{P} >^2 = 4.0246e-04 \approx 0.08\%$$
$$\left[\frac{d(\Delta L_w)}{d(T)}\right]^2 < \Delta T >^2 = 1.1844e-04 \approx 0.02\%$$
$$\left[\frac{d(\Delta L_w)}{d(c_{eff})}\right]^2 < \Delta c_{eff} >^2 = 8.8298e-05 \approx 0.02\%$$
$$\left[\frac{d(\Delta L_w)}{d(c_2)}\right]^2 < \Delta c_2 >^2 = 4.2555e-05 \approx 0.01\%$$
$$\left[\frac{d(\Delta L_w)}{d(c_1)}\right]^2 < \Delta c_1 >^2 = 9.3321e-06 \approx 0.00\%$$
$$\left[\frac{d(\Delta L_w)}{d(T)}\right]^2 < \Delta P >^2 = 3.3566e-06 \approx 0.00\%$$

The standard deviation or absolute error from this example is 0.63 cm zenith wet path delay The algorithm error for noise free radiometer measurements (e.g $\Delta T_{s,1} = \Delta T_{s,2} = 0$) is 0.19 cm zenith wet path delay. The most important error contributions are those related to the brightness temperature measurements of the WVR. In operational use brightness temperature measurements are carried out at different elevation angles to calibrate the hot load reference temperature of the instrument by the method of tipping curve. System noise contributions from the microwave and electronic components are mitigated into the hot load correction pa-

rameter. It is therefore difficult to isolate the noise of the antenna measurements. In addition, contributions from water vapor distributions not modeled by the mapping function (e.g in one azimuthal direction) are included. The noise of the calibrated hot load temperature may therefore be more representative for the noise of the radiometer than the noise of the antennas alone. The accuracy of the instrument can be calculated by determining the noise level of the calibrated hot load temperatures using these as representatives for the antenna temperature noise.

9.2 Radiosonde Profiles

The following 17 radiosonde profiles were launched on the Big Island of Hawaii from February 17. to 28. Temperature and water vapor pressure are displayed in grey and black, respectively. For each sonde the wet path delay as a function of height was calculated and displayed together with wet path delays from the GPS stations.

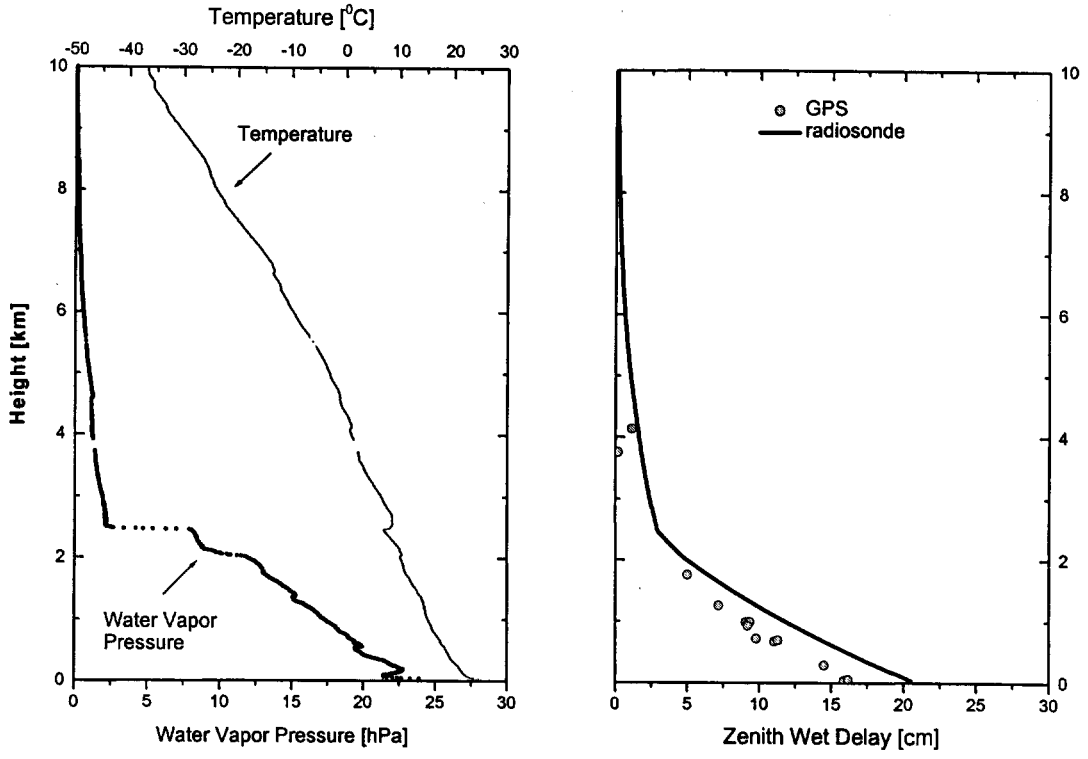

Station: PGF4, Sonde: 03:00 UT, Feb. 17.

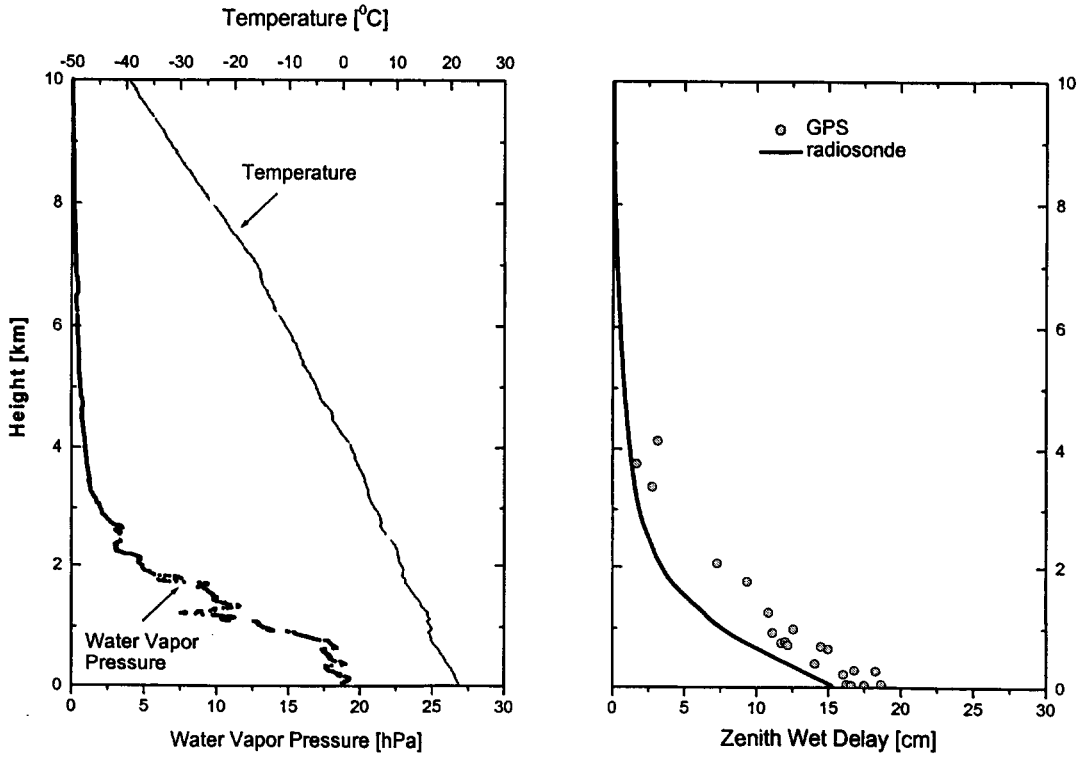

Station: PGF4, Sonde: 14:00 UT, Feb. 17.

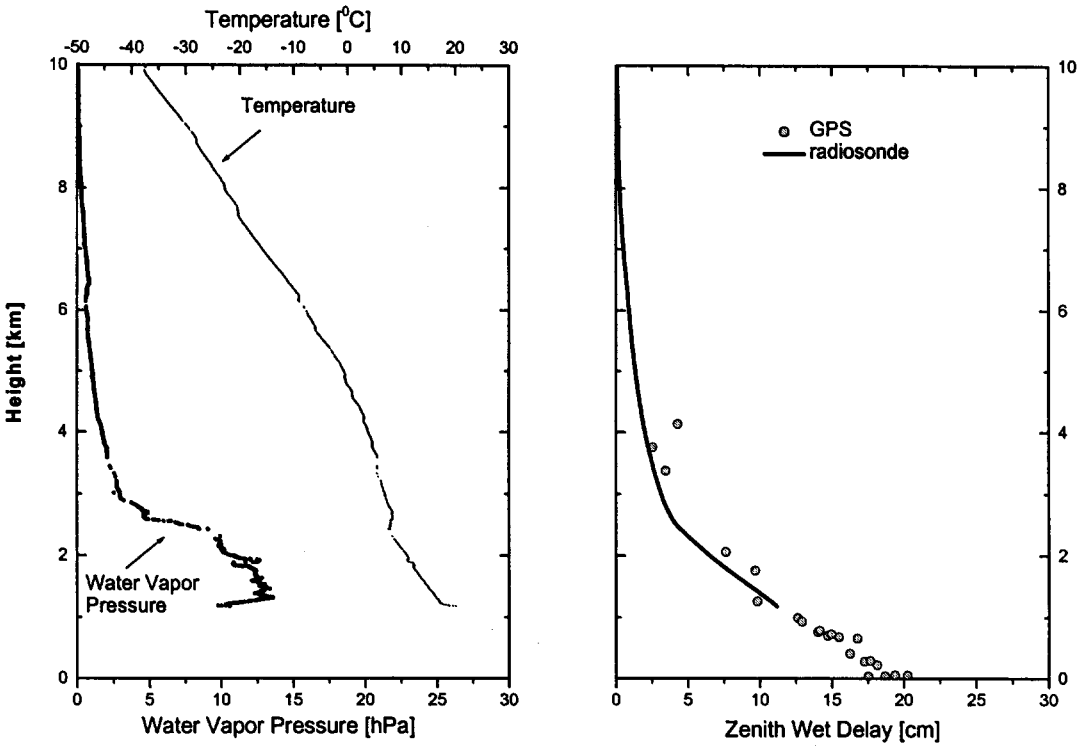

Station: VOLCANO, Sonde: 23:00 UT, Feb. 18

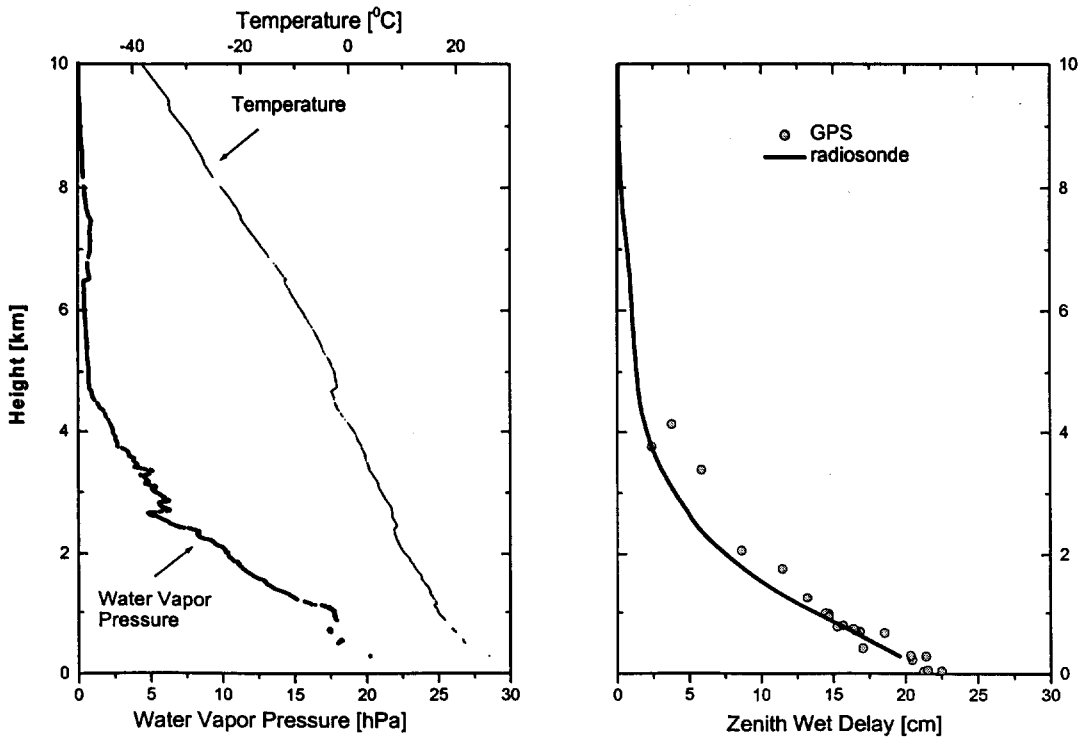

Station: BILL, Sonde: 23:00 UT, Feb. 19

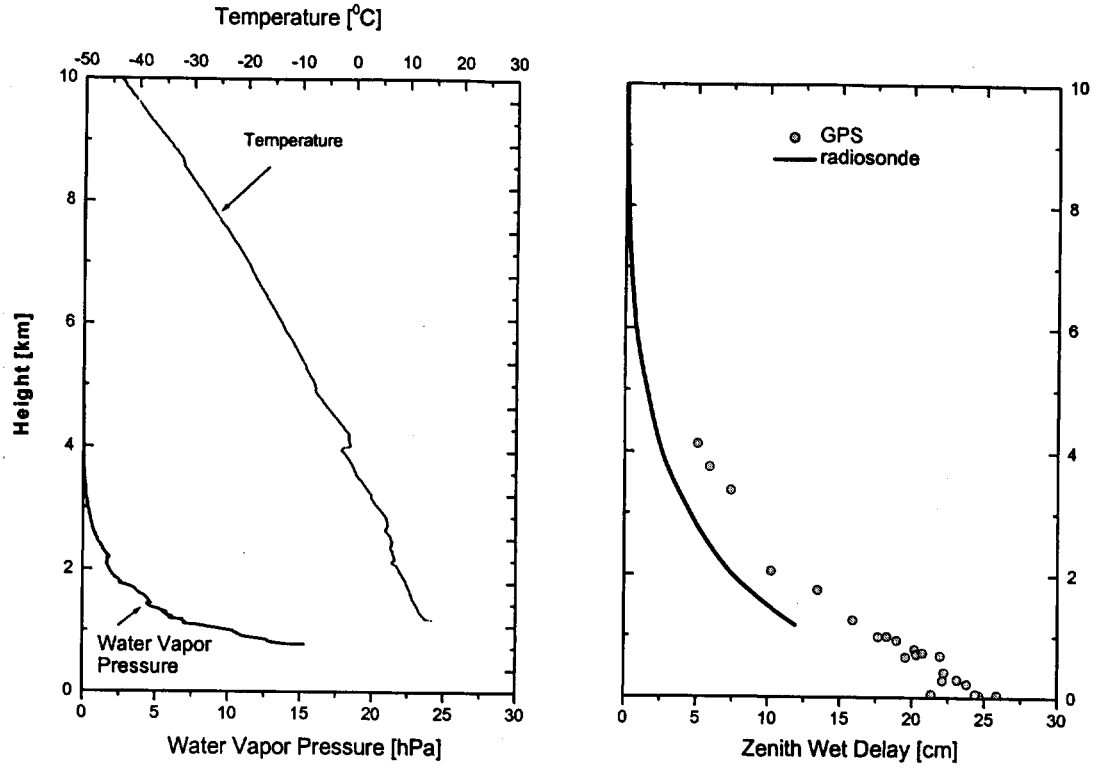

Station: VOLCANO, Sonde: 20:00 UT, Feb. 21

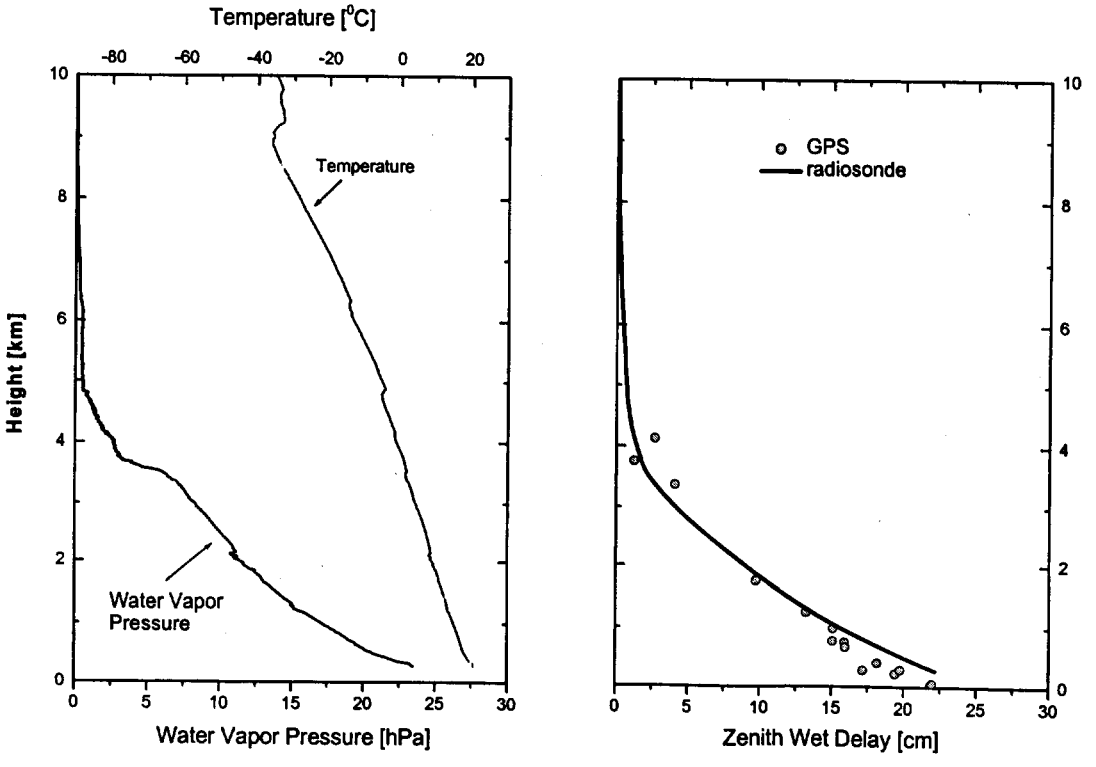

Station: BILL, Sonde: 15:00 UT, Feb. 22

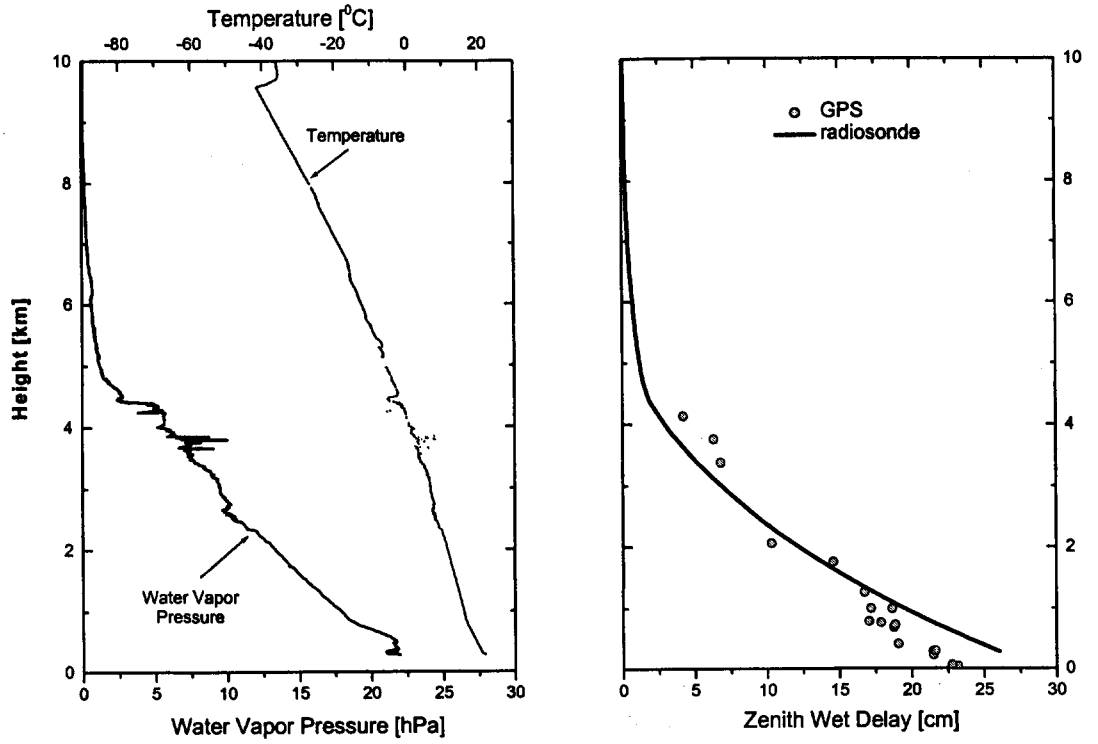

Station: BILL, Sonde 23:00 UT, Feb. 22

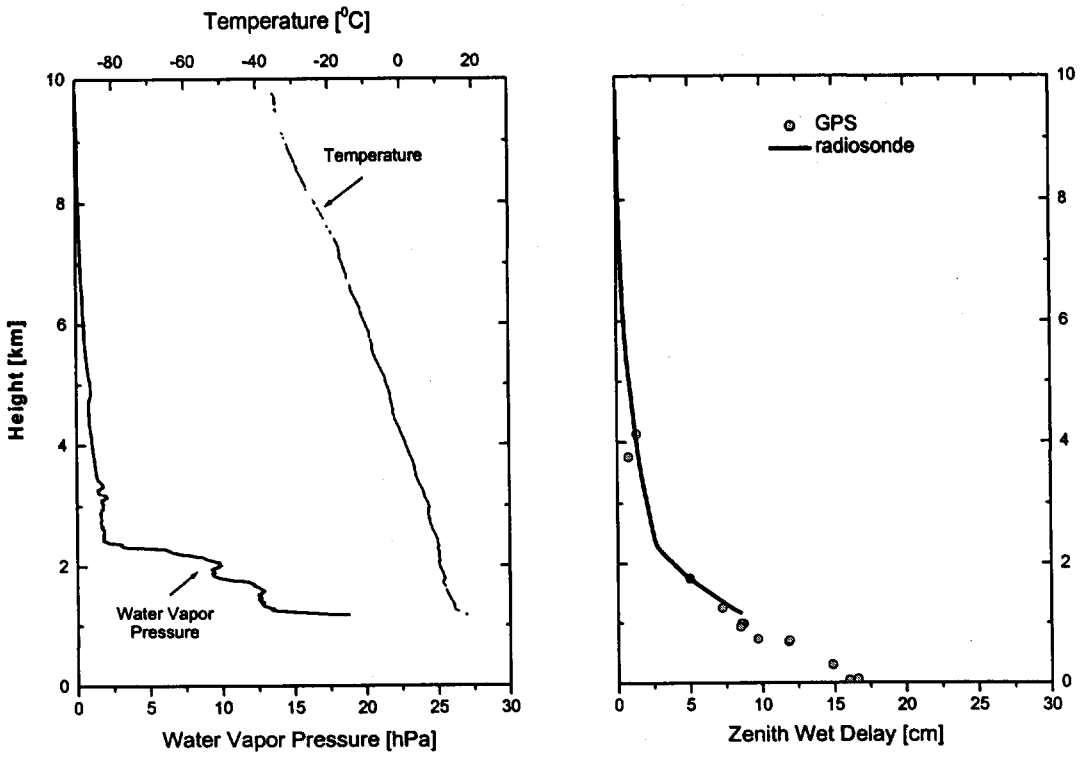

Station: VOLCANO, Sonde 01:00 UT, Feb. 23

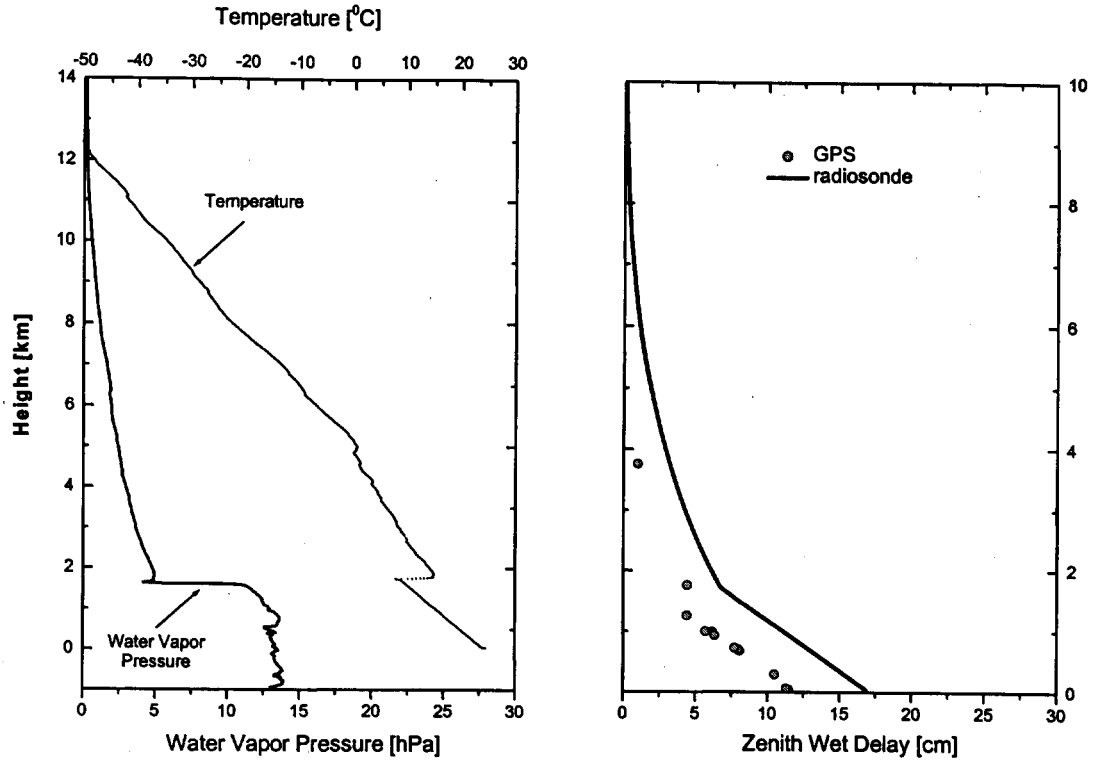

Station: PGF4, Sonde 23:00 UT, Feb. 24

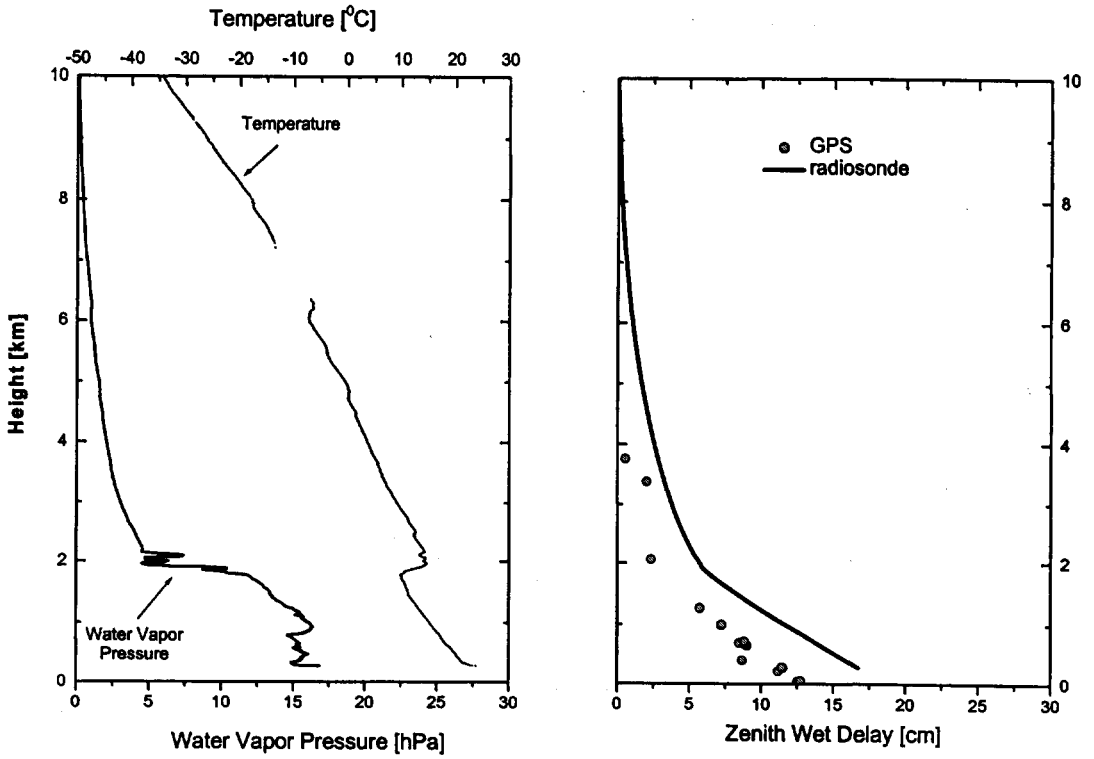

Station: BILL, Sonde 13:00 UT, Feb. 25

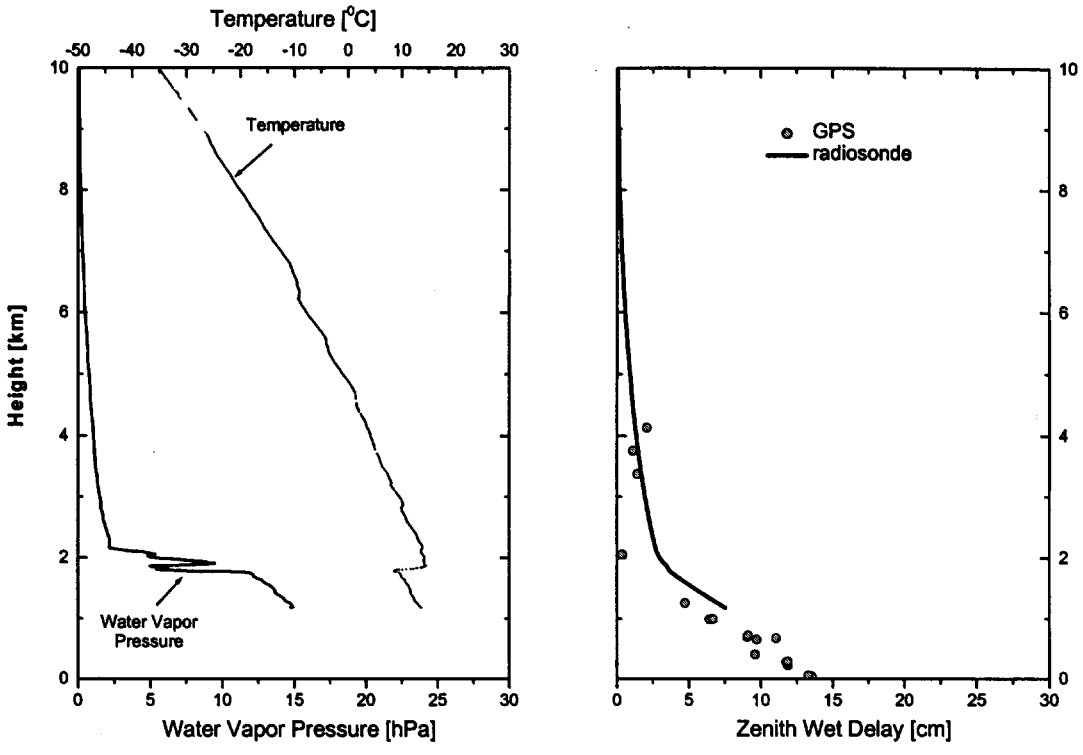

Station: VOLCANO, Sonde: 16:00 UT, Feb. 25

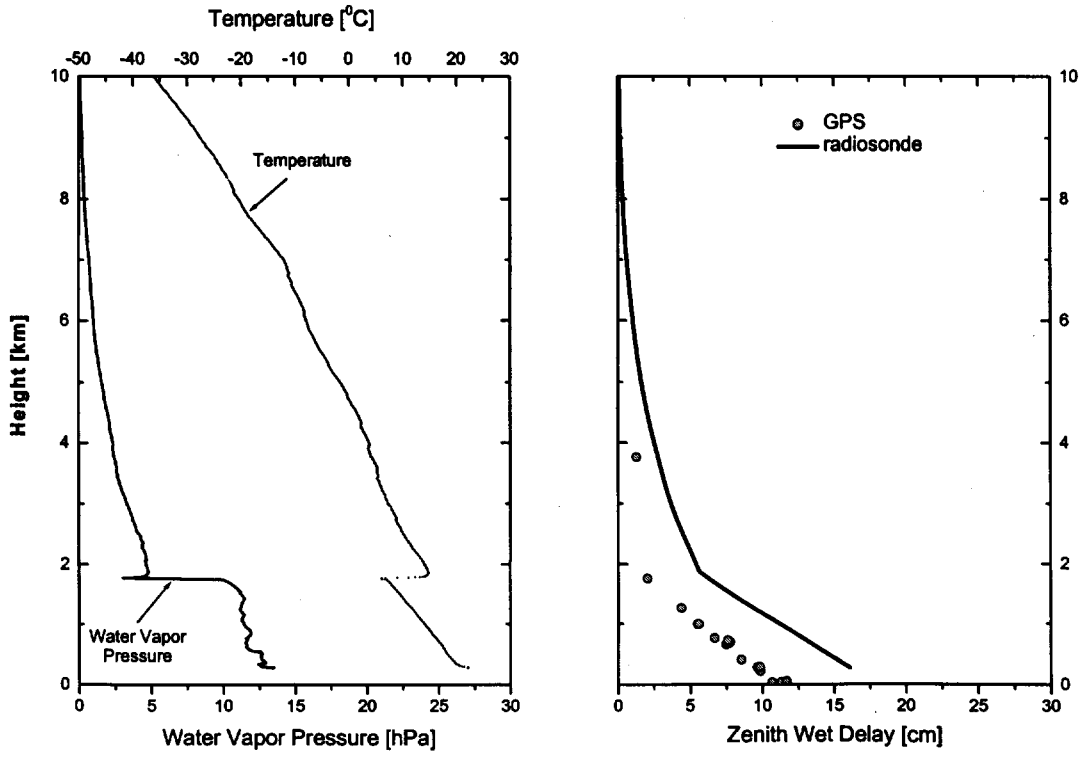

Station: BILL, Sonde: 22:00 UT, Feb. 25

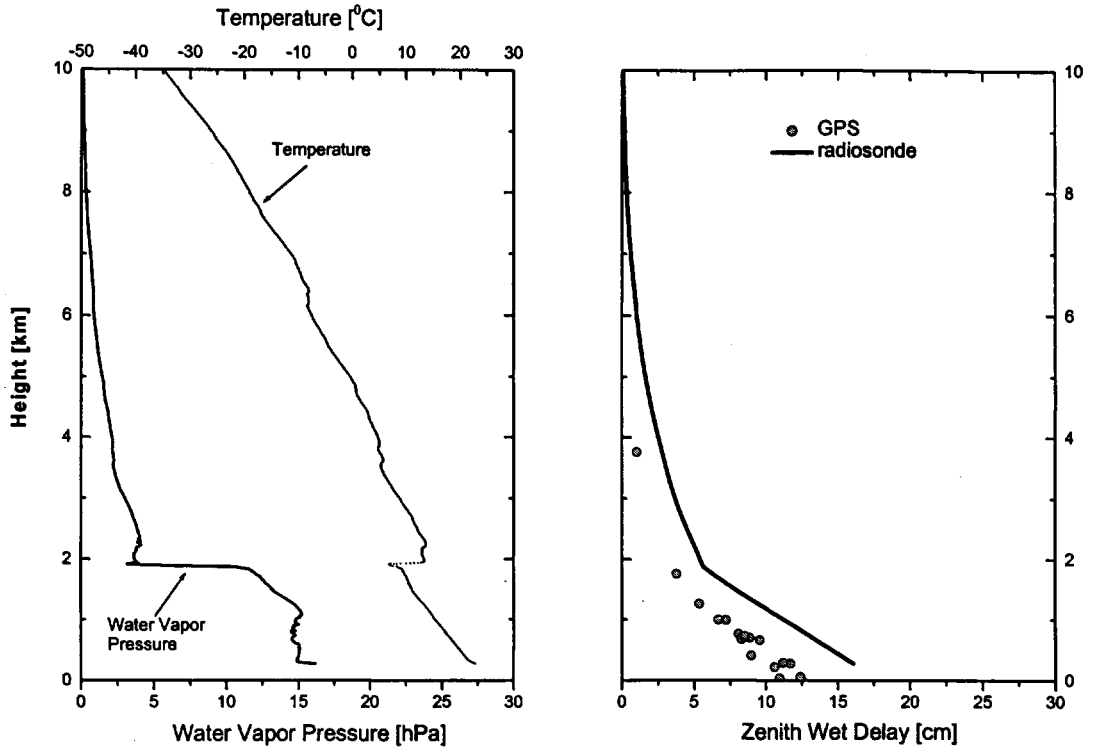

Station BILL, Sonde: 23:00 UT, Feb. 25

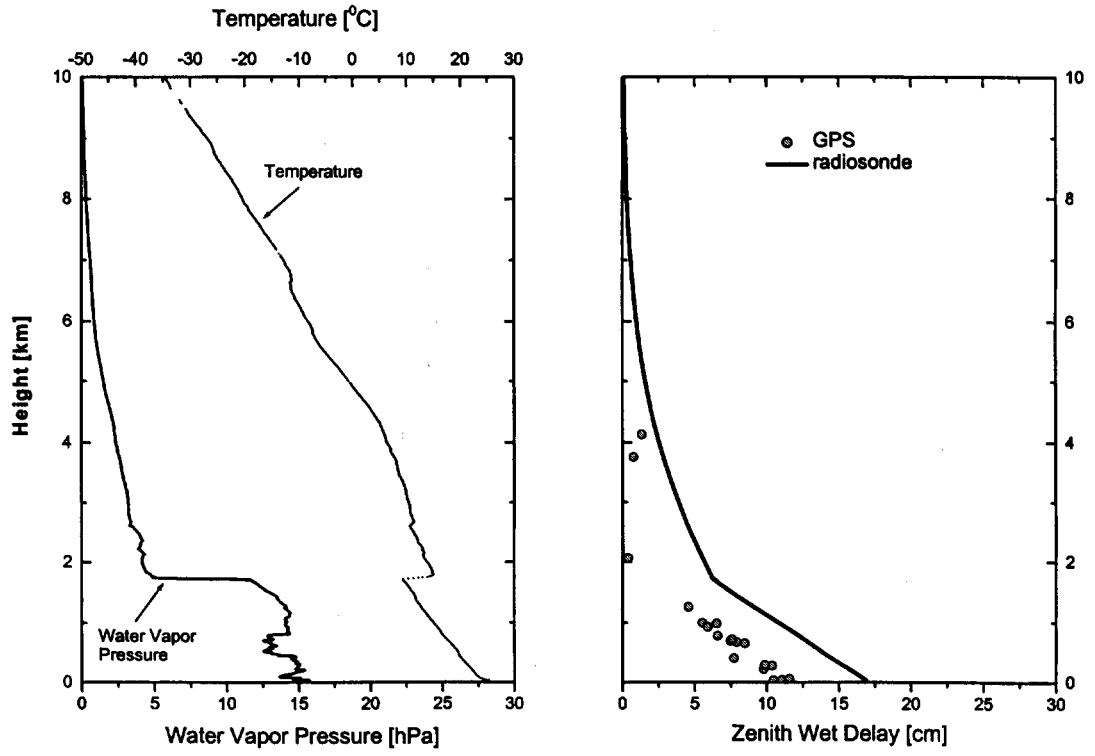

Station PGF4, Sonde: 13:00 UT, Feb. 26

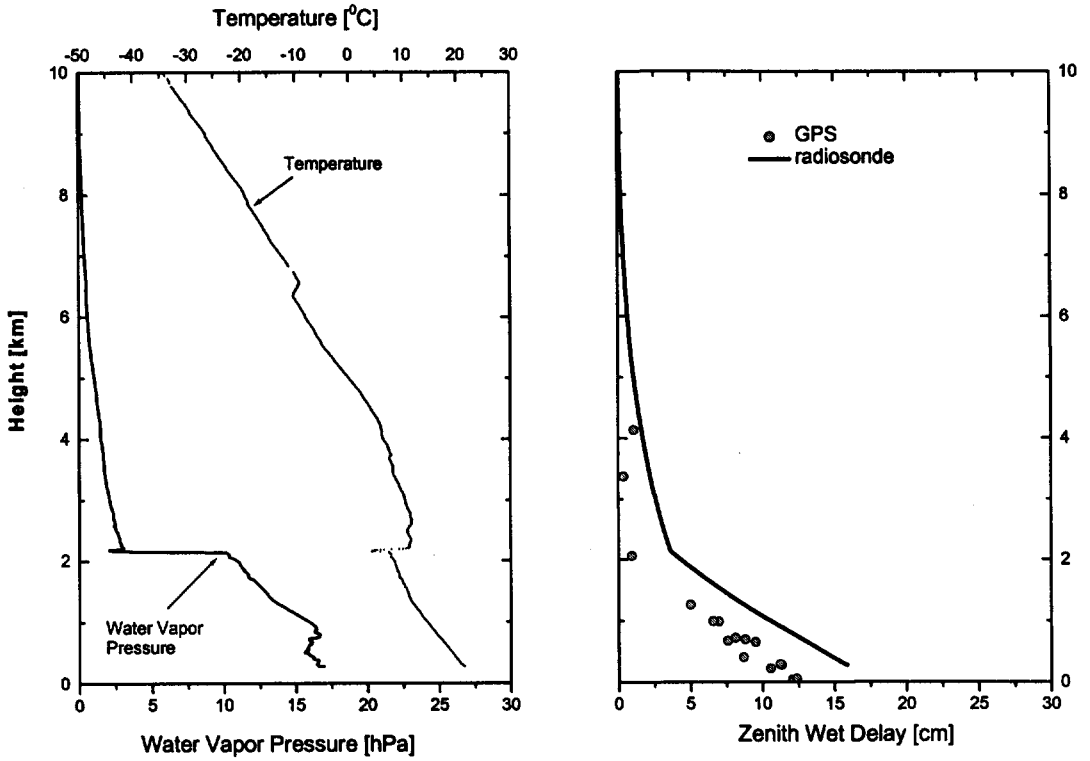

Station: BILL, Sonde 23:00 UT, Feb. 26

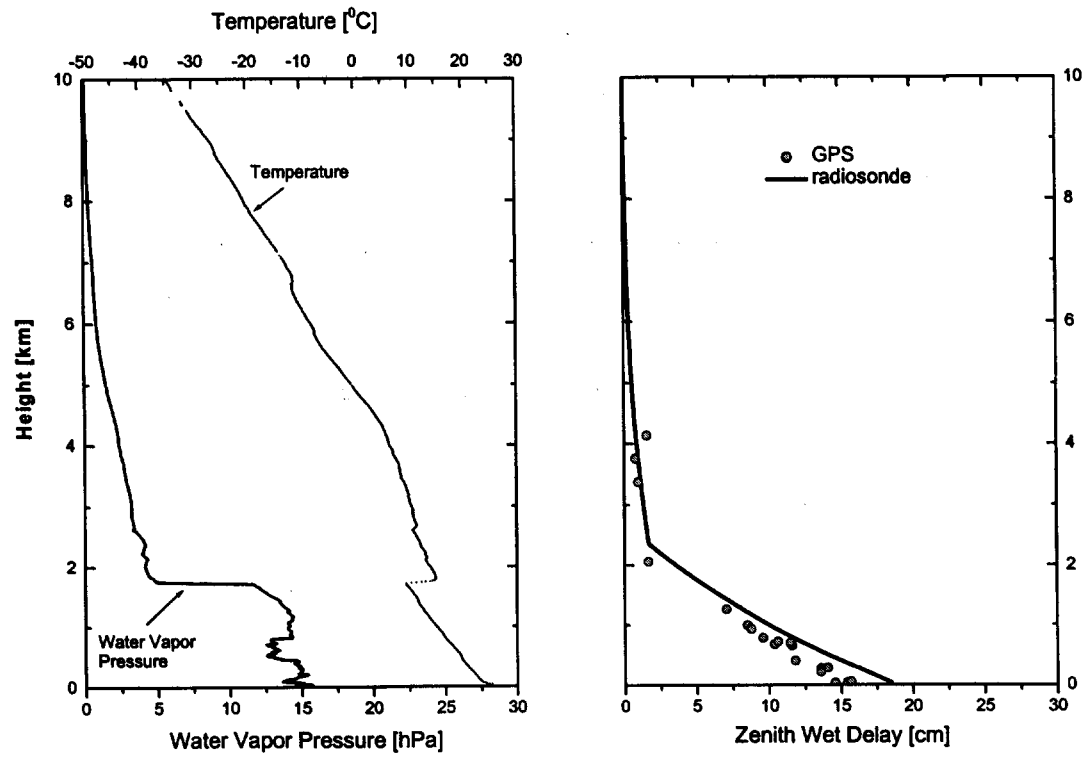

Station: PGF4, Sonde 21:00 UT, Feb. 27

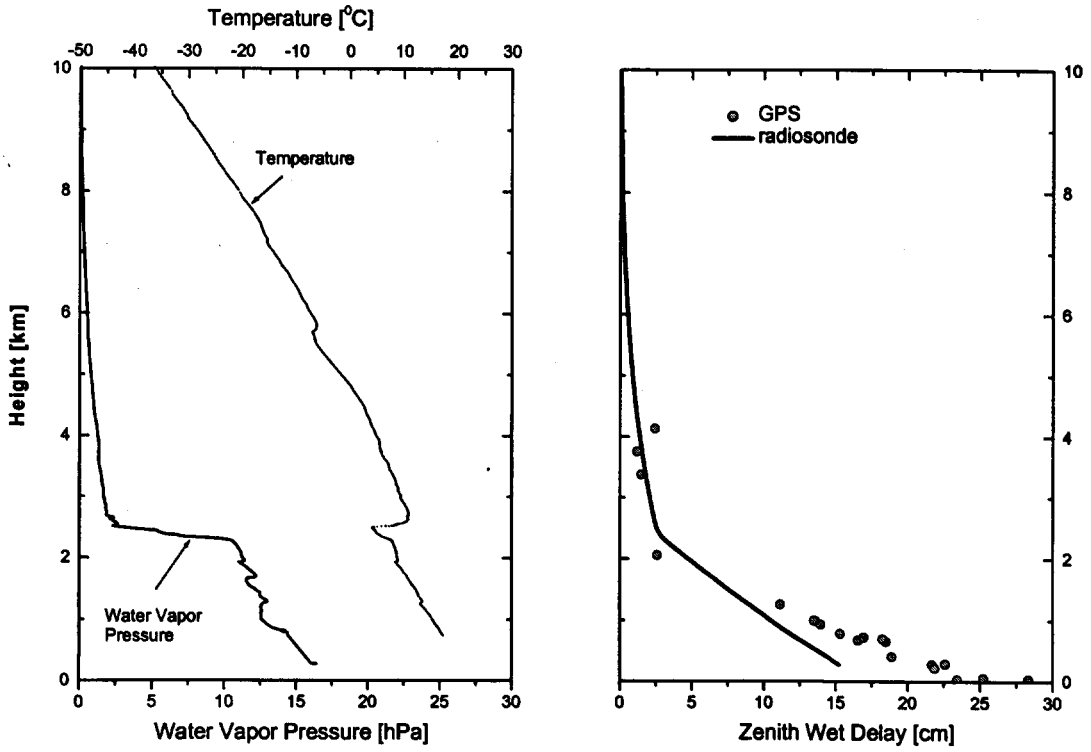

Station: BILL, Sonde: 22:00, Feb. 27

"Geodätisch-geophysikalische Arbeiten in der Schweiz"

(Fortsetzung der Publikationsreihe "Astronomisch-geodätische Arbeiten in der Schweiz") der Schweizerischen Geodätischen Kommission (ab Bd. 40):

40 1989 Integrale Schwerefeldbestimmung in der Ivrea- Zone und deren geophysikalische Interpretation. B. Bürki. 186 Seiten.

41 1990 ALGESTAR satellitengestützte Geoidbestimmung in der Schweiz. U. Marti. 61 Seiten plus Punktprotokolle.

42 1990 Höhensysteme, Schwerepotentiale und Niveauflächen: Systematische Untersuchungen zur zukünftigen terrestrischen und GPS-gestützten Höhenbestimmung in der Schweiz. B. Wirth. 204 Seiten.

43 1990 Gravimetrisches Geoid der Schweiz: Potentialtheoretische Untersuchungen zum Schwerefeld im Alpenraum. A. Geiger. 231 Seiten.

44 1991 Rapid Differential Positioning with the Global Positioning System (GPS). E. Frei. 178 Seiten.

45 1992 Dreidimensionales Testnetz Turtmann 1985-1990 Teil I. F. Jeanrichard (Hrsg.) Autoren: A.Geiger, H.-G. Kahle, R. Köchle, D. Meier, B. Neininger, D. Schneider, B. Wirth. 183 Seiten.

46 1993 Orbits of Satellite Systems in Space Geodesy. M. Rothacher. 243 Seiten.

47 1993 NFP 20. Beitrag der Geodäsie zur geologischen Tiefenstruktur und Alpendynamik. H.-G. Kahle (Hrsg.) Autoren: I. Bauersima, G. Beutler, B. Bürki, M. Cocard, A. Geiger, E. Gubler, W. Gurtner, H.-G. Kahle, U. Marti, B. Mattli, M. Rothacher, Th. Schildknecht, D. Schneider, A. Wiget, B. Wirth. 153 Seiten plus 90 Seiten Anhang.

48 1994 Ionosphere and Geodetic Satellite Systems: Permanent GPS Tracking Data for Modelling and Monitoring: Urs Wild, 155 Seiten.

49 1994 Optical Astrometry of Fast Moving Objects using CCD Detectors: Thomas Schildknecht, 200 Seiten.

50 1995 Geodätische Alpentraverse Gotthard: A. Elmiger, R. Köchle, A. Ryf und F. Chaperon. 214 Seiten.

51 1995 Dreidimensionales Testnetz Turtmann 1985-1993, Teil II (GPS-Netz). F. Jeanrichard (Hrsg.) Autoren: G. Beutler, A. Geiger, M. Rothacher, Stefan Schaer, D. Schneider, A. Wiget, 173 Seiten.

52 1995 High Precision GPS Processing in Kinematic Mode: M. Cocard. 139 Seiten.

53 1995 Ambiguity Resolution Techniques in Geodetic and Geodynamic Applications of the Global Positioning System. L. Mervart. 155 Seiten.

54 1997 SG 95: Das neue Schweregrundnetz der Schweiz: F. Arnet und E. Klingelé. 37 Seiten.

55 1997 Combination of Solutions for Geodetic and Geodynamic Applications of the Global Positioning System (GPS). Elmar Brockmann, 211 Seiten.

56 1997 Geoid der Schweiz 1997. Urs Marti, 140 Seiten.

57 1998 Astrometry and Satellite Orbits: Theoretical Considerations and Typical Applications. Urs Hugentobler, 209 Seiten.

58 1998 Systematic Investigations of Error- and System-Modelling of Satellite Based Flight Approaches and Landings in Switzerland. Maurizio Scaramuzza, 165 Seiten.

59 1999 Mapping and Predicting the Earth's Ionosphere Using the Global Positioning System. Stefan Schaer, 205 Seiten.

60 2000 Modeling and Validating Orbits and Clocks Using the Global Positioning System. Timon Anton Springer, 154 Seiten.

61 2001 Spatial and Temporal Distribution of Atmospheric Water Vapor using Space Geodetic Techniques. Lars Peter Kruse, 128 Seiten.